Crack Injection as a Mechanism for Stress Corrosion Cracking

by

Erin Karasz

A Dissertation Presented in Partial Fulfillment
of the Requirements for the Degree
Doctor of Philosophy

Approved November 2020 by the
Graduate Supervisory Committee:

Karl Sieradzki, Chair
Nikhilesh Chawla
Pedro Peralta
Jagannathan Rajagopalan

ARIZONA STATE UNIVERSITY

December 2020

ABSTRACT

Traditionally nanoporous gold is created by selective dissolution of silver or copper from a binary silver-gold or copper-gold alloy.  These alloys serve as prototypical model systems for a phenomenon referred to as stress-corrosion cracking.  Stress-corrosion cracking is the brittle failure of a normally ductile material occurring in a corrosive environment under a tensile stress.  Silver-gold can experience this type of brittle fracture for a range of compositions.  The corrosion process in this alloy results in a bicontinuous nanoscale morphology composed of gold-rich ligaments and voids often referred to as nanoporous gold.  Experiments have shown that monolithic nanoporous gold can sustain high speed cracks which can then be injected into parent-phase alloy.

This work compares nanoporous gold created from ordered and disordered copper-gold using digital image analysis and electron backscatter diffraction. Nanoporous gold from both disordered copper-gold and silver-gold, and ordered copper-gold show that grain orientation and shape remain largely unchanged by the dealloying process.  Comparing the morphology of the nanoporous gold from ordered and disordered copper-gold with digital image analysis, minimal differences are found between the two and it is concluded that they are not statistically significant.  This reveals the robust nature of nanoporous gold morphology against small variations in surface diffusion and parent-phase crystal structure.

Then the corrosion penetration down the grain boundary is compared to the depth of crack injections in polycrystal silver-gold.  Based on statistical comparison, the crack-injections penetrate into the parent-phase grain boundary beyond the corrosion-induced porosity.  To compare crack injections to stress-corrosion cracking, single crystal silver-

gold samples are employed. Due to the cleavage-like nature of the fracture surfaces, electron backscatter diffraction is possible and employed to compare the crystallography of stress-corrosion crack surfaces and crack-injection surfaces. From the crystallographic similarities of these fracture surfaces, it is concluded that stress-corrosion can occur via a series of crack-injection events. This relationship between crack injections and stress corrosion cracking is further examined using electrochemical data from polycrystal silver-gold samples during stress-corrosion cracking. The results support the idea that crack injection is a mechanism for stress-corrosion cracking.

ACKNOWLEDGMENTS

Many thanks to my advisor, Dr. Karl Sieradzki, for his mentorship and guidance through my graduate research at Arizona State University. His knowledge and expertise has been invaluable and he has helped me grow immensely as a researcher. I am very appreciative of all the coffee break discussions we have had over the years and the advice that made this research possible.

I would also like to thank my committee members, Dr. Nikhilesh Chawla, Dr. Pedro Peralta, and Dr. Jagannathan Rajagopalan for their time and consideration. I appreciate all the valuable insight and feedback. Thank you to Dr. Ashlee Aiello, Dr. Marion Branch-Kelly, Ariana Tse, and Yusi Xie for your help and support both in and out of the lab. Also thank you to Dr. Nilesh Badwe, Dr. Xiying Chen, and Dr. Ke Geng for your help and support in my research. Special thanks to my mentors, Dr. R. Allen Roach and Amy Kaczmarowski, for introducing me to the world of materials science and encouraging me to go to graduate school. Without your belief in me, I would not have pursued a doctorate.

To my parents and my grandparents, I could not have done this without you. Thank you for all your love and sacrifice. I'm so appreciative of how you made science and engineering an intentional part of my life from a young age. Thank you for all your support.

Finally to my husband, Zach, thank you for taking this journey with me. There is no one I would rather have by my side and I could not have done it without you.

TABLE OF CONTENTS

iv

LIST OF TABLES

LIST OF FIGURES

CHAPTER 1

INTRODUCTION AND BACKGROUND

Nanoporous gold (NPG) is a bicontinuous system of ligaments and pores.  The

high surface area to volume ratio of nanoporous gold combined with the catalytic

capabilities of gold make it a material of interest.  Areas of research include catalysis

(Zeis et al. 2008), biosensing (Zheng et al. 2019), and actuation (J. Weissmüller et al.

2003).  Such areas are concerned with surface area to volume ratio (ligament diameter)

and the morphology of the nanoporous gold (Chen-Wiegart et al. 2012).  The traditional

method of making nanoporous gold is the selective leeching, referred to as dealloying, of

silver from a binary alloy of silver-gold.  Other material systems that can form

nanoporosity by dealloying, such as copper-manganese and aluminum-nickel, can take on

ordered structures. Silver-gold is disordered over all compositions.

Differences in composition can lead to differences in morphology.  As such,

there has been no research on the effects of ordered versus disordered parent alloy on

dealloying morphology.  Copper-gold can be used as a parent material to make

nanoporous gold and, unlike silver-gold, it can be heat-treated to adopt both long-range

ordered and disordered crystal structures.  At a composition of 75 at% copper and 25 at%

gold the alloy is generally disordered, but through extensive heat-treatment the $L1_2$

ordered crystal structure is achieved and can be retained.  In the $L1_2$ ordered structure,

gold atoms occupy the corner positions of a cube and copper atoms occupy the face-

centered positions (H. Okamoto, Chakrabarti, and Laughin 1987).  The lattice parameter

of this ordered phase is 0.3743 nm compared to that of the disordered, face-centered

cubic (FCC) phase which is 0.3754 nm (H. Okamoto, Chakrabarti, and Laughin 1987).

Chapter 2 compares nanoporous gold morphology created by dealloying ordered and disordered copper-gold as well as the grain structure before and after dealloying. A more complete background of dealloying is presented in Section 1.1 and a background of nanoporous gold is presented in Section 1.2.

Nanoporous gold can sustain high-speed cracks (S. Sun et al. 2015) which can then be injected into the undealloyed parent phase material causing stress-corrosion failure (N. Badwe et al. 2018; Sieradzki and Newman 1985). The phenomena of normally ductile materials failing in a brittle manner when under tensile stress and in a corrosive environment is called stress-corrosion cracking.

Instances of stress-corrosion cracking have been studied since the 1950's and are generally catastrophic and unexpected. The real-world consequences of stress-corrosion cracking are often expensive and can even result in loss of life. An iron-alloy pipe in a pressurized water reactor at Surry Nuclear Plant underwent stress-corrosion cracking due to the pressure of steam it was carrying and the corrosive nature of iron-based alloys in the presence of water, resulting in the deaths of four workers in 1986 (Lochbaum 2018). In a less deadly but expensive case, California's bullet train project was delayed in 2019 when steel supports for a bridge began successively snapping, a stress-corrosion failure that resulted from the penetration of rain into the internal structure (Vartabedian 2020).

In addition to being expensive, stress-corrosion cracking can also have environmental impacts. In 2018 stress-corrosion cracking was responsible for the failure of a gas pipeline in Canada that interrupted the gas supply to several refineries and left a large crater and scorched pine trees behind (Nickel 2020). The proposed mechanisms of stress-corrosion cracking are described in Section 1.3.1.

Hydrogen embrittlement is a phenomenon that presents similarly to stress-corrosion cracking although it is not pertinent to nanoporous gold.  In alloys that can experience hydrogen embrittlement, the fracture surfaces resulting from stress-corrosion cracking are indistinguishable from those caused by hydrogen embrittlement.  Therefore the proposed mechanisms for hydrogen embrittlement are examined in Section 1.3.2.

The work presented in Chapter 3 of this thesis uses nanoporous gold from polycrystal silver-gold to examine crack injection events.  In Section 3.1 the corrosion and tensile stress components are separated in time, creating crack injections in grain - boundaries.  Section 3.2 examines the continuity of stress-corrosion cracking propagation.  Evidence is presented here in the form of current transients to support the theory that stress-corrosion cracking occurs by a series of finite crack injections.

Chapter 4 utilizes single crystal silver-gold samples to examine transgranular crack injections and compare the fracture surfaces to those obtained in transgranular stress-corrosion.

 Similar to observations by Li and Sieradzki, Badwe et al.  showed that for nanoporous gold samples of 125 µm thickness, ligament diameters less than 220 nm exhibited brittle behavior while larger ligaments exhibited ductile behavior (Nilesh Badwe, Chen, and Sieradzki 2017; R. Li and Sieradzki 1992).  Chapter 5 explores sample size/thickness effects on the fracture behavior of smaller nanoporous gold samples to see if the same transition exists and for what average ligament diameter in relation to the thickness of the sample.

1.1 Dealloying

Dealloying, sometimes called selective dissolution or leeching, is a type of

corrosion mechanism where a specific atomic species is removed from an alloy. Early

on, dealloying was used to "purify" gold ore. It was found that for dealloying to occur

there was a compositional criterion referred to as a 'parting limit' discussed in Section

1.1.2.

Later it was discovered that there are alloys that can be completely dealloyed,

leaving a material composed entirely of a bicontinuous ligament-void morphology (R. Li

and Sieradzki 1992). The ligaments can be highly enriched in the more noble metal, the

other being removed from the alloy. The traditional method of fabricating nanoporous

metals is electrochemical dealloying which can be classified as a type of corrosion.

However more recently methods such as liquid metal dealloying (McCue, Karma, and

Erlebacher 2018) have begun to be explored. Only electrochemically induced dealloying

is discussed here.

1.1.1 Porosity

One of the earliest alloys used to study dealloying was brass. By the 1920's

researchers were aware that brass underwent 'dezincification' where the surface of brass

would become enriched in copper but many believed that the copper was dissolved and

then redeposited. In 1934 Stillwell and Turnipseed determined that in strong acids both

zinc and copper were dissolved and the copper redeposited to form this enriched copper

layer, but in weaker acids only the zinc was removed (Stillwell and Turnipseed 1934).

This selective dissolution was consistent with Graf's results a few years earlier on

4

copper-gold binary alloys where copper was dissolved from gold (Stillwell and Turnipseed 1934). In 1967 Pickering and Wagner set out to prove that selective dissolution was possible and that the enrichment of the nobler metal was not simply a case of dissolution and redeposition (Pickering and Wagner 1967). They corroded a copper-gold binary alloy in a rotating disk electrode setup which constantly refreshed the electrolyte at the metal/electrolyte interface, moving dissolved atoms away from the interface to prevent redeposition. These samples still showed a surface enriched in gold. Additionally, the ring electrode was gold to attract any dissolved gold as it was being removed by the rotation. The current from the ring electrode was extremely small, also indicating that gold was not being dissolved.

In 1978 Scamans and Swann saw nanoporosity, which they referred to at the time as bulbous protrusions, on corroded 304 stainless steel where selective dissolution had occurred (Scamans and Swann 1978). Dating back to the 1920's researchers had claimed a porous layer could be achieved on copper-zinc alloys (Pickering and Wagner 1967). Pickering and Wagner suggested that porosity formation would be dictated by volume diffusion and dismissed the role of surface diffusion (Pickering and Wagner 1967). They argued that bulk diffusion via divacancies, driven by a composition gradient between the bulk and the surface subjected to selective dissolution, would be fast enough to create porosity. This would compensate for bulk diffusivities being too slow, as others argued. They dismissed surface diffusion as being too slow. Measurements for surface diffusion at that time were done in vacuum, which it is now known gives much lower values for surface diffusivity than are obtained in electrolyte (Erlebacher 2004).

In the 1970's Forty proposed a mechanism that relied on surface diffusion (A.J.Forty 1979). Less noble atoms would be removed from the surface and the remaining nobler atoms would congregate together via surface diffusion forming islands. Forty observed such islands of gold on a partially dealloyed silver-gold single-crystal with transmission electron microscopy. These islands had started to grow together forming a sort of interlocking channel, island morphology.

In the 1980's the scanning tunneling microscope (STM) was developed by Binnig and Rohrer (Binnig and Rohrer 1986). The STM exploited tunneling spectroscopy, which had seen a lot of advancement in the 1960's (Giaever 1960), to examine the topography of surfaces on an atomic scale. This advance in microscopy allowed for a much closer interrogation of surfaces during dealloying (Oppenheim et al. 1991) which, in turn, led to the measurement of surface diffusivities in electrolyte (Seebauer and Allen 1995). Surface diffusivities of materials like gold in electrolytes are much larger than bulk diffusion, lending credence to the surface diffusion model (Oppenheim et al. 1991; Moffat, Fan, and Bard 1991).

Erlebacher et al. (Erlebacher et al. 2001) proposed a mathematical description based on the flux of diffusing atoms following the Cahn-Hilliard (J. W. Cahn 1959) equation for diffusion during spinodal decomposition. They arrived at the equation

$$\frac{\partial C}{\partial t} = v_n C_0 - v_n \kappa C - \nabla \cdot J_s. \tag{1}$$

$J_s$ is the flux of diffusing atoms, and $C_0$ is the concentration of gold in the bulk. $v_n$ is the velocity of the interface normal to itself, which depends on $\kappa$, the local curvature, and C, the gold concentration. They estimate $J_s = -D_s \nabla C$. This equation was implemented in a kinetic Monte Carlo simulation and agreed with experimental silver-

gold results (Erlebacher et al. 2001). Later kinetic Monte Carlo simulations by

Erlebacher, also on silver-gold, account for site coordination of atoms. For the rate of

diffusion, $k_{diff}$, and the rate of dissolution, $k_{diss}$, Erlebacher (Erlebacher 2004) used

$$k_{diss} = v_E \exp\left[-\frac{aE_b - \phi}{k_B T}\right] \tag{2}$$

$$k_{diff} = v_D \exp\left[-\frac{aE_b}{k_B T}\right] \tag{3}$$

Here $E_b$ is the bond energy, the applied voltage is $\phi$, T is absolute temperature,

and $k_B$ is Boltzmann's constant. The $v_E$ term is a frequency held at $10^4$ s$^{-1}$ for their

simulations, correlating to a monolayer of less noble atoms dissolved per second and the

$v_D$ term is a frequency based on the surface diffusion of gold in electrolyte. These

simulations obtained results qualitatively consistent with experimental results for critical

potential values (Erlebacher 2004). Direct, quantitative comparisons cannot be made yet

due to some simplifications in the kinetic Monte Carlo simulations which are presently

required to keep computing costs manageable.


1.1.2 Parting Limit

While most material properties change continuously as a function of composition,

some experience a discontinuous change in their chemical reactivity at a specific

composition, termed the parting limit. When the less noble component is richer than that

of the parting limit, selective dissolution can occur and when it is less than the parting

limit it cannot. This selective dissolution process is sometimes termed 'dealloying'

referring to the removal of an atomic species from an alloy. The terms 'dealloying

threshold' and 'parting limit' are often used interchangeably in literature.

7

The name 'parting limit' has origins in gold-mining. Gold ore can be purified by being submerged in nitric acid, but only if the atomic percentage of gold is low enough. In the event that the percentage of gold was not low enough to part the impurities from the gold, the gold ore would be melted and combined with silver and subjected to nitric acid again (R. W. Cahn 1997). Once the percentage of silver was high enough, the silver and the impurities would be parted from the gold, hence the name 'parting limit'. The percentage of silver required to 'part' the impurities from the gold was experimentally found to be approximately 65 at% silver (Sieradzki et al. 2002, 1989). Parting limits exist for other alloy systems as well, though the value of the parting limit varies by alloy. For example, the parting limit in copper-gold is ~60 at% copper.

The German researcher Tammann researched parting limits in the 1920's and found some alloys exhibit sharp parting limits (Movrin 2000). Sharp, in this case, refers to a sudden, non-negligible increase in chemical reactivity. This research lead Tammann to determine that a sharp parting limit will only occur in homogenized solid solutions where the atoms cannot change place in the solid phase. His explanation relied on the statistical distribution of atoms in an ordered crystal lattice to form continuous paths of atom species. The paths of less noble species would then allow electrolyte to penetrate the bulk as atoms were removed and allow atoms below the surface to be exposed to electrolyte. Later Masing and Borelius independently predicted, and Dehlinger and Giesen experimentally confirmed, that although Tammann's explanation relied on an ordered material, sharp parting limits could be found in disordered materials if Tammann's other criteria were met (Movrin 2000). Dehlinger and Glockner later pointed

8

out that although Tammann's criteria for a sharp parting limit appeared correct, the explanation was insufficient to account for the dealloying process (Movrin 2000).

One school of thought is that this limit is related to percolation theory and is analogous to the percolation threshold in percolation theory (Sieradzki and Newman 1986). Percolation threshold refers to the point in the composition where continuous "paths" of the constituent in question are formed, connecting one end of a huge sample to the other. These "paths" are sometimes referred to as an "infinite cluster" (Sieradzki and Newman 1986). In some cases, the parting limit is very close to the percolation threshold. For example, copper-aluminum has a percolation threshold of 20 at% aluminum and a parting limit of 13 at% aluminum. However, traditional percolation theory gives a percolation threshold value for silver-gold of 20 at% silver, substantially different from the parting limit of ~60 at% silver (Sieradzki et al. 1987). This value is reached by considering the case where the minimum number of silver atoms required to be near-neighbors with another silver atom to reach percolation is two (Sieradzki et al. 1989; Artymowicz, Erlebacher, and Newman 2009).

The discrepancy between the calculated percolation threshold and the parting limit is sometimes attributed to the fact that surface diffusion and dissolution contribute the parting limit. Although the exact influence of these factors has not been determined, if this were the primary source of the discrepancy then temperature would play a large role in the parting limit, which is not experimentally supported (Arne Wittstock et al. 2012). In response to this discrepancy, Sieradzki et al. applied a concept referred to as 'high density percolation' thresholds (Sieradzki et al. 1987). For high density percolation, the minimum number of silver atoms required to be near-neighbors with another silver atom

is increased to nine silver atoms. This gives a percolation threshold of ~60 at%, noticeably close to the experimentally determined parting limit of 65 at% silver (Artymowicz, Erlebacher, and Newman 2009).

1.1.3 Critical Potential

For electrochemically induced dealloying to create porosity the parting limit must be satisfied. Additionally the applied voltage must lie above a certain value, called the 'critical potential'. The critical potential is only defined for noble metal compositions below the parting limit. Above the critical potential, selective dissolution occurs at a rate which allows it to over take surface diffusion of the more noble element as the defining kinetic factor. Below this potential the alloy displays passivation-like behavior. The critical potential is above the standard electrode potential of the less noble element in order to remove it from the alloy, but below the standard electrode potential of the more noble element so that it is not also simultaneously removed. Pickering noted that the difference in the standard electrode potentials of the alloy elements, $\Delta E^0$, must be sufficiently large to achieve a polarization curve with clear regions of passivity and dissolution (Pickering 1983). Specifically $\Delta E^0 \gg RT/F$ where R is the ideal gas constant, T is the temperature, and F is the Faraday constant.

The critical potential changes with composition. An alloy richer in the less noble species has a lower critical potential. If the alloy is too rich in the less noble species, it does not exhibit the distinct passivation-like and dissolution regions during linear sweep voltammetry, like curve 4 in Figure 1.1 from Pickering (Pickering 1983).

In this figure, species A is the less noble in a binary alloy of species A and B. The flat sections of curves 1, 2, and 3, labeled 'a', correspond to low current densities caused by an enriched layer of B protecting the sample. The inclined portions of curves 1 and 2, labeled 'b', correspond to the selective dissolution of species A and formation of porosity. An alloy containing too much of the more noble species, B, will push the critical potential up to the point where both species A and species B are removed, corresponding to curves 3a and 3b.
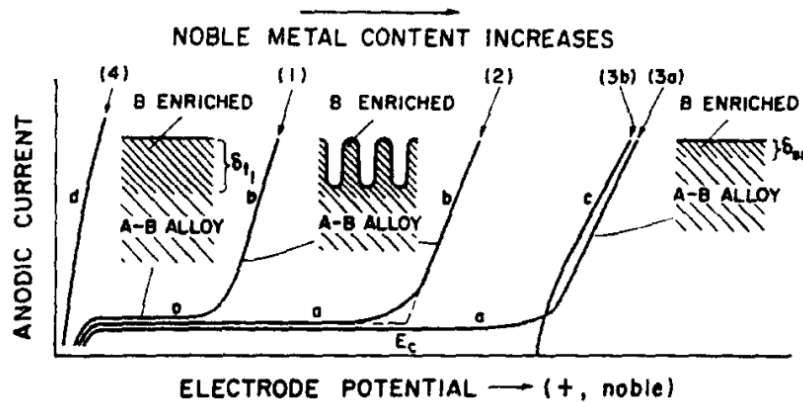


Figure 1.1: Anodic Polarization Curves for a Binary Alloy of a Binary A-B Alloy Where B Is the More Noble Species. Curve 4 Shows Passivation Like Behavior. Curves 1 and 2 Show the Region and Behavior for Selective Dissolution of A. Curve 3 Illustrates the Behavior for the Dissolution of Both A and B. (Pickering 1983)

An exact value for the critical potential cannot be determined from linear sweep voltammetry, but it can be approximated (Sieradzki et al. 2002). In order to create porosity, less noble atoms must be removed from terrace sites but the easiest atoms to remove, and therefore the first atoms to contribute to the current, are the edge sites. The critical potential is generally taken as the voltage in the 'knee' bend in the linear sweep voltammetry, where the current is 1 mA/cm$^2$ in the linear sweep voltammetry. This bend is labeled "E$_c$" in Figure 1.1. When the linear sweep voltammetry is being performed,

11

however, it must be done at an appropriate sweep rate. If the sweep rate is too fast it can artificially alter the measured critical potential as explained by Erlebacher (Erlebacher 2004) and Corcoran (Dursun, Pugh, and Corcoran 2003). Therefore it is imperative to use a sweep rate that will allow for steady-state dissolution to be reached at each potential step (Sieradzki et al. 2002).

A more precise method of measuring the critical potential is through a series of selective dissolution experiments employing the application of a constant voltage (chronoamperometry) (Dursun, Pugh, and Corcoran 2003, 2005). When the applied voltage is at or above the critical potential, the current density over a long time period is more constant. The further the applied voltage is below the critical potential, the more rapidly the decay occurs. The steady-state current density, or final current density when no steady-state is reached, plotted against the applied potential provides a much sharper transition.
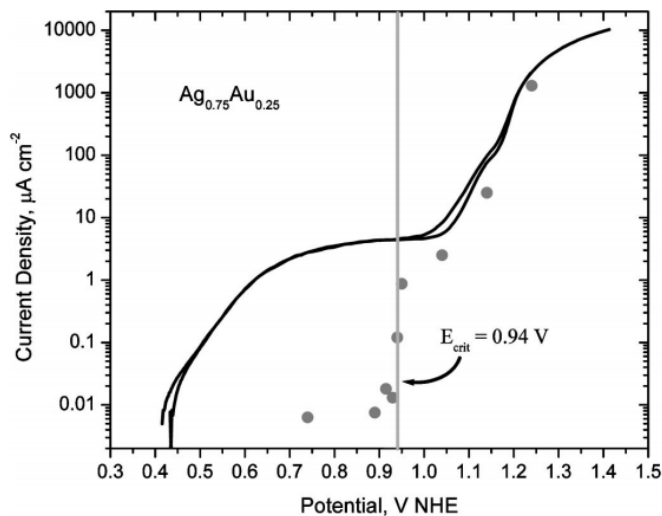


Figure 1.2: Linear Sweep Voltammetry (Line) and Steady-state or Final Current Density From Chronoamperometry (Dots) Versus Applied Potential for 75 at% Ag 25 at% Au In .1 M HClO$_4$ (Dursun, Pugh, and Corcoran 2005)

12

1.1.4 Coarsening

The ligaments in nanoporous metals can take on a range of diameters. The smallest recorded ligament size from dealloying is 2 nm (Snyder et al. 2010) and the largest is in the tens of microns (Kertis et al. 2010). Ligament size to some degree is tunable. Among the options for tuning ligament size are dissolution rates, heat treatments, and composition. Varying the dissolution rate and the composition of the parent phase material varies the ligament size that results from the dealloying process. Conversely, heat treatments are done on samples that have already been dealloyed and can only increase the ligament size from its as-dealloyed state.

At slower dissolution rates, the ligaments are larger and increasing the dissolution rate leads to smaller ligaments. Nanoporous gold has a substantial body of work making it the easiest to compare for this scenario. Li and Sieradzki have reported nanoporous gold ligaments as small as 15 nm (R. Li and Sieradzki 1992). Badwe et al. obtained an as-dealloyed nanoporous gold ligament diameter of 40 nm (Nilesh Badwe, Chen, and Sieradzki 2017). Detsi et al. found that relationship between ligament size and dealloying potential is linear for nanoporous gold for potentials from 1 to 1.5 V vs NHE (Detsi et al. 2011).

Ligaments can be coarsened after they have formed through heat treatments. The temperature and length of heat treatment has to be determined experimentally. In 1992 Li and Sieradzki introduced nanoporous gold as a material and tested multiple heat treatments on nanoporous gold (R. Li and Sieradzki 1992). They kept the length of the heat treatment constant at 10 minutes and varied the temperature. The initial ligament

diameter was ~3 nm and for a heat treatment at 100° C the ligament diameter became 10 nm, at 500° C 200 nm, 600° C 500 nm, 700° C 600 nm, and 800° C 1 μm.  This also provided the first evidence that nanoporous gold coarsens in a self-similar manner. Additionally, research has been done on nanoporous gold showing that the distribution of ligament diameters follows a Weibull distribution(Nilesh Badwe, Chen, and Sieradzki 2017).   Chen and Sieradzki examined the relationship between time, temperature, and ultimate ligament size (Q. Chen and Sieradzki 2013).  McCue et al. expanded upon these experimental results and made the assumption that surface self-diffusivity is the dominant mechanism for coarsening and followed Herring's analysis (Herring 1950) to arrive at the expression (McCue et al. 2018)

$$\lambda = At^n e^{-nE_a/k_bT}. \tag{4}$$

Here $\lambda$ is the average ligament diameter, t is time, $k_b$ is Boltzmann's constant, T is the temperature, and $E_a$ is the activation energy for the rate-limiting process.  A is a constant, representing all of the time and temperature independent constants.  For nanoporous gold ligaments coarsened in air at a single temperature they calculated  an $E_a$ of 1.33 $\pm$0.56 eV, an n of 0.12$\pm$ 0.05, and an A of 3800 $\pm$750 cm*sec$^{-n}$ (McCue et al. 2018).

There is some evidence that the specific type of environment the heat treatment takes place in may affect the results (Y. Sun, Burger, and Balk 2014; Kuwano-Nakatani et al. 2015).  Kuwano-Nakatani et al. observed that thermal coarsening occurs readily in nitrogen and oxygen gas but does not readily occur under vacuum (Kuwano-Nakatani et al. 2015).  Sun et al. also found that heat-treating in nitrogen gas causes more coarsening that heat-treating in vacuum (Y. Sun, Burger, and Balk 2014). They attribute this to

adsorbates from the gas assisting diffusion. This is surprising and, as Sun et al. mention, not intuitive. More work needs to be done in this area to rule out other factors. It is worth noting that the nanoporous gold heat treated in nitrogen shows large amounts of faceting, while nanoporous gold heat treated in ambient air and vacuum have smooth ligaments like those seen in the 'as-dealloyed' condition (Y. Sun, Burger, and Balk 2014).

There are techniques that do not involve heat-treating that allow the diffusion to be increased and cause coarsening. Ding et al. noted that submerging nanoporous gold in concentrated nitric acid increases the surface diffusion of gold and causes coarsening (Ding, Kim, and Erlebacher 2004). Hakamada treated nanoporous gold by submerging it in a HCl solution for 24 hours. They found that the ligaments coarsened and the (111) crystallographic texture was enhanced but less than a heat treatment of 873 K for 180 s (Hakamada and Mabuchi 2006, 2008). Coarsening has also been observed in nanoporous gold acting as a catalyst for CO oxidation (D. Li et al. 2013; Fujita et al. 2014; Pia, Cincotti, and Delogu 2016). Fujita et al. observed this using TEM, concluding that planar defects hindered coarsening (Fujita et al. 2014).

Coarsening can also create unintended consequences. Using kinetic Monte Carlo simulations Li et al. found that coarsening is affected by the solid fraction of the material (Y. Li et al. 2019). Specifically that for nanoporous gold with a solid fraction less than 30%, coarsening causes a loss in connectivity.

1.2 Nanoporous Gold

The ligaments that compose nanoporous gold (NPG) have a surface that is almost entirely gold and an interior that is enriched in gold, if not almost entirely gold. Ligament diameters can be controlled to a certain degree and can range from 5 nm to 1000 nm with a similar range for pore sizes. The density of NPG can vary, but generally falls between 30% and 50% (Nilesh Badwe, Chen, and Sieradzki 2017). Gold has properties advantageous for applications such as sensing (Arne Wittstock, Biener, and Bäumer 2010; Yin et al. 2014), catalysis (A. Wittstock et al. 2010; Zeis et al. 2008; Fujita et al. 2012; Jurgens et al. 2007), and bio applications (Xiao et al. 2014; Gittard et al. 2010) which are enhanced by the large surface area and tunable ligament size. Due to the low solubility of hydrogen in gold and its mechanical properties it can also be used as a model system for stress-corrosion cracking (N. Badwe et al. 2018).

Nanoporous gold is most commonly synthesized from multicomponent alloys through selective dissolution, often termed dealloying, induced by either the application of voltage or free corrosion. The resulting morphology of ligaments and voids can be "crack-free". The most common form of "cracks" are opened grain boundaries although they can also occur intergranularly where ligaments have simply not connected. The primary factor that influences whether NPG is crack-free or not is the dealloying rate. "Crack-free" procedures generally centralize around the idea of dealloying slowly (Senior and Newman 2006; Y. Sun et al. 2008; Jin et al. 2009).

Although it is possible to make NPG from an alloy consisting of more than two components, silver-gold and copper-gold alloys are the most common parent alloys. Silver-gold and copper-gold binary alloys are preferred, particularly when studying

16

stress-corrosion cracking due to its crystal structure, hydrogen solubility, and volume change during dealloying.

Gold is FCC and therefore does not have a ductile to brittle transition temperature like many body-centered cubic metals. Additionally, it has low or no solubility in acids where it can't be complexed which aids in the retention of gold during selective dissolution of a less noble species. Gold is a very noble metal allowing not only for catalysis but also providing a wide array of less noble elements that it can be alloyed with to form the parent alloy.

Both copper and silver are FCC and generally form FCC solid solutions with gold (or always in the case of silver), eliminating a phase change between parent alloy and NPG. The solubility of hydrogen in copper-gold and silver-gold alloys is extremely low allowing hydrogen embrittlement to be eliminated as a factor in stress-corrosion experiments. This allows stress-corrosion experiments to be performed on these alloys in water based electrolytes. Copper and silver also both have substantially lower standard electrode potentials than gold, making them easier to remove than other elements with higher standard electrode potentials. Silver is particularly close to gold in lattice parameter size, however copper is fairly different. Silver and gold have a lattice misfit of 0.2% while copper and gold have a lattice misfit of 11.4%. Therefore, using silver-gold allows the change in lattice parameter during dealloying to be minimized. Silver also provides the advantage of heat treating in ambient air, which would oxidize copper.

1.2.1 Mechanical Properties

Nanoporous gold is linearly elastic to fracture, indicating it behaves as a brittle material (Nilesh Badwe, Chen, and Sieradzki 2017). This is contrary to the nature of bulk gold which fractures in a ductile manner. However, upon close inspection of the ligaments themselves, they fracture in a ductile manner. In 2005 Biener et al. found that for samples with smaller ligaments (100 nm diameter), the ligaments experienced plastic flow and necking. Samples with ligaments of ~1 µm showed ligament failure via slip (Biener, Hodge, and Hamza 2005).

Li and Sieradzki reported in 1992 that bulk nanoporous gold also has the ability to macroscopically fracture in a ductile manner (R. Li and Sieradzki 1992). They found that the "natural length scale" of the sample, defined at sample thickness times the square root of the number of pores per unit area, determined the fracture strain of a sample. Fracture strains were large, indicating ductile fracture, for small natural length scales and conversely small, indicating more brittle fracture, for large natural length scales.

In addition to influencing the macroscopic behavior during failure, the size of the ligaments also influences some of the mechanical properties. The general trend is that the yield stress decreases as ligament diameter increases, although the technique or method results in a wide spread of values, as much an order of magnitude (Balk et al. 2009; Lührs et al. 2017).

The Gibson-Ashby relation for foams, seen in Equation 5, (Maiti, Ashby, and Gibson 1984) is a common method used to predict the Young's modulus of nanoporous gold, although it was developed for length scales of micrometers instead of nanometers. In the equation, E and $E_s$ are the Young's modulus of the porous material and bulk solid,

and $\rho/\rho_s$ is the relative density of the porous material.  The Young's modulus of

nanoporous gold does not scale with ligament size as shown by Weissmuller et al. (Jörg

Weissmüller et al. 2009).  Ligaments are not constrained by neighboring grains and

instead ligament strength behaves the way an independent nanowire would (Biener,

Hodge, and Hamza 2005; Biener et al. 2006; Hodge et al. 2007; Wang and Weissmüller

2013).

$$E = E_s \left(\frac{\rho}{\rho_s}\right)^2 \tag{5}$$

Experimentally the Young's modulus of nanoporous gold has been found to

depend on things other than the density.  Mameka et al. found that the storage modulus

increases as hydroxide adsorption increases and also changes linearly with the charging

and discharging of the double layer (Mameka et al. 2014).  They attribute these changes

in storage modulus to the surface stress of the ligaments.

The technique used to measure the mechanical properties also affects the Young's

modulus and yield strength values measured.  For nanoporous gold there exists an

asymmetry in tension-compression (Balk et al. 2009; Lührs et al. 2017).  In tension,

nanoporous gold generally fractures in a brittle manner, although it can behave in a

ductile manner at larger ligament sizes (Nilesh Badwe, Chen, and Sieradzki 2017).

Conversely, in compression nanoporous gold appears to fracture plastically and exhibit

quite a bit of strength.  Biener et al. used nanoindentation and measured a yield strength

of ~145 MPa and a Young's modulus of 11.1 GPa for samples with a ligament diameter

of ~100 nm (Biener, Hodge, and Hamza 2005).  For a ligament size of ~105 nm in

tension, Briot et al.  measured a yield strength of ~7.9 MPa and a Young's modulus of

6.25 GPa, markedly different (Briot et al. 2014).  Ahn and Balogun tested nanoporous

gold samples with ligament diameters around 30 nm but varying densities (Ahn and Balogun 2014). Using a non-destructive laser ultrasonics technique, they found that the Young's modulus varied with density and obtained values of 2.57 to 2.88 GPa for relative densities from 25% to 35%. This would suggest that the values obtained in tension are a more accurate depiction of the material than those obtained from compression. One suggested explanation for this apparent increase in strength in compression is the densification of the material as it is compressed like the densification seen by Volkert et al. in micropillar compression tests (Volkert et al. 2006) and Jin and Weissmuller for much larger samples (Jin and Weissmüller 2011). Another explanation that has been proposed is the surface energy. Luhrs et al. found that the plastic Poisson's ratio changes depending on the applied voltage (Lührs et al. 2017). Ultimately, they concluded that the asymmetry is due to the change in surface energy as the surface area is decreased in compression and increased in tension. Surface area can also be increased by decreasing the ligament diameter and some results have been recorded that indicate that as the ligament diameter decreases, the strength increases (Volkert and Lilleodden 2006; Greer and Nix 2006).

1.2.2 Dynamic Fracture

Freund defined dynamic fracture as a "…branch of the engineering science of fracture mechanics concerned with fracture phenomena on a time scale for which inertial resistance of the material to motion is significant" (Freund 1986). Griffith's theory of fracture says that energy has to be supplied to create new free surfaces and applies the theorem of minimum energy (Griffith 1921). This energy balance becomes the basis for

many equations of crack motion.  One of the more commonly referenced equations for crack motion was developed by Freund who used continuum mechanics and balanced the elastic energy release rate with the fracture energy.

Atkinson and Eshelby  proposed that the integral expression of dynamic energy release rate for dynamic growth was the quasi-static form where the total internal energy density replaced the elastic energy density (Atkinson and Eshelby 1968).  Freund adapted this dynamic energy release rate to a form dependent on crack tip stress and the deformation fields using elastodynamics (Freund 1972).  Goldman et al. expands on work from Freund to find the following equation for an "infinite medium" (Freund 1986; Goldman, Livne, and Fineberg 2010).

$$G \cong \frac{1-v^2}{E} \frac{8l}{\pi} \sigma_\infty^2 \left(1 - \frac{v}{c_R}\right) \tag{6}$$

In this equation E is the Young's modulus, $v$ is Poisson's ratio, $v$ is the instantaneous crack speed, $l$ is the length of the crack, and $c_r$ is the Rayleigh wave velocity.  This equation contains an approximation for $K_I$ based on a stress singularity of $1/\sqrt{r}$ at the crack tip.  Specifically $K_I = K_s(\sigma_\infty, l)k(v)$ where $K_s(\sigma_\infty, l) = \sqrt{\frac{8l}{\pi}} \sigma_\infty$ and $k(v)$ is a universal function.  The $\left(1 - \frac{v}{c_R}\right)$ term causes the velocity to accelerate toward the Rayleigh velocity as the crack proceeds (Goldman, Livne, and Fineberg 2010).  The crack propagation emits acoustic waves (Achenbach and Harris 1979).  The emitted waves will have characteristic wave speeds which will interact with the crack propagation when reflected off of sample boundaries (Freund 1986).  A Rayleigh wave is a near-surface wave with a speed, $c_r$, which is dependent on material characteristics (Nkemzi 1997); it is the terminal velocity for fracture (Freund 1986).  This equation assumes an

infinite sample and does not account for the waves reflecting off of the sample boundaries and interacting with the crack tip. It also does not have an acceleration term.

Marder took a slightly different approach to the equation of motion and considered a sample with a finite width, 2b, across which the crack travels. The length of the sample is not used for the equation and the sample is considered infinite in that direction. Marder balanced the energy by setting the fracture energy, $\Gamma(v)$, equal to strain energy per unit area far ahead of the crack tip, W, and included a dimensionless acceleration $\frac{b\dot{v}}{c_l^2}$. The variable $c_l$ is the speed of the longitudinal wave that is emitted in crack propagation. Marder also uses the Rayleigh velocity as the terminal velocity for the crack. Marder arrives at the equation of motion (M Marder 1991; Michael Marder 1998)

$$\Gamma(v) = W\left(1 - \frac{b\dot{v}}{c_l^2}\left(1 - \frac{v^2}{c_r^2}\right)^{-2}\right). \tag{7}$$

Freund's formulation was shown to reasonably predict behavior in brittle gels for crack velocities less than 96% of the Rayleigh velocity (Goldman, Livne, and Fineberg 2010) and for brittle acrylic with crack velocities less than 40% of the Rayleigh velocity (Sharon and Fineberg 1999). For the case of the brittle gels, Goldman et al. found that for short times, before the crack could interact with reflected waves, the crack movement closely followed Freund's formulation but at beyond this point in time it closely follows the prediction given by Marder's equation.

These experiments were done with high speed photography (Goldman, Livne, and Fineberg 2010), a common technique for measuring crack speed (Ravi-Chandar 1998). A few techniques exist for calculating crack speed. This includes examining a sample post-

mortem and using Wallner lines to calculate the speed (Kerkhof 1973).  Wallner was the

first to explain these features often seen on fracture surfaces of brittle materials.  Wallner

lines are curved, concentric lines formed by a perturbation in the elastic field ahead of the

curve.  This perturbation is caused by the interaction between the crack front and the

shear wave (Rabinovitch, Frid, and Bahat 2006; Ravi-Chandar 1998; Andrews 1959).

Using the distance between the crack origin and the Wallner lines the speed of the crack

can be calculated in terms of the shear wave speed and the Rayleigh wave velocity

(Kerkhof 1973; Andrews 1959; Rabinovitch, Frid, and Bahat 2006).  Another technique

is the electrical resistance grid method, first used in the 1960's (Dulaney and Brace

1960).  In this method, electrically conductive lines are placed perpendicularly to the

direction of crack propagation.  The resistance of this system changes as the crack

propagates and severs the lines.  This change is recorded with respect to time and,

utilizing the distance between the lines, the crack speed can be calculated (Dulaney and

Brace 1960).  In the 1990's, a thin film of conductive material would be used in place of

discrete lines, increasing the resolution (Stalder, Beguelin, and Kausch 1983; Fineberg et

al. 1992).

The high-speed photography technique started with the Cranz-Schardin multi-

spark camera developed in the 1950's (Ravi-Chandar 1998; Garg and Siekmann 1966).

The crack speed was calculated by measuring the crack length in each frame, therefore

the accuracy of this technique is limited by the frame speed and the pixel size of the

camera.  High-speed photography then became a tool for digital image correlation (DIC)

(Pan et al. 2009).  For DIC, the sample surface is covered with a high contrast, black and

white speckle pattern.  This allows software to compare each frame in the high-speed

photography and track the pattern, providing displacement information for the sample (Pan et al. 2009).

Previous work by Sun et al. examined dynamic fracture in nanoporous gold (S. Sun et al. 2015). They used 125 µm thick nanoporous gold samples with an average ligament diameter of 40 nm, airbrushed with solid black and a white speckle pattern for DIC. A high-speed camera captured crack-propagation emanating from the tip of a notch at a frame rate of 4.34 µs as the sample is loaded at a displacement rate of 20 µm/s. They determined the Rayleigh velocity of the material to be 400 ±20 m/s and measured crack speeds up to ~ 250 m/s. Later work by Chen et al. used samples with the same average ligament diameter but pre-loaded the sample and dropped a knife on the sample edge to initiate a crack (X. Chen et al. 2020). Chen et al.'s sample dimensions adhered to the requirements for the sample to act as an "infinite strip" for the duration of the experiment. They found the maximum velocity had a linear relation to the applied, initial strain energy.

## 1.3 Stress-Corrosion Cracking and Hydrogen Embrittlement

Stress-corrosion cracking (SCC) cannot be classified as a strictly chemical attack or a purely mechanical failure. The rate of propagation is too high for a chemical attack and too low for a purely mechanical failure (Rhodin 1959). Failure that occurs by SCC is often catastrophic. Common examples of failure through SCC are nuclear reactors, high-pressure gas lines, and boilers (Staehle 2016). SCC has been attributed to different mechanisms, some of which are slip-dissolution, anodic reaction-induced cleavage, surface mobility, hydrogen embrittlement, and film-induced cleavage.

1.3.1 Stress-Corrosion Cracking Mechanisms

1.3.1.1 Slip-Dissolution

The slip-dissolution mechanism is also known as the film-rupture mechanism. In this mechanism, a protective film is subjected to a strain substantial enough to rupture it. This rupture exposes bare metal surface and metal dissolution occurs for a brief time, until the protective film reforms, thus advancing the crack some distance, L, into the plastic strain field ahead of the crack tip. Driven by the strain gradient, the strain at the crack tip accumulates until the critical strain level is again reached, passive film ruptures, and the process repeats (Vermilyea 1972; Logan 1952).

Vermilyea put forward equations to describe the slip dissolution mechanism (Vermilyea 1977b, 1972). For the plane stress case, he used the Dugdale model for the stress ahead of the crack-tip which considers the strain $\epsilon_r$, at a distance r ahead of the crack tip, measured normal to the crack plane, to be linearly related to the distance such that

$$\epsilon_r = \epsilon_\rho - \frac{\epsilon_\rho r}{R} \tag{8}$$

where $\rho$ is the radius of curvature of the crack tip, $\epsilon_\rho$ is the strain at the crack tip, and R describes the distance from the crack tip to the end of the plastic zone. The size of the plastic zone depends on several material parameters: the stress intensity parameter, K, the elastic modulus, E, and the yield strength, $\sigma_y$. The crack tip opening displacement, $\delta$, can be estimated using K, E, and $\sigma_y$. $\epsilon_\rho$ in turn is estimated from $\delta$ and the thickness of the plate containing the crack, T.

$$R = \frac{\pi K^2}{8\sigma_y{}^2} \tag{9}$$

$$\epsilon_\rho \simeq \frac{\delta}{T} = \frac{K^2}{TE\sigma_y} \tag{10}$$

The difference between the strain at the crack tip and the strain at some distance, L, must reach a critical value for the rupture to occur and advance the crack the distance, L. This difference can be written as

$$\Delta\epsilon = \frac{8\sigma_y L}{\pi TE} . \tag{11}$$

If we take the minimum $\Delta\epsilon$ required for the mechanism to be greater than or equal some critical value, $\epsilon_c$, the minimum value of L can be calculated by

$$L_{min} = \frac{\pi TE\epsilon_c}{8\sigma_y}. \tag{12}$$

However, this Dugdale model is known to be inadequate for the size of the plastic zone normal to the crack through the thickness of the plate (G. T. Hahn and Rosenfield 1965). On that basis Vermilyea suggests that instead of a linear dependence on r, a $r^{-1}$ relationship exists for $\epsilon_r$. When the equation for $\epsilon_r$ and $\Delta\epsilon$ are rewritten with the inverse dependence on r, Vermilyea arrives at

$$\epsilon_r = \frac{\epsilon_\rho \rho}{r} \tag{13}$$

and

$$\Delta\epsilon = \frac{\epsilon_\rho L}{\rho + L} . \tag{14}$$

Vermilyea then assumes that after the crack has progressed, the crack tip opening displacement will be $\delta+2L$ and that the new radius of curvature will be half of this, leading to the equation

$$\rho = \frac{\epsilon_\rho T}{2} + L . \tag{15}$$

The equation for the minimum L value, making the same assumption as before that $\Delta\epsilon$ must be greater than or equal to some critical value, $\epsilon_c$, is now

$$L_{min} = \frac{\epsilon_\rho \epsilon_c T}{2(\epsilon_\rho - 2\epsilon_c)} \; .$$
(16)

In the case of plane strain, the minimum L value is also determined by $X_o$, the ductile-rupture dimple spacing.

$$L_{min} = \frac{3\epsilon_\rho \epsilon_c X_o}{2(\epsilon_\rho - 2\epsilon_c)}$$
(17)

When the math, put forward by Vermilyea, to support the slip-dissolution mechanism is examined there are some apparent issues (Vermilyea 1972, 1977b). He oversimplifies and assumes that the center of the radius of curvature for the crack tip does not move. Additionally, the math does not account for strain to accumulate during the corrosion period between rupture and repassivation. Vermilyea used a linear plastic strain gradient for his first plane-stress calculation and a 1/r strain gradient for the second plane stress as well as the plane strain calculations. A 1/r strain gradient is the steepest strain gradient supported by theory which makes it the optimal choice as steeper strain gradients require smaller values of L (Hutchinson 1968); as Rice points out, 1/r is not a realistic strain-gradient (Vermilyea 1977a). One of the potential rate-limiting steps is the dissolution rate (Ford 1984). In the case of both plane-stress calculations, Sieradzki used realistic values and calculated $L_{min}$ values. Sieradzki then went further and, by integrating under the repassivation current, calculated substantially larger charge-densities than generally seen in a repassivating system that experiences SCC (Sieradzki 1990).

Notably Ford and Andresen added a creep term to the strain(Andresen and Ford

1988; Hall 2008). Lu and Shoji also made changes to the strain by implementing a

logarithmic strain gradient. Collectively these changes became known as the Ford-

Andresen-Shoji formulation. In this formulation, a constant crack-tip strain rate is

assumed although similar to Vermilyea's initial formulation it seems to ignore a detailed

time-dependent description of how the crack-tip moves (Roger C. Newman and Healey

2007). Lu and Shoji used a much more realistic crack tip strain dependent on K, $\sigma_y$, and

E similar to Vermilyea's original formulation. However, it introduces an inverse strain

hardening exponent, n, and other dimensionless variables, $\beta$ and $\lambda$ (Z. Lu and Shoji 2006;

Roger C. Newman and Healey 2007).

$$\epsilon_{ct} = \beta \left(\frac{\sigma_y}{E}\right) \left\{ \ln\left[\left(\frac{\lambda}{r}\right)\left(\frac{K}{\sigma_y}\right)^2\right]\right\}^{\frac{n}{n-1}} \tag{18}$$

Turnbull notes that this mechanism is no longer widely supported for

transgranular stress-corrosion (TGSCC), whose fracture surfaces appear as cleavage, and

viewed as a mechanism by which intergranular stress-corrosion (IGSCC) may occur

(Turnbull 1993). He also notes, however, that the model lacks what might be considered

realistic chemistry at the crack-tip. Another notable weak point of this model is its

sensitivity to input parameters (Roger C. Newman and Healey 2007; Turnbull 1993).


1.3.1.2 Surface Mobility

Galvele introduced an SCC mechanism referred to as the surface mobility

mechanism and claimed it could account for SCC, liquid metal embrittlement, and

hydrogen embrittlement (Jose R Galvele 1987; J. R. Galvele 1993). Unlike previous

attempts to explain SCC, this mechanism focuses on vacancies and surface diffusion.

Specifically, the mechanism proposes that if the temperature is less than half that of the

melting point of the material and the applied stress is less than the flow stress, the

environment can cause a large surface mobility which will allow cracks to grow when

surface vacancies move to the crack tip or adatoms move from the crack tip down the

side of the crack.

Galvele begins by giving an equation, which he attributes to Nabarro-Herring

creep, defining the concentration of vacancies, C, on a sample under a normal stress, σ, as

$$C = C_0 \exp\left(\frac{\sigma a^3}{kT}\right). \tag{19}$$

The $\sigma a^3$ term is the energy required to remove an atom using the stress, σ, to

expose an area, $a^2$. $C_0$ is defined as the stress-free thermal equilibrium concentration of

vacancies, T is temperature, and k is Boltzmann's constant (Jose R Galvele 1987).

Galvele goes on to derive crack velocity, $V_p$, where $D_s$ is the surface self-diffusion

coefficient and L is the distance the adatoms or vacancies diffuse (Jose R Galvele 1987;

J. R. Galvele 1993).

$$V_p = \frac{D_s}{L}\left[\exp\left(\frac{\sigma a^3}{kT}\right) - 1\right] \tag{20}$$

Galvele's argument is that the environment sufficiently increases $D_s$ to make this

mechanism viable. He suggests that one way the environment causes this increase in $D_s$

is through the formation of a salt on the metal surface whose melting point is lower than

the bulk.

Sieradzki and Friedersdorf examined several technical issues with Galvele's

surface mobility mechanism (Sieradzki and Friedersdorf 1994). In Galvele's calculations

he made the assumption that a normal stress acts on the surface of the crack, however they are free surfaces and therefore have no normal stresses acting on them. Additionally, volume relaxation around a vacancy was not considered and consequently the interactions between the vacancies and the stress field were effectively ignored. Sieradzki and Friedersdorf also point out that the vacancy concentration Galvele uses is wrong and should include second order stress terms in order to be accurate as well as consider the chemical potentials (Sieradzki and Friedersdorf 1994). They consider a situation put forth by Larche and Cahn of a cylindrical tensile bar that has been axially loaded (Larche and Cahn 1985). For that situation when lattice relaxation surrounding the vacancy is neglected, the concentration of vacancies, $c_v$, is

$$kT \ln\left(\frac{c_v}{c_v^0}\right) = \Delta\mu = -\frac{\sigma_{yy}^2}{2E}a^3 + \frac{\gamma a^3}{\rho}. \tag{21}$$

In the above equation, $c_v^0$ is the unstressed solid surface equilibrium vacancy concentration, k is Boltzmann's constant, T is the temperature, $\Delta\mu$ is the difference in chemical potential of the vacancies with respect to the unstressed condition, $\sigma_{yy}$ is the stress at the crack tip surface, E is the Young's modulus, $\gamma$ is the free energy of the solid/liquid interface, and $\rho$ is the radius of curvature of the crack tip. The second term of the equation, which includes $\gamma$, accounts for the effect of curvature on chemical potential and is responsible for driving the surface diffusion by which crack growth occurs in this mechanism. Taking into account conservation of matter and the number of lattice sites per unit area, $N_s$, Sieradzki and Friedersdorf then calculate the velocity of the crack normal to itself, $V_n$, as

$$V_n \cong \frac{D_S N_s a^6}{kT}\frac{2}{\pi\rho^2}\left(\frac{\sigma_{yy}^2}{2E} - \frac{\gamma}{\rho}\right). \tag{22}$$

30

Notably, the second-order stress terms contribute to the velocity while the first-order do not, unlike Galvele's proposal. Using realistic values for $\sigma_{yy}$, E, and $\gamma$ Sieradzki and Friedersdorf arrive at crack velocities ~14 orders of magnitude smaller for ductile FCC metals than Galvele. Therefore, although proposed as a universal SCC mechanism, it may be applicable but only in more brittle materials and at low crack growth rates.

1.3.3.3 Film-Induced Cleavage

The film-induced cleavage mechanism general concept was initially proposed by Edeleanu and Forty (Edeleanu and Forty 1960) and later explained and developed by Sieradzki and Newman (Sieradzki and Newman 1985, 1987). The mechanism seeks to explain the transgranular SCC (TGSCC) cases where ductile alloys appear to fail in a microscopically brittle manner. Proposed mechanisms often fail to address the fracture surface's cleavage-like appearance in TGSCC (J. S. Chen, Salmeron, and Devine 1992). The premise of the theory is that brittle, microcleavage fractures are initiated in a thin film on the surface of metal. A crack with enough speed will "inject" into the substrate. The film will reform on the exposed surfaces of the crack and, importantly, at the crack tip. If the crack is arrested, Sieradzki and Newman suggest that the local deformation at the crack tip can be altered by the film such that cleavage is instigated again. One particularly important aspect of this mechanism is the idea that the roles of the stress and corrosion can be decoupled.

It is put forth that the film is produced through anodic reactions between the environment and the metal and generally takes the form of a dealloyed, oxidized, chloride, or nitride layer. The time-scales associated with SCC indicate that, at ambient

31

temperature, the reaction between the environment and the metal must be limited to the surface and near-surface, lending credence to the proposal of a film over a bulk effect. Sieradzki and Newman note that nucleation of the cleavage is easier to envisage if this film is brittle but assert that even if the film is not brittle, the mechanism may still hold under specific conditions (Sieradzki and Newman 1985).  Sieradzki and Newman provide a list of film parameters they believe are integral to the mechanism: lattice parameter misfit, elastic modulus mismatch, interfacial state of coherency, degree of interfacial bonding, shape of film around crack, porosity, and inherent ductility or brittleness (Sieradzki and Newman 1987).  In the case of brass the layer is created by dezincification (dealloying) where zinc is removed and the layer has a lower amount of zinc than the bulk material.  Silver-gold and copper-gold alloys can be similarly dealloyed, yielding a layer of nanoporous gold ligaments.  Depending on the dealloying rate, the diameter of the ligaments can vary.

A crack can arrest in the ductile or semi-brittle material due to unbroken ligaments connecting the film at the bulk, collisions with defects (either generated by the deformation process or previously existing within the material), crack bifurcation, or exhaustion as the crack's velocity is decreased by the emission of dislocations during propagation.  The ligaments effects on crack arrest is unlikely for several reasons: ligaments can be very small (on the order of tens of nanometers), the portion of the ligament that can be involved in arrest is small, arrest seems to be inherent to the dynamic crack as arrest marks appear continuously on steps of varied heights.  Edeleanu and Forty saw cracks arrest at slip bands, providing the case for arrest at defects (Edeleanu and Forty 1960). However, a defect is not always present at the site of arrest.

32

Sieradzki and Newman argue that the evidence supports the exhaustion arrest process (Sieradzki and Newman 1987). Some research has provided evidence that dislocations are generated at the crack-tip in conjunction with the cleavage (Gilman 1956). Additionally, in molecular dynamics simulations by Dienes and Paskin (Sieradzki et al. 1988), just after a dislocation is created the cleavage process is momentarily halted and resumes when the dislocation is sufficiently far from the crack-tip. This results in a discontinuous, crack-jumping progression.

The film-induced cleavage mechanism has research to support it. Sieradzki and Newman examined TGSCC of α-brass under fixed displacement in sodium nitrite (R. C. Newman and Sieradzki 1983). An acoustic emission sensor used in tandem with the potentiostat allowed the corrosion and the cracking to be measured separately. This data showed that the TGSCC was occurring discontinuously. Later additional work on α-brass was done by Newman, Shahrabi, and Sieradzki (R. C. Newman, Shahrabi, and Sieradzki 1989). These were done at varying strain rates and used cuprous ammonia. In one experiment the sample was strained to fracture in the electrolyte, while in other experiments the sample was removed from the electrolyte after dealloying. In the cases where it was removed it was either immediately rinsed in water and methanol before being fractured, dried before frozen in liquid nitrogen and then fractured, or immediately frozen in liquid nitrogen and fractured. When the brass was fractured in the electrolyte, it exhibited brittle behavior at slow and fast strain rates as well as displaying a single event. The experiments that incorporated rinsing in water and methanol and drying before freezing served to show that the experiment that fractured in electrolyte did not fail exclusively due to a stress corrosion crack propagating. The experiment where the

sample was frozen in liquid nitrogen immediately following the dealloying and fractured

yielded a brittle crack which supports the idea that the roles of stress and corrosion can be

decoupled. Although the results of these experiments showed TGSCC, Newman,

Shahrabi, and Sieradzki suggest that previously seen intergranular fracture in brass could

be occurring by the same mechanism (R. C. Newman, Shahrabi, and Sieradzki 1989).

Pugh examined brass TGSCC fracture surfaces in an SEM and was able to confirm the

crack-jumping phenomenon by analyzing the crack arrest marks (Pugh 1985). Hahn and

Pugh were similarly able to confirm the discontinuous progression of TGSCC in stainless

steel (M. T. Hahn and Pugh 1980).

In addition to the research on brass, the film-induced cleavage mechanism was

also studied in noble-metal alloys. Noble metals alloys serve as a good model system for

studying SCC because in the cases of copper-gold alloys and silver-gold alloys hydrogen

embrittlement can be ruled out. Additionally the dealloying of these alloys can be

controlled potentiostatically. Chen, Salmeron, and Devine studied the film induced

cleavage mechanism in copper-gold alloys (J. S. Chen, Salmeron, and Devine 1993,

1992; J. S. Chen 1992). They found that depending on the amount of stress, it could be

determined whether the SCC would occur intergranularly or transgranularly. The type of

fracture could change as the crack propagates through the thickness and the stress

distribution changes. More importantly, their results indicated that the same mechanism

was responsible for both intergranular stress-corrosion cracking (IGSCC) and

transgranular stress-corrosion cracking (TGSCC) in the copper-gold system. Kelly et al.

studied silver-gold alloys and obtained brittle IGSCC (Kelly et al. 1991). These

experiments also found that when the dealloyed layer is allowed to coarsen, it again

34

becomes ductile.  Kelly et al. characterized this coarsening by measuring interfacial

capacitance of the dealloyed layer.

Saito et al. went on to confirm the coarsening of the porosity and determine that it

was controlled by surface diffusion as well as being dependent on time and potential

(Saito, Smith, and Newman 1993).  In their studies on silver-gold alloys, Sieradzki and

Friedersdorf examined the effects of the thickness of the dealloyed layer on the crack

penetration depth (Friedersdork and Sieradzki 1996). They found that when the layer is

>150 nm, the relationship between the crack penetration depth and the layer thickness is

linear.  Barnes, Senior, and Newman worked to induce entirely intergranular or

transgranular fracture in silver-gold foils and wires (Barnes, Senior, and Newman 2009).

These results showed that the coarsening (ageing) occurs at different rates depending on

the applied potential used to induce dealloying.  They also noted the idea that the

corrosion was progressing much further down the grain boundaries causing IGSCC could

be ruled out since thinner dealloyed layers often were more effective at enabling IGSCC.

Although research done in support of the film-induced cleavage mechanism has

been heavily focused on brass and noble metal alloys, some research has been done

which shows that this mechanism also applies to stainless steel(M. T. Hahn and Pugh

1980) and rhodium plated nickel(Ricker et al. 1992).


1.3.2 Hydrogen Embrittlement

Hydrogen-assisted cracking, otherwise called hydrogen-embrittlement, is a

significant topic, particularly for stainless steels which exhibit noticeably different

fracture behavior in a hydrogen environment (Perng and Altstetter 1987; Oriani 1978).

Some metals form metal hydrides which are brittle (Birnbaum 1984). This 'hydride-embrittlement' can be treated as film-induced cleavage and therefore will not be addressed here. Many mechanisms for hydrogen embrittlement have been proposed over the years (Robertson et al. 2015): hydrogen induced reduction in surface energy, hydrogen-enhanced dislocation ejection, hydrogen-enhanced decohesion, hydrogen-enhanced localized plasticity, hydrogen-assisted vacancy production, hydrogen-induced ductile to brittle transition, and hydrogen-induced phase transformation. Of these, the hydrogen-enhanced localized plasticity (HELP) and hydrogen-enhanced decohesion mechanisms are the most popular so the following will be restricted to these two.

Hydrogen atoms can be absorbed by metals. High strength martensitic steels, moderate strength ferritic steels, and titanium alloys are particularly susceptible while austenitic steels, nickel alloys, and aluminum alloys are less susceptible but can still suffer (Lynch 2011). Hydrogen can come from many places such as cleaning solutions, atmosphere, and aqueous electrolytes or environments (Lynch 2011). If $H_2S$ is present in the aqueous, sulfur adsorption will facilitate hydrogen absorption (Roger C. Newman 2002). Alternatively, in the case of aqueous electrolytes and environments, hydrogen can be formed by the reduction of water:

$$H^+ + e^- \rightarrow H \tag{26}$$

$$H_2O + e^- \rightarrow H + OH^- . \tag{27}$$
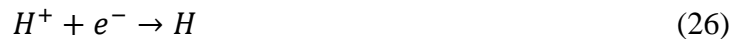
During fracture, the strained crack-tip will have the highest hydrogen atom generation of the newly exposed metal (Turnbull 1993) as plastic deformation can increase transportation rates of hydrogen (Scully 1977). Among other sites, the hydrogen can become trapped at free surfaces, vacancies, dislocation cores, and grain boundaries

(Lynch 2011). Up to a point, increasing the hydrogen pressure will increase susceptibility to hydrogen embrittlement (Lynch 2011). Ambient temperatures are often the most ideal for hydrogen embrittlement (Lynch 2011). Additionally susceptibility is affected by the strain rate (higher strain rates are less vulnerable), microstructure (twins in martensite increase its susceptibility, grain size also affects susceptibility), and impurity content (higher strength materials are less susceptible but too many impurities will make it more susceptible) (Lynch 2011).

1.3.2.1 Hydrogen-Enhanced Decohesion

The decohesion model was proposed by Oriani (Oriani 1972) and built off of earlier models that had been proposed by Petch and Stables (Petch and Stables 1952) and Troiano (Scott and Troiano 1960). Petch and Stables initial proposal was that a stress concentrator would cause hydrogen adsorption, lowering the surface free energy and thereby lowering the Griffith criterion for cracking. Oriani uses this as his thermodynamic starting point in combination with Troiano's work that suggested that hydrogen can be concentrated at a crack tip due to elastic stresses and cause decohesion in the lattice (Scott and Troiano 1960). Oriani asserts that his decohesion model differs from Troiano's because it theorizes that hydrogen embrittlement cracking is intrinsically continuous and any discontinuous behavior results from inhomogeneities in the material as well as requiring a different magnitude of elastic stress to induce cracking (Oriani 1972).

Oriani then conducted experiments where he measured the plane-strain stress intensity factor, K, of AISI 4340 steel in different pressures of hydrogen and deuterium

(Oriani and Josephic 1974). From this data he then fit an equation to the decohesion theory. First, Oriani incorporates a Langmuir isotherm into the Petch modification of the Griffith criterion in order to achieve a linear relationship between the natural logarithm of pressure of hydrogen and the stress intensity factor which he found from his experiments. Then Oriani adjusts for an increasing radius of curvature at the crack-tip to match his experimental findings.

Detecting hydrogen can be a very difficult task and to truly verify the decohesion model, the effects of hydrogen on the cohesive force between atoms in an alloy should be measured.


1.3.2.2 Hydrogen-Enhanced Localized Plasticity

The HELP model proposes that concentrated hydrogen at the crack tip assists the deformation processes allowed by the microstructure. It proposes that instead of hydrogen embrittling a material, it instead affects the plasticity. Beachem proposed the HELP mechanism based on a series of experiments that were devised to test the previously proposed interactions between hydrogen and steel (Beachem 1972). He summarizes these interactions as: hydrogen is created and absorbs at the crack tip in aqueous SCC and charging, fracture surfaces serve as sites to dissociate hydrogen gas which is then absorbed into the metal, hydrogen migrates to the crack-tip due to the stress concentration, and hydrogen in the metal aids deformation. The first experiment was to test the mode of fracture, the second was to examine macroscopic flow properties, and the third was to eliminate issues associated with electrochemical charging.

The first experiment was done in an aqueous electrolyte with two types of steel which were known to crack via a microvoid coalescence mechanism during SCC.  SCC and hydrogen-assisted cracking was performed on the steel and the resulting fracture surfaces were examined.  Both types of steel failed by microvoid coalescence in both SCC and hydrogen-assisted cracking.  Ultimately Beachem concluded that no identifying fracture marks resulted from hydrogen-assisted cracking which could assist in determining whether failure could be ascribed to SCC or hydrogen embrittlement.

The second experiment monitored the internal pressure of both uncharged steel and hydrogen-charged steel during torsion in addition to the torque and extent of torsion. The uncharged steel did not see a rise in pressure but the charged steel pressure rose until the metal yielded at which point the pressure remained constant until the experiment was stopped.  Beachem argues that this indicates that the deformation was trapping the hydrogen.  The torque required by the charged specimen was noticeably diminished compared to the uncharged, confirming that hydrogen reduced flow stress.

In the third experiment, steel was exposed to hydrogen gas in the absence of an aqueous environment.  The steel was alternately fatigued and held in tension in the hydrogen rich environment until it failed during fatigue.  When Beachem examined the fracture surfaces, there were small dimpled regions indicating that, while being held in tension, hydrogen assisted cracking had occurred via the microvoid coalescence mechanism.  Additionally there appeared to be cleavage-like fracture surfaces that are not seen under normal fatigue conditions.

Beachem argues that the prevalence of the microvoid coalescence mechanism of failure indicates that a model for hydrogen assisted cracking should be focused on

39

microscopic plasticity and not on embrittlement.  Generally it is believed that HELP

operates by enhancing dislocation movement or inducing slip (Birnbaum and Sofronis

1994).  More recent simulations by Song and Curtin have disproven these interactions

between hydrogen and dislocations (Song and Curtin 2014). It is also worth noting that in

the first experiment, the role of hydrogen cannot be completely discounted in what

Beachem prescribes to purely SCC.


1.3.2.3 Superabundant Vacancies

Some metals, notably those with hydrogen solubility, experience a lattice

expansion in the presence of elevated hydrogen pressures (Baranowski, Majchrzak, and

Flanagan 1971).  Fukai and Okuma noticed, however, that for Pd and Ni the lattice

parameter was reduced when held at high temperature and high hydrogen pressure for

more than two hours.  When ambient temperature and pressure was restored, the

decreased lattice parameter was retained.  The lattice parameter could revert to the initial

value when the metal was annealed, however.  From this they concluded that a large

number of metal atom vacancies had been introduced to the material, allowing the lattice

parameter to be reduced (Yuh Fukai and Okuma 1993).   It was also found that for nickel

and copper this superabundant amount of vacancies can be introduced through

electrodeposition where metal and hydrogen atoms are deposited concurrently (Y. Fukai

et al. 2003).  Osono et al. saw that after the anneal in nickel samples, voids form owing to

the agglomeration of hydrogen vacancies (Osono et al. 1995).  The superabundant

vacancies formation has also been seen in other metallic systems like copper (Yuh Fukai

2003), aluminum (G. Lu and Kaxiras 2005), cobalt (Yuh Fukai, Yokota, and Yanagawa

2006), chromium (Y Fukai and Mizutani 2002), iron (Y. Fukai, Mori, and Shinomiya 2003; Iwamoto and Fukai 1999), stainless steels (Gavriljuk et al. 1996), and some metal hydrides (Yuh Fukai and Sugimoto 2007).

Nazarov et al. examined hydrogen atom interactions with vacancies in FCC metals using density functional theory and found that multiple hydrogen atoms can be trapped by a vacancy but $H_2$ molecules are not thermodynamically stable in many FCC materials. The study also showed that the trapping of multiple hydrogen atoms by a vacancy would occur before reaching the point where the metal would transform into a hydride (Nazarov, Hickel, and Neugebauer 2014). Trapping hydrogen atoms causes the energy of formation for a vacancy to be reduced, making the superabundant void structure stable (Y. Fukai et al. 2003).

Previous research on palladium had shown that dissolved hydrogen increased the diffusion of metal atoms and modified the equilibrium state of a palladium-manganese or palladium-ruthenium alloy at elevated temperatures (Flanagan and Noh 1995). This increase in diffusion was termed hydrogen-induced lattice mobility and is now believed to be an effect of the superabundant vacancy structure. Experimental results on electrodeposited copper indicate that an additional effect of the superabundant vacancy structure is enhanced creep (Yuh Fukai 2003). Based on the evidence that the superabundant vacancy structure can be formed in iron (Iwamoto and Fukai 1999; Y. Fukai, Mori, and Shinomiya 2003) and stainless steels (Gavriljuk et al. 1996) in combination with the structure's ability to change diffusion and creep, it has been theorized that this may be a mechanism for hydrogen embrittlement. Fukai theorizes that

the superabundant vacancies structure is formed at a crack tip in steels (Yuh Fukai 2003)

and this structure allows for the hydrogen embrittlement type fracture.

CHAPTER 2

NANOPOROUS GOLD FROM ORDERED AND DISORDERED PHASES

A common alloy used to study NPG is Cu-Au.  It has some of the same advantages as the silver-gold system.  Although copper-gold has a slightly higher hydrogen solubility, it is still very minimal and allows hydrogen embrittlement to be discounted as the cause of fracture so the system can be used to study stress-corrosion cracking as well.  Copper, like silver and gold, is an FCC material.  Copper gold binary alloys form a perfect FCC solid-solution over a large composition range eliminating a phase change between the parent phase and resultant NPG.  However, unlike the silver-gold system, copper-gold can also take on an ordered structure in the composition range relevant to the formation of NPG.  Specifically, 75 at% Cu – 25 at% Au can be FCC solid-solution or become $Cu_3Au$ with the $L1_2$ structure, in Strukturbericht notation, where Cu atoms sit at face-centered positions and the corner positions are Au atoms (H. Okamoto, Chakrabarti, and Laughin 1987).  This presents an excellent opportunity to study the effects of a phase-change and ordering on the characteristics of the resultant NPG while eliminating factors such as differing compositions and materials that may confound this in other systems.  Two characteristics potentially affected by a phase change are the crystal orientation of the NPG as it relates to the parent phase, and the morphology of the ligaments.

2.1 Effects on Orientation

It has long been assumed that silver-gold and copper-gold retain the crystallographic orientations of their grains when they undergo dealloying to form NPG

43

due to their lack of phase change. Since surface reorganization during dealloying occurs through surface diffusion, it is not unreasonable to believe that the material will retain the orientations of the underlying parent phase because this should create the least amount of misfit and strain, the same principal as epitaxial film growth (Vook and Oral 1987).

There is some experimental proof that the orientation is retained in the silver-gold system during dealloying from Petegem et al. who utilized X-ray diffraction and X-ray microdiffraction techniques to obtain Laue diffraction patterns on pre and post dealloyed silver-gold (Van Petegem et al. 2009). The Laue diffraction patterns indicate that the crystallographic orientations are retained during dealloying.

Despite the large amount of research that has been done on NPG with a variety of techniques, there is a noticeable lack of electron backscatter diffraction (EBSD) work. Historically, EBSD on soft, noble-metal alloys like silver-gold and copper-gold has been difficult. Traditionally in order for EBSD to be performed on a metal surface, it is polished down until it is extremely flat. Chen found that a heat treatment was needed on silver-gold immediately preceding the EBSD (X. Chen 2016). Despite being considerably less than what would be considered ideally flat, these heat-treated surfaces can yield very clean EBSD. Heat treating NPG coarsens the ligaments, therefore it cannot be guaranteed that after heat treatment the surface orientation is identical to the 'as-dealloyed' surface.

EBSD work on NPG by de Jeer used work-hardened silver-gold leaf as the parent alloy (De Jeer et al. 2015). This is not good for comparison between before and after dealloying because the material has stresses from being work-hardened. It is not

unreasonable to presume that the surface reorganization required to form the NPG will also remove some of the stress, potentially changing grain orientations in the process.

A procedure was developed to allow for EBSD on NPG in order to interrogate the 'as-dealloyed' surfaces of silver-gold and copper-gold alloys. This, in turn, was used to determine if any change in grain size or orientation occurred during dealloying.

2.2 Effects on Morphology

A lot of nanoporous metal research has been done on solid solutions like Ag-Au and Cu-Au, but research on dealloying-created nanoporosity from ordered metals, like Li-Sn and Li-Pb, has also been done. There are not many binary alloys suitable for electrochemical formation of nanoporosity which can have both a solid solution (disordered) and ordered structure. Until now, no nanoporosity from ordered and disordered parent phases of the same material has been examined. Therefore, it has been impossible to attribute any morphological differences to a phase change occurring during dealloying because they could be attributed to the differences in initial concentrations of the less noble component or different less noble alloy components all together.

It is known that changing the less noble component in an alloy with ordered phases can affect the morphology. Chen and Sieradzki examined the morphology from the dealloying via free corrosion of four different binary lithium alloys: Li-Sn, Li-Pb, Li-Cd, Li-Bi (Q. Chen and Sieradzki 2013). The four nanoporous morphologies showed variation in both ligament size and roughness. They also examined morphology resulting from three different compositions in Li-Sn nanoparticles and found similar results. Changes in composition (30, 48, and 77 at% Li) affected the roughness as well as

45

creating voids in the ligament structure for the composition of 30 at% Li and an entirely

hollow particle center for 48 at% Li while 77 at% resulted in a bicontinuous morphology

similar to NPG obtained from Au-Ag.  Geng et al. (Geng et al. 2019) found similar

results for Li-Pb nanoparticles; 20 at% Li yielded negative dendrites, 50 at% Li had voids

and nodes, 70 at% Li produced a bicontinuous structure, and 75 at% Li showed an

anisotropic, roughened nanoporous structure.

One of the more well-studied alloys that forms a bicontinuous nanoporous

morphology, Cu-Au, can be both ordered and disordered at the concentration of 75 at%

copper which lies above the parting limit of ~ 60 at% copper.  This work exploits this

ability to interrogate whether starting with an ordered phase or random solid solution

change results in a different post-dealloying morphology (Tse, Karasz, and Sieradzki

2020).  Determining the impact of an ordered parent phase on the morphology caused by

dealloying will help to inform the understanding of the kinetic processes involved in

nanoporosity formation.

2.3 Methods

A sheet of 75 at% copper and 25 at% gold, 100 μm thick, was purchased from

ESPI Metals and the composition was verified using energy-dispersive X-ray

spectroscopy (EDS) on a Philips XL30 ESEM-FEG (Cu Kα).  Pieces 5 mm by 12 mm

were cut, polished with silicon carbide paper followed by an alumina suspension to 0.05

μm.  The samples were then encapsulated in quartz ampules and backfilled with 5%

$H_2$/Ar to 0.5 atm to prevent samples from oxidizing during heat treatments.  Samples

were disordered (FCC solid-solution) through a heat treatment of 850° C for 72 hours

followed by a water quench.  To order the copper-gold and create the $L1_2$ structure, a

procedure published by Seker et al.  was followed (Seker, Shih, and Stine 2018).

Samples were held at 850° C for 72 hours, lowered to 380° C for 72 hours, and lowered

by 10° C every 24 hours following until the sample reached room temperature.  X-ray

diffraction (XRD) was done on a Bruker D8 Multipurpose Powder X-ray Diffractometer

to verify the structures.  The peaks, seen in Fig 2.1, were consistent with previous XRD

data on ordered and disordered $Cu_{0.75}Au_{0.25}$ from Parks et al. (Parks, Fritz, and Pickering

1989).
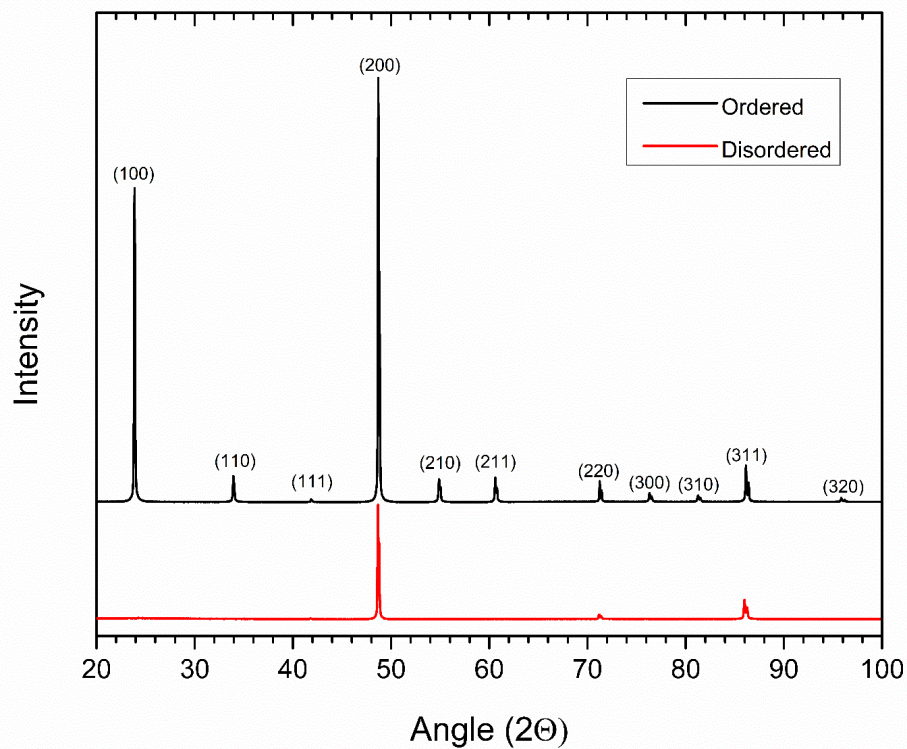


Figure 2.1: X-ray Diffraction of 75 at% Copper and 25 at% Gold, Ordered (Black) and
Disordered (Red) Samples. (Tse, Karasz, and Sieradzki 2020)

47

One corner of each sample was cut off to serve as a location marker for the EBSD before being gently attached to an SEM stub with carbon tape. EBSD was performed on the 'as heat-treated' surfaces with a Zeiss Auriga FIB-SEM and the grain size and orientation examined. It is important to note here the lack of polishing after heat-treatment which is crucial to the success of the EBSD and, in the case of the ordered samples, maintains the $L1_2$ structure which would be disturbed by polishing. In order to remove the sample without deformation, the adhesive of the carbon tape was "dissolved" using isopropyl alcohol (IPA) and then the surface that had been attached to the SEM stub was gently wiped using a sterile cotton swab and IPA. It is important to avoid bending the sample during removal.

For electrochemical testing and dealloying, the samples were laid on mica coated in gold and secured by wrapping gold wires around both layers. The gold wire was wrapped to try and evenly distribute it across the length of the sample. They were lightly pressed with a gloved finger to ensure electrical contact. The gold wires were left long enough that the mica could rest at the bottom of a beaker and protrude from the electrolyte in order to be connected to the potentiostat. Supporting the sample with the mica minimized any premature fracturing and allowed the entire sample to more consistently dealloy at the same rate.

The critical potentials for the ordered and disordered alloys were obtained by performing linear sweep voltammetry (LSV) in a three-electrode setup with a Gamry PCI4/300 potentiostat. The reference electrode was a saturated calomel electrode, platinum mesh was the counter electrode, and the electrolyte was 0.5 M $Na_2SO_4$ +0.005 M $H_2SO_4$. The voltage was swept at a rate of 0.1 mV/s from 384 to 1394 mV vs a

standard hydrogen electrode (SHE).  The critical potentials of the ordered and disordered

samples were 1074 and 824 mV (vs SHE) respectively consistent with the work of Parks

et al. (Parks, Fritz, and Pickering 1989).
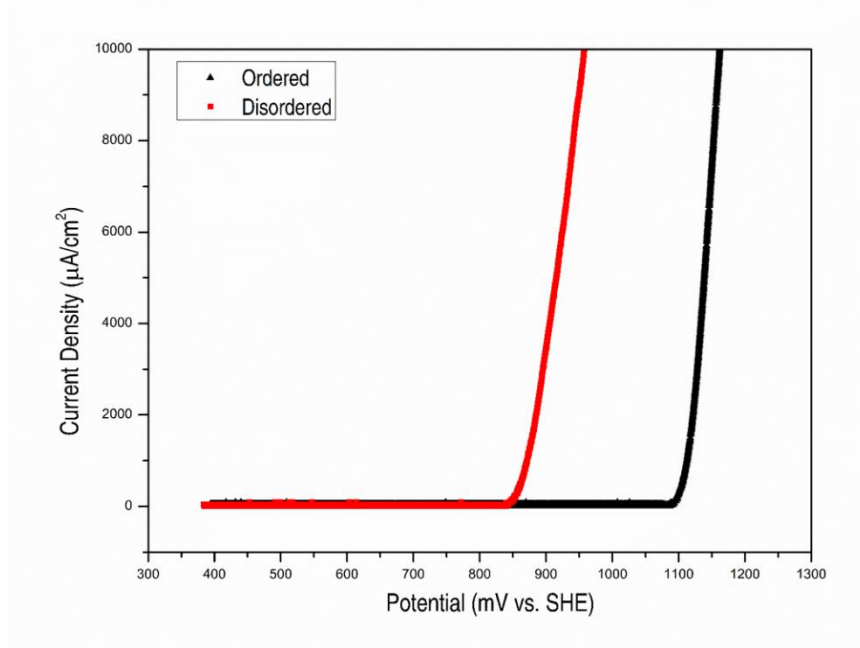


Figure 2.2: Linear Sweep Voltammetry of 75 at% Copper and 25 at% Gold Samples, Ordered (Black) and Disordered (Red) at a Rate Of .1 mV/s (Tse, Karasz, and Sieradzki 2020)

This difference in critical potential is another indication of a difference in

structure and surface diffusion rates.  In accordance with the work published by Rugolo

et al. (Rugolo, Erlebacher, and Sieradzki 2006) the difference between the ordered and

disordered critical potentials ($V_{ordered}$, $V_{disordered}$) is dependent on the length scale of

copper clusters on terraces ($\xi$) and the ordering energy resulting in

$$\Delta V = V_{ordered} - V_{disordered} = \frac{4\gamma_{Au/elec}\Omega}{nq}(\xi^{-1}_{ordered} - \xi^{-1}_{disordered}) + E_{ordering} \quad (28)$$

49

where $\gamma_{Au/elec}$ is the interfacial free energy between the gold and the electrolyte (1.27

$J/m^2$) (Rugolo, Erlebacher, and Sieradzki 2006), $\Omega$ is the volume of a copper atom (1.2 x

$10^{-29}$ $m^3$), q is the elementary charge, and $n$ is the number of electrons transferred per

copper atom during dissolution (2 electrons). The calculation of the length scale for the

disordered alloy, $\xi_{disordered}$, arises from percolation theory concepts pertaining to perfect

solid solutions. Taking $\chi_{Cu}$ as the copper atomic fraction in the parent alloy (0.75) and $a$

as the first nearest neighbor spacing for the parent alloy (0.2654 nm), the length scale for

the disordered alloy can be calculated as

$$\xi_{disordered} = \frac{(1+\chi_{Cu})}{(1-\chi_{Cu})}a = 7a. \tag{29}$$

The ordered length scale cannot be calculated using percolation theory arguments

as they apply only to solid solutions. Based on low index surfaces and normal cross-

sections for the L1$_2$ structure of the ordered alloy, it is estimated that $\xi_{ordered}$ is ~2a. The

energy of ordering can be calculated several different ways, each yielding a slightly

different value. If the energy to order the system is k$_B$T where T is 663 K, the

temperature required to achieve the L1$_2$ structure in Cu$_{0.75}$Au$_{0.25}$, the energy to order the

system is 57 mV (B. H. Okamoto and Massalski 1983). Zhang et al. calculated the heat

of formation for the ordered alloy using first-principles density functional theory (DFT)

and got values of 44 mV and 71 mV using two different approaches (Zhang, Kresse, and

Wolverton 2014), while Ozolins et al. used a third DFT approach and calculated a value

of 37 mV (Wolverton, Zunger, and Ozolin 1998). The mean ordering energy from these

calculations is ~14 mV. Orr used calorimetery to calculate the heat of formation and got

a value of 23 mV (Orr 1960). Using the mean ordering energy from the three DFT

calculations, $\Delta V$ is ~273 mV which is close to the difference of 250 mV obtained from

the LSV.  These values are acceptably close to each other due to the number of inexact

variables used in the calculation, namely $\xi_{ordered}$.

The samples were dealloyed at a constant current density of 1 mA/cm$^2$ in the

same three-electrode setup used for the LSV above, resulting in the curves seen in Figure

2.3.  This current density was chosen to ensure the dissolution rate would allow for the

formation of porosity, as the corresponding voltage from the LSV lay above the critical

potential, while still dealloying slowly.  The difference of ~250 mV in critical potentials

is reflected in the first ~1.5 hours of the chronopotentiometry seen in the inset of Figure

2.3.  The difference in applied voltages eventually drops to ~30 mV, most likely due to a

difference in surface mobilities between the ordered and disordered phases.  The

dealloying was considered completed when, after staying low for over 24 hours, the

applied voltage increased sharply.  The samples were allowed to sit at this higher voltage

for ~12 hours to remove any further copper.  This increase is attributed to oxygen

evolution beginning to occur due to a lack of copper atoms available to be removed from

the sample.  The full process took approximately 2.5 days.  The process of removing,

rinsing, and mounting the sample is the key to being able to perform EBSD on the as-

dealloyed surface.
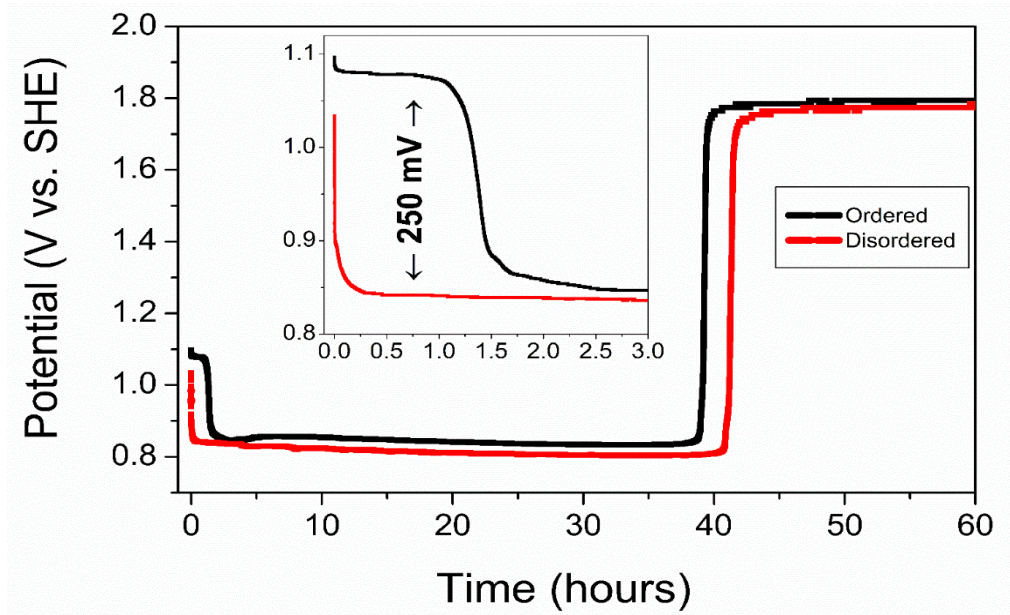
Figure 2.3 Galvanostatic Dealloying of 75 at% Copper and 25 at% Gold, Ordered (Black) and Disordered (Red) Samples at a Current Density of 1 mA/cm$^2$. (Tse, Karasz, and Sieradzki 2020)

It is crucial that the samples not experience any stress. Something as simple as dropping the sample from a short distance can prevent the ability to do EBSD. The force needed to obscure EBSD is so small, that in some cases where EBSD was not possible, the NPG surface lacked any signs of deformation. The mica and sample were removed by slowly lifting them from the acid by the protruding gold wires and then lowered into a beaker of nanopure water, allowing the mica to come gently to rest on the bottom of the beaker. After several hours in the nanopure water, the mica and sample were removed again by slowly lifting them by the gold wires out of the liquid. The sample was then rinsed with IPA, but to avoid stressing the surface the IPA could not be applied directly to the sample. Instead, the IPA was put on the mica and then the mica was tilted to move the liquid onto the sample. The sample was then allowed to dry. To remove the sample from the mica, tweezers were used to hold the mica steady, being careful to make sure

they did not come into contact with the sample, while another pair of tweezers was used to, as gingerly as possible, remove the gold wires that secured the sample. The mica was then gently overturned into an open, gloved palm and the mica slowly slid off of the sample. It is important that the sample not drag or slide across the hand. With the mica removed and sample in hand, an SEM stub with carbon tape was gently lowered until it just made contact with the back of the sample. No additional pressure was applied. The SEM stub was then flipped right-side up and placed in a sample box. EDS was done to examine the post-dealloying composition. To examine the effects on orientation, EBSD was conducted on the dealloyed samples in the same places as before dealloying. The EBSD and EDS was conducted on a Zeiss Auriga FIB-SEM.

There are minimal differences between the preparation of samples used for orientation and those used for morphology. The samples used to examine the morphology did not require EBSD before or after dealloying. Although the fragile nature of NPG usually necessitates the need for gentle handling, these samples are easier to handle because the surfaces were not going to be studied. Instead, these samples were cross-sectioned with a razor blade so that the ligaments on the interior of the sample could be analyzed for morphological purposes. Interior ligaments are used because the surfaces have a higher chance of becoming deformed during handling, and the surface ligaments are consistently a different size than that of the interior in NPG from both Cu-Au and Ag-Au. The cross-sections were examined and micrographs taken in a Nova 200 NanoLab UHRFEG SEM. Digital image analysis was then performed using an open source python program developed initially for nanoporous metals, Aquami (Stuckner et al. 2017).

2.4 Results and Discussion

Using a Zeiss Auriga FIB-SEM, EDS was done post-dealloying on the surfaces of

the samples which confirmed that, in both the ordered and disordered samples, the

majority of the copper was removed.  The amount of copper retained was measured to be

between 0 and 2.32 at% for the ordered and 0.18 and 1.79 at% for the disordered, as seen

in Table 2.1 below.  The sample size is not large enough to draw any conclusions from

this difference in spread.  Qualitatively, there was no clear correlation between the

amount of copper retained and how close or far the collection site was from the edge of

the sample.

| Ordered | | Disordered | |
|---|---|---|---|
| Cu | Au | Cu | Au |
| 0 | 100 | 0.18 | 99.82 |
| 0 | 100 | 0.44 | 99.56 |
| 0.28 | 99.72 | 0.7 | 99.3 |
| 0.62 | 99.38 | 1.04 | 98.96 |
| 0.95 | 99.05 | 1.13 | 98.87 |
| 1.08 | 98.92 | 1.2 | 98.8 |
| 1.17 | 98.83 | 1.4 | 98.6 |
| 1.2 | 98.8 | 1.46 | 98.54 |
| 1.24 | 98.76 | 1.68 | 98.32 |
| 2.32 | 97.68 | 1.71 | 98.29 |
| | | 1.79 | 98.21 |

Table 2.1:  EDS Results in Atomic Percent from Surfaces of Dealloyed Ordered and
Disordered $Cu_{0.75}$ $Au_{0.25}$ Samples (Tse, Karasz, and Sieradzki 2020)

EBSD was found to be successful when following the described procedure, despite the surface being qualitatively rougher than is generally advisable for EBSD. A representative SEM of a $Cu_{0.75}Au_{0.25}$ as-dealloyed surface where EBSD was possible is seen in Figure 2.4.
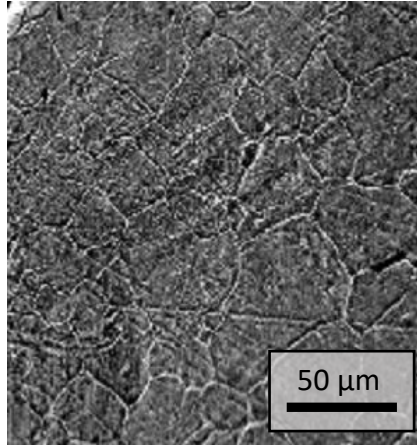


Figure 2.4: SEM Image of Post-dealloyed $Cu_{0.75}$ $Au_{0.25}$ Showing Surface Roughness Where EBSD Was Still Possible.

2.4.1 Orientation

Figure 2.5 shows the EBSD before and after dealloying for both ordered (Figure 2.5 A and B) and disordered (Figure 2.5 C and D) samples. In both cases, the grain shape and orientation are largely retained. There is a slight change in color for some of the grains, suggesting that a minor shift may have occurred in grain orientation. The large, dark blue section at the top of Figure 2.5 B is a result of handling. There are no appreciable differences between the ordered and disordered in terms of changes to the

orientations. The effects of the phase change from L12 to FCC may be minimized because they are both cubic and fairly similar in atomic placement.
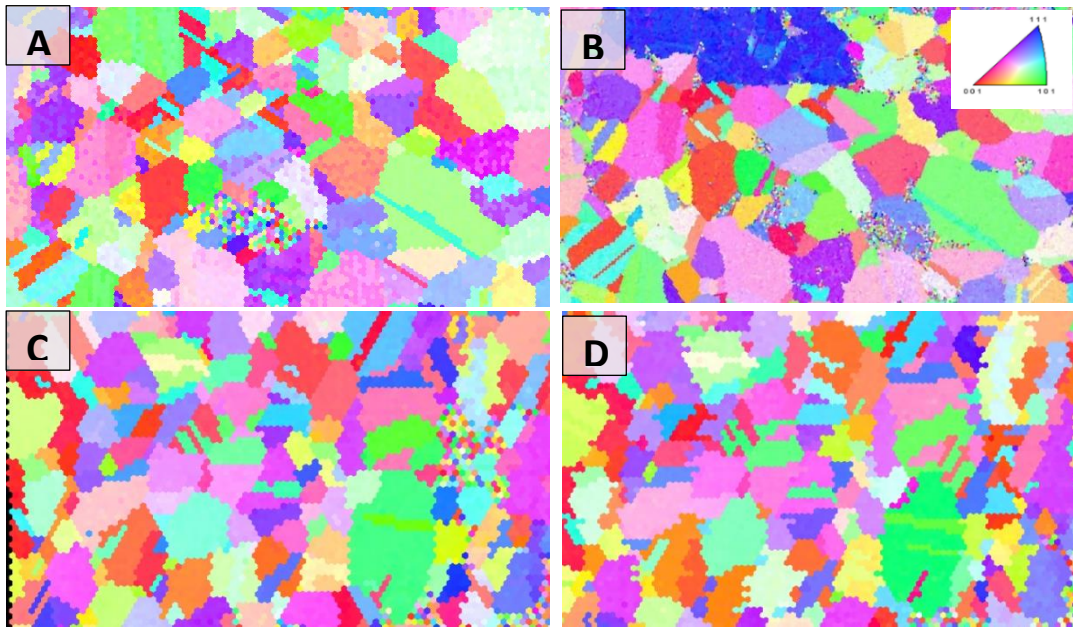


Figure 2.5 EBSD Grain Orientation Maps of Ordered and Disordered Samples Over the Same Region of the Samples Pre and Post Dealloying. (A) Ordered Parent Phase and (B) Resultant NPG. The Blue-colored Region in the Upper Left Region of the Image Resulted From Sample Handling. (C) Disordered Parent Phase and (D) Resultant NPG. (Tse, Karasz, and Sieradzki 2020)

Although silver, copper, and gold are all FCC, there is a lattice misfit due to this size difference. Silver and gold have a lattice misfit of 0.2% while copper and gold have a lattice misfit of 11.4%. In order to rule out this large lattice misfit as the source of the slight orientation changes in the copper-gold grains, silver-gold was also examined. Silver-gold was expected to retain grain orientations and shapes better than the copper-gold system overall based on the lack of phase change as well as the smaller lattice misfit.
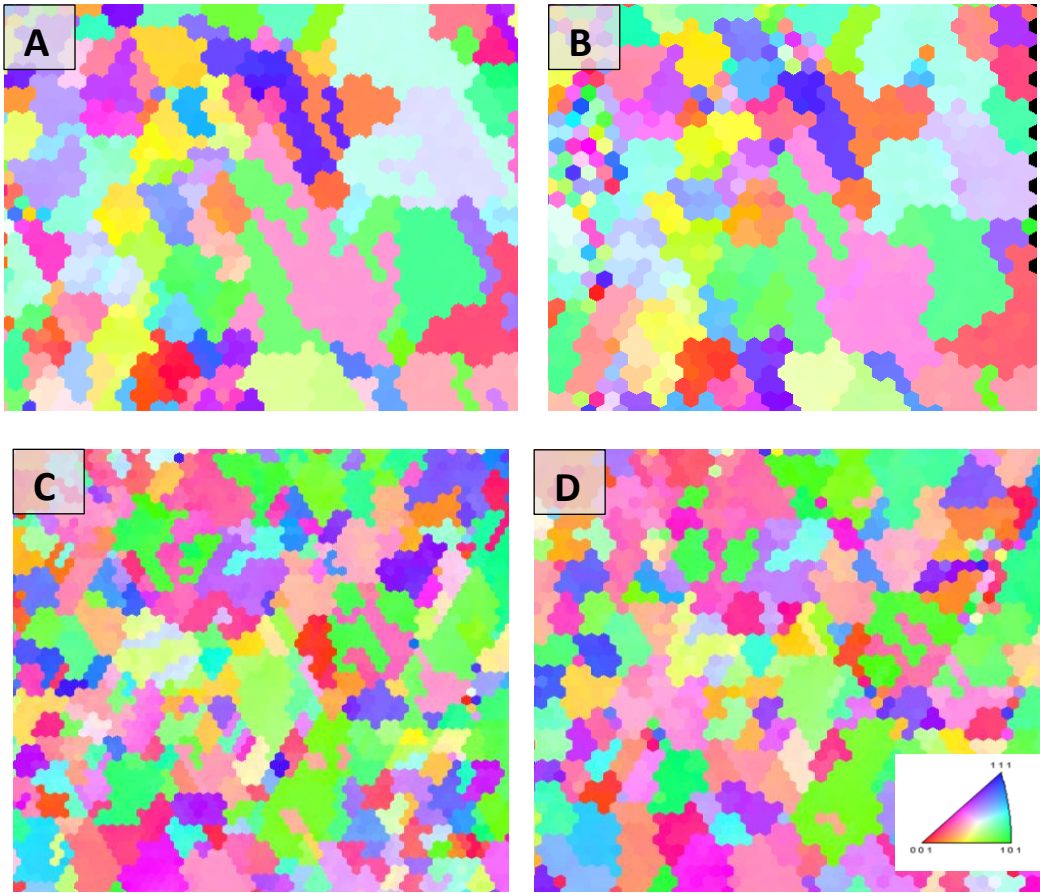
Figure 2.6: EBSD Before (A,C) and After (B,D) Dealloying of $Ag_{0.72}$ $Au_{0.28}$ at 1.17 V vs SHE in 1 M $HClO_4$ With a Pt Counter and MSE Reference

Accordingly, EBSD was attempted before and after dealloying of a silver-gold binary alloy. The setup for dealloying was the same as the setup for the copper-gold seen in Figure 2.5. The dealloying parameters and conditions, however, were taken from Badwe's recipe (N. Badwe et al. 2018; Nilesh Badwe, Chen, and Sieradzki 2017) for crack-free NPG. These results are seen in Figure 2.6. Some grains are preserved very well, but there are some changes in grain shape and orientation. These changes are probably more substantial compared to the copper-gold results in Figure 2.5 because the dealloying was not done at a constant rate, instead the potential was held fixed. The initial dealloying rate for the silver-gold system was higher and the surface, which is

being examined by the EBSD, is the first to dealloy. Dealloying in the bulk will occur more slowly. This indicates that the rate of dealloying may play a large role in whether or not the grain orientation is retained during dealloying. The $L1_2$ phase is closely related to the FCC phase, potentially too close to see effects from the phase change. In the $L1_2$ phase, however, one would expect that vacancies left behind by removed copper atoms would be too small for a gold atom to easily occupy without incurring stresses which may be large enough to cause new grain orientations to become preferable. This makes the retention of grain shape and orientation in the dealloying of $L1_2$ copper-gold surprising.

2.4.2 Morphology

Aquami (Stuckner et al. 2017) was used to evaluate four disordered and four ordered samples. For each sample, five SEM images were chosen to represent the sample. Effort was made to take images from approximately the middle of the sample thickness (100 µm) spaced over the length (5 mm) of the cross-section, avoiding the edges of the sample. Figure 2.7 A and B are representative SEM images of ordered and disordered samples, respectively. Cumulative histograms for ligament length and diameter of all the ordered and disordered samples are seen in Figure 2.7 C, D, E, and F. Notably, both the ordered and disordered ligament diameter histograms (Fig. 2.7 C and E) appear to have a normal bell curve shape while the corresponding ligament length histograms (Fig. 2.7 D and F) are asymmetric and both skewed towards the shorter lengths. The average ligament diameter for each sample is shown in Table 2.2.

|  | Ordered | Disordered |
|---|---|---|
| **Sample 1** | 126.31 | 113.80 |
| **Sample 2** | 128.12 | 131.93 |
| **Sample 3** | 140.41 | 128.00 |
| **Sample 4** | 138.67 | 133.07 |

Table 2.2: Average Ligament Diameters (nm) for Each Ordered and Disordered Sample. (Tse, Karasz, and Sieradzki 2020)
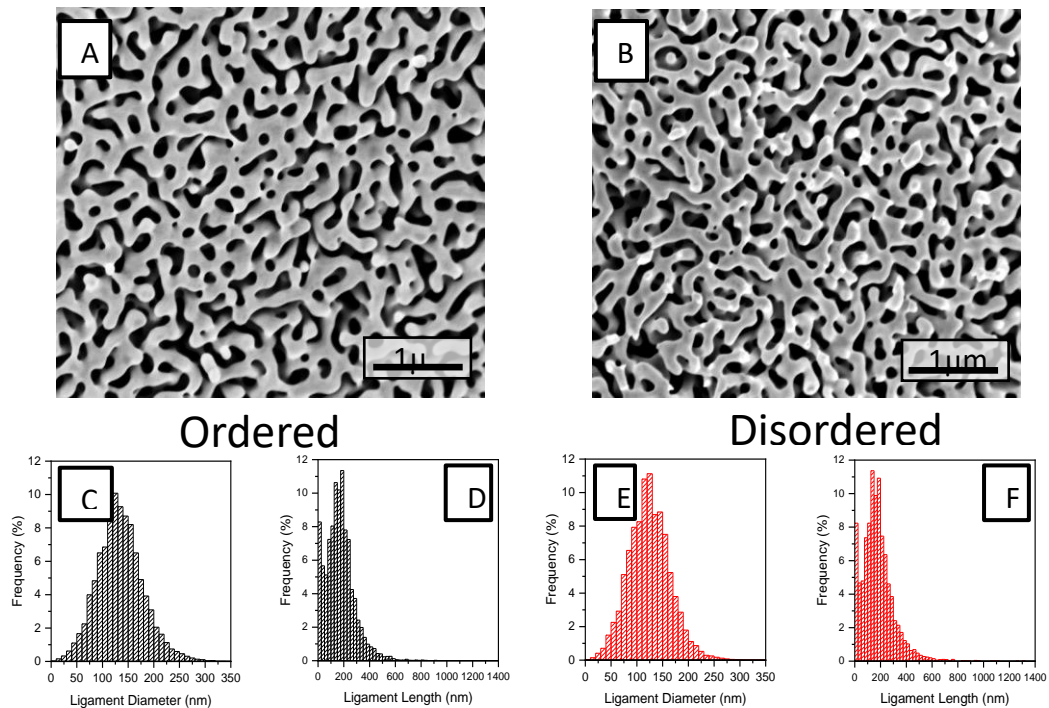


Figure 2.7: SEM Images and Statistical Analysis of NPG Morphology of the Ordered and Disordered Phases. Representative SEM Images of the NPG Morphology Resulting From Dealloying at 1 mA/cm$^2$ an Ordered Sample (a) and a Disordered Sample (B). Cumulative Histograms of the Ligament Size (C) and Ligament Length (D) Obtained From DIA of 5 Images on 4 Different Ordered Samples. Cumulative Histograms of the Ligament Size (E) and Ligament Length (F) Obtained From DIA of 5 Images on 4 Different Disordered Samples. (Tse, Karasz, and Sieradzki 2020)

Overlaying the ligament diameter histograms for the ordered and disordered samples in Figure 2.8 A, it can be seen that the average ligament diameter of the ordered samples is slightly larger than that of the disordered. Comparing box and whisker plots
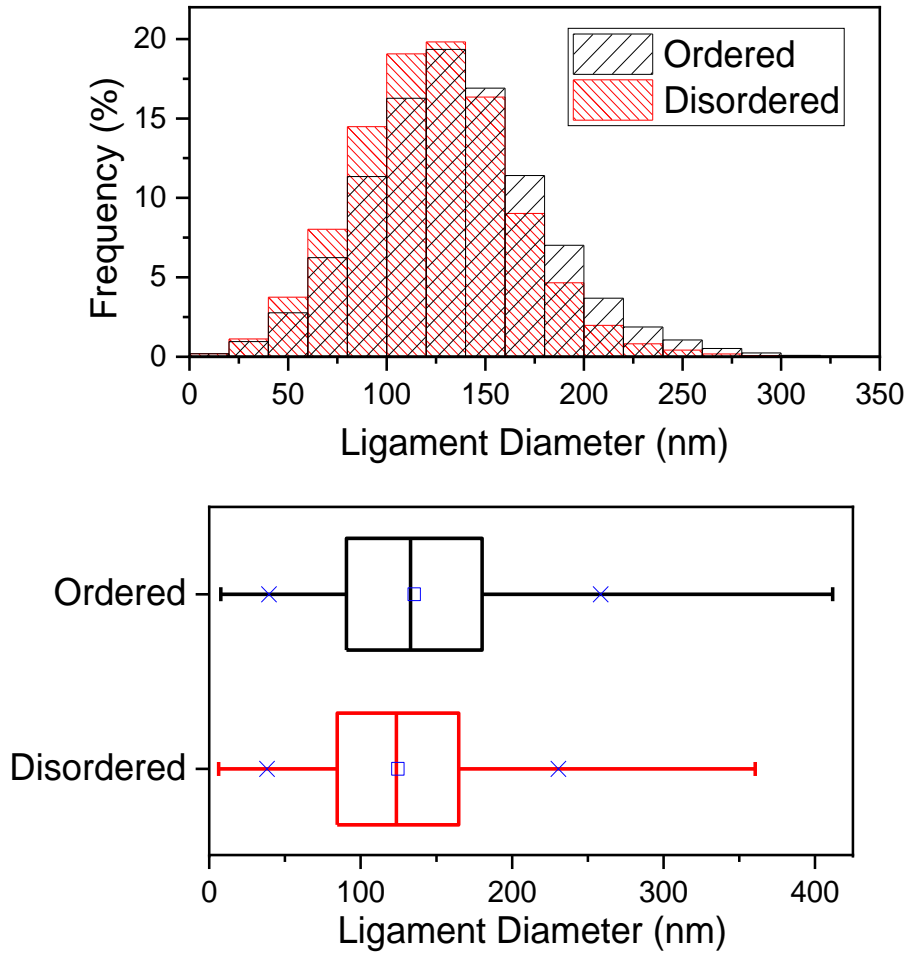
Figure 2.8: (A) Superimposed Ordered and Disordered Ligament Diameter Histograms and (B) Box and Whisker Plots of the Same Data, Where the Left and Right Sides of the Box Are One Standard Deviation From the Mean, Which Is the Vertical Line in the Box. The Blue Square Marker in the Box Is the Median, the Ends of the Lines Are at the Minimum and Maximum, and 99% of the Data Lies Between the Blue X's. Parent Phase Ordered Alloy (Black), Parent Phase Disordered Alloy (Red). (Tse, Karasz, and Sieradzki 2020)

of the same ligament diameter data, Figure 2.8 B, the median ligament diameter value is

very close to the mean for both the ordered and disordered samples and the difference

between the ordered and disordered is small.  The box size corresponds to the standard

deviation, 33% of the mean for the ordered and 32 % of the mean for the disordered.

This is consistent with the findings of 35% by Badwe et al. (Nilesh Badwe, Chen, and

60

Sieradzki 2017). In order to assess any statistical significance to the differences between the ordered and disordered ligament diameters, a statistical T-test was conducted. Using a confidence value of 95% and pooled variance estimate for variations in standard deviation, the test concluded that the differences were not statistically significant. This was anticipated given that the means were so close together and the difference was far less than the standard deviation as evidenced by the box and whisker plot. A difference in ligament diameters had been expected, particularly given the difference in surface diffusion that was so evident in the linear sweep voltammetry. Evidently the morphology is robust against some small differences in surface diffusion.

2.5 Conclusions

A method for achieving EBSD on as-dealloyed noble metal alloys was found. The success of the method is dependent on the careful handling of the material as well as a potential dependence on dealloying rate. EBSD was used to determine that dealloying did not substantially change grain shape or orientation in either or ordered or disordered $Cu_{0.75}Au_{0.25}$ dealloyed at a slow, constant rate. Despite the differences in crystal structure, and thus surface diffusion, there were no observable differences in orientation and shape retention. The phase change from $L1_2$ to FCC in the disordered phase did not impede the retention, potentially due to both being cubic. The ordered and disordered phases of $Cu_{0.75}Au_{0.25}$ were confirmed through both electrochemical methods and XRD. When $Ag_{0.72}Au_{0.28}$ was examined before and after being galvanostatically dealloyed, the grain structure was not as well preserved, potentially owing to the comparatively

increased initial dealloying rate despite being slow enough to produce crack-free NPG. The orientations did however stay fairly close to the original.

Based on digital image correlation, the ordered and disordered phases did not produce substantially different morphologies when dealloyed. The only quantitative difference, the mean ligament diameter, proved not to be statistically significant enough to draw any conclusions. The standard deviation in the ligament diameters were approximately the same and consistent with previous research. Qualitatively, the morphologies appeared the same and equivalent to the traditional NPG morphology achieved from both copper-gold and silver-gold, rounded ligaments, bi-continuous, and isotropic. Hence it can be concluded that the morphology is fairly robust against some differences in surface diffusion and phase. This provides insight into the formation of nanoporous gold ligaments and the role of surface diffusion.

CHAPTER 3

CRACK INJECTION IN SILVER-GOLD ALLOYS

Conventionally, one might expect the strain from loading would be large enough to plastically tear ligaments as they form due to the low yield strength of gold.  As porosity forms in front of the crack, the ligaments would simply stretch until plastic failure.  This would cause the crack to advance in a fairly continuous manner, one ligament at a time, effectively tearing apart the NPG as it formed in front of the crack tip. The crack velocity, in this case, would then be limited by Faraday's law.  Experimental results give velocities much larger than what is possible by the corrosion penetration rate alone, suggesting that this is not what happens.  In slow strain rate ($10^{-6}$ s$^{-1}$) corrosion tests with an applied current density of $10^{-3}$ A/cm$^2$ crack speeds are on the order of 0.1 cm/s (Lichter et al. 1996) but the corrosion penetration rate for that current density is on the order of $10^{-6}$ cm/s.

Instead of the crack advancing with corrosion, some volume, or thickness, of the NPG layer must form in front of the crack before it advances some distance into the uncorroded material.  The layer of porosity then forms on the freshly exposed surface allowing a crack to initiate and penetrate into the uncorroded material again.  Stress-corrosion cracking in polycrystal silver-gold is largely intergranular.  Corrosion occurs faster in a grain boundary than in the grain itself.  This can raise the question, "Is the crack actually penetrating the uncorroded grain boundary, or simply opening an already corroded grain boundary?"  Work by Badwe et al. showed that for a sample undergoing tension via hand-bending a large grain-boundary crack would occur and no evidence of porosity was found on the walls of the crack near the tip (N. Badwe et al. 2018).

63

Section 3.1 uses polycrystal silver-gold samples to provide further evidence that a corroded grain boundary can inject a crack into an uncorroded grain-boundary by statically comparing the depth of grain boundary corrosion to the depth of a crack injection event.  To examine the extent of corrosion down the grain boundary, a sample was corroded, allowed to rest and then pulled to open the corroded grain boundaries.  For comparison, a crack injection experiment was performed where a sample underwent the same corrosion conditions but was subjected to tension immediately following the corrosion.  The depths of the cracks for both samples were then statistically compared. Ultimately these intergranular results show that a "crack-injection" event does penetrate from a corroded, into an uncorroded grain boundary.

Perhaps the earliest evidence that stress-corrosion is a series of finite crack injection events was presented by Newman and Sieradzki in 1985.  It has long been known that there is an acoustic emission associated with fracture (Achenbach and Harris 1979).  There is experimental evidence that for cracks occurring during stress-corrosion cracking, acoustic emissions associated with cracking occur simultaneously with a current transient, when the sample is under voltage control (R. C. Newman and Sieradzki 1983; Sieradzki and Newman 1985).  This brief spike in current results from the exposure of new, parent phase material to the electrolyte.  Newman and Sieradzki used acoustic emissions in tandem with electrochemical current spikes to show that TGSCC can progress in a discontinuous manner in alpha brass (Sieradzki and Newman 1985).  A similar type of experiment looking for current transients associated with crack injection events is presented here, on silver-gold, further supporting the conclusion from the single-crystal experimental results.

3.1 Decoupling Stress and Corrosion

3.1.1 Methods

Silver-gold alloy sheets, 125 µm thick, of $Ag_{70}Au_{30}$ or $Ag_{72}Au_{28}$ were cut into strips approximately 2 mm by 12 mm.  These samples were then lightly mechanically polished with silicon carbide paper (320 American grit) and annealed at 700° C overnight in air.  They were then allowed to cool to room temperature and subsequently suspended in 1 M $HClO_4$ electrolyte.  Using a platinum wire as a counter electrode and a mercury/mercurous sulfate (MSE) reference electrode, the silver-gold sample was dealloyed using a Gamry potentiostat at 1.31 V vs a normal hydrogen electrode (NHE) or 1.26 V vs NHE for 60 seconds for the $Ag_{72}Au_{28}$ and the $Ag_{70}Au_{30}$ compositions respectively.  After being dealloyed, the sample was removed from the acidic electrolyte and placed into a beaker of nanopure water overnight to ensure that electrolyte was completely removed from the sample and corrosion was stopped.  Samples were then dried in air for 24 hours.  After drying, samples were secured on a tensile stage and subjected to ~15% elongation.

A control, crack injection experiment was also performed.  An $Ag_{72}Au_{28}$ sample, 125 µm thick and 1 mm by 12 mm, was dealloyed over a small Teflon cell, attached to a solenoid.  An electrolyte of 0.1 M $HClO_4$+ 0.01 M $AgClO_4$ was used along with a silver wire pseudo-reference and a silver wire counter electrode.  Immediately following a dealloying of 1.26 V vs NHE for 60 seconds, the sample was strained using the solenoid, ~5% elongation.  Then it was immersed in nanopure water, dried, and pulled on the

tensile stage, ~15% elongation. For simplicity the two types of samples will be referred to as corrosion penetration samples and control samples respectively.

After the cracks were opened on the tensile stage, the samples were put in stainless steel sample holding clips, mounted in epoxy, and allowed to cure for 24 hours before being mechanically polished. Initial polishing was done with silicon carbide paper (180, 320, 600, and 1200 American grit) on automated polishing equipment with a pressure of approximately 25 psi. This was followed by hand polishing using alumina suspensions (1.0, 0.3, and 0.05 micron) on soft cloth. Between grits, the samples were thoroughly rinsed using DI water. During polishing, several microns of material were removed to ensure representative cross-sections were exposed. The polished samples were then fixed onto aluminum sample mounts for microscopy. Early samples were not mounted in conductive epoxy while later samples were mounted in conductive epoxy. The non-conductive epoxy samples were coated in carbon to minimize charging. Scanning electron microscopy (SEM) was performed in a Nova 200 NanoLab (FEI) system and a Zeiss Auriga system. SEM micrographs were taken over the length, approximately 8 mm, of the dealloyed portion of the samples. ImageJ was used to analyze the micrographs, like the one seen in Figure 3.1, and measure the depths of the cracks. The depth was taken as the distance from the crack tip to the sample edge, perpendicular to the sample edge.
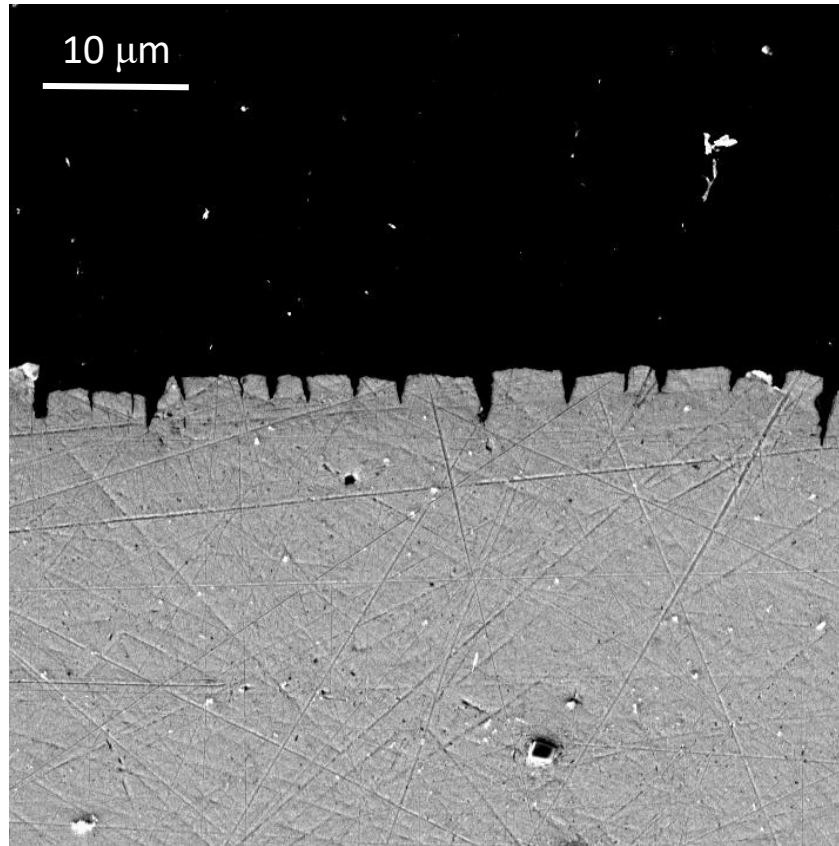
Figure 3.1: SEM Micrograph of $Ag_{72}$ $Au_{28}$ Crack Injection Sample. The Silver-Gold Alloy Is the Bottom of the Image and the Black, Upper Portion Is the Carbon Coated Epoxy. Cracks Can Be Seen Protruding Into the Sample From the Top

3.1.2 Results and Discussion

The statistical distribution of crack depths, which were reported in the paper by

Badwe et al.(N. Badwe et al. 2018), are shown in Figure 3.2. Figure 3.2 A and B are

$Ag_{70}Au_{30}$ and $Ag_{72}Au_{28}$ respectively, corrosion penetration samples and Figure 3.2 C is an

$Ag_{72}Au_{28}$ control sample. Each sample had a different thickness of NPG. The samples

from Figure 3.2 A, B, and C had thicknesses of ~0.6 µm, ~2.2 µm, and ~2.5 µm

respectively. For the corrosion penetration samples, the majority of the cracks stop at or

67

before the interface between the dealloyed layer and the bulk, parent-phase material. Some cracks do extend beyond the average dealloyed layer depth, but this is to be expected. We expect that these deeper cracks are in areas where the dealloyed depth is slightly deeper than average, for example grain boundaries. There is no indication that the cracks are injecting into the bulk, parent-phase material in the corrosion penetration experiments.
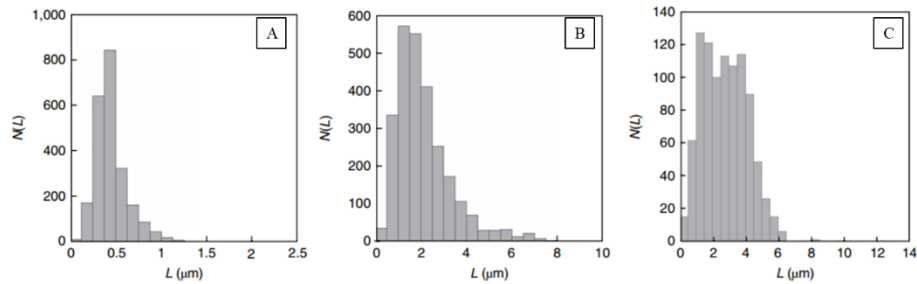


Figure 3.2: Histograms of the Cracks in (A) $Ag_{70}Au_{30}$ Corrosion Penetration Sample, (B) $Ag_{72} Au_{28}$ Corrosion Penetration Sample, (C) $Ag_{72} Au_{28}$ Control Crack Injection. L Is the Length of the Crack Injection/Penetration and N(L) Is the Number of Crack Injections /Penetrations of Length L. (N. Badwe et al.. 2018)

There are clear qualitative differences between the control crack-injection and the crack penetration crack distributions in Figure 3.2. This is expected because the purpose of the control experiment was to inject a crack beyond the NPG/parent-phase interface. Additionally, it is worth looking at the median of the crack penetration depths, seen in Table 3.1. The median crack depth lines up closely with the dealloyed depth in the crack penetration experiments. However, the control experiment shows a median crack depth slightly deeper than the average dealloyed depth.

There are clear qualitative differences between the control crack-injection and the crack penetration crack distributions in Figure 3.2. This is expected because the purpose of the control experiment was to inject a crack beyond the NPG/parent-phase interface.

68

Additionally, it is worth looking at the median of the crack penetration depths, seen in Table 3.1. The median crack depth lines up closely with the dealloyed depth in the crack penetration experiments. However, the control experiment shows a median crack depth slightly deeper than the average dealloyed depth.

| | Mean Dealloyed Depth (µm) | Median Crack Depth (µm) |
|---|---|---|
| Corrosion Penetration $Ag_{70}Au_{30}$ | ~0.6 | 0.55 |
| Corrosion Penetration $Ag_{72}Au_{28}$ | ~2.2 | 1.93 |
| Crack Injection $Ag_{72}Au_{28}$ | ~2.5 | 2.79 |

Table 3.1: Average Dealloyed Depths and Median Crack Depths in Microns for $Ag_{70}Au_{30}$ and $Ag_{72}Au_{28}$ Samples Where the Tension Was Applied to Open Corroded Grain Boundaries as Well as the Control, Crack-injection $Ag_{72}Au_{28}$ Sample Where the Corrosion and Tension Were Applied in Quick Succession (N. Badwe et al. 2018)

3.2 Current Transients

3.2.1 Methods

A polycrystal sheet of $Ag_{72}Au_{28}$ was cut into samples between 1 and 3 mm wide and 10 mm long. Single crystal samples were wire EDM cut from a single crystal of $Ag_{77}Au_{23}$, 9 mm in diameter, whose z-axis was in the (001) direction by Majer Precision Engineering with a thickness of 100 µm and a width of 1 mm. Samples were lightly polished using a silicon carbide paper before being annealed in air at 700° C for 16 hours. The samples were secured on one end to a tensile stage and the other to a load cell, spanning a small Teflon well, 1 mm wide, that held the electrolyte. Corrosion took place in 0.1 M $HClO_4$ + 0.01 M $AgClO_4$ with a silver counter electrode and silver wire pseudo

reference electrode on a Gamry 1010B potentiostat.  The sample was extended a

determined distance and allowed to relax for ~2 minutes before beginning corrosion.  A

constant voltage was applied to induce corrosion: 1.23 V vs NHE for the poly crystal and

1.15 V vs NHE for the single crystal.  The experimental setup can be seen in Figure 3.3.
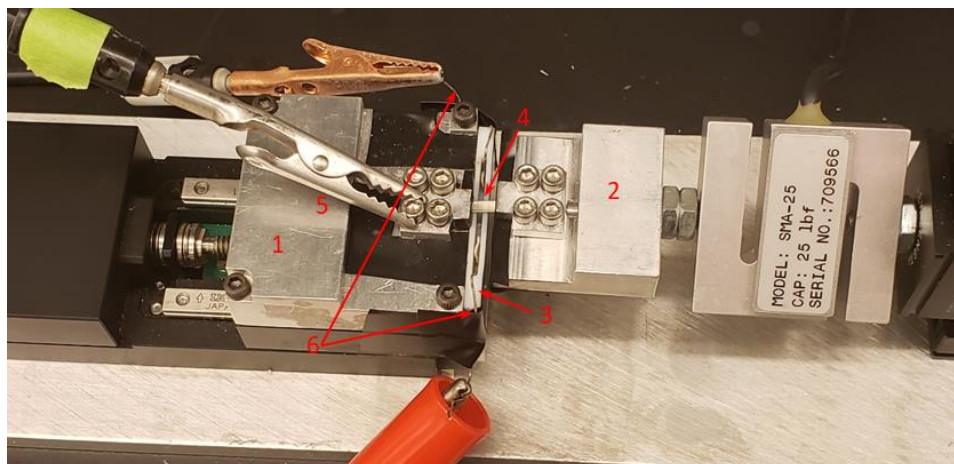


Figure 3.3: Experimental Setup for Current Transient Experiments: Tensile
Stage (1), Load Cell (2), Teflon Cell (3), Sample (4) and Working Electrode
Clip Connected to the Sample (5) As Configured for a Test. The Teflon Cell
Containing the Counter and Reference Electrodes (6) Is Filled With
Electrolyte. The Bottom Surface of the Sample Is in Contact With the
Electrolyte Meniscus so That Only This Face of the Sample Is Dealloyed.

The first ten seconds of corrosion were not recorded by the potentiostat for the

polycrystal samples in order to increase its data collection precision.  Load and current

data was recorded through the rest of the experiment at a rate at or faster than 50 points

per second.  When the fracture had come to completion, the voltage was turned off and

the sample removed and rinsed in nanopure water.  The fracture surfaces were examined

using the scanning electron microscope on a Zeiss-Auriga FIB SEM.

3.2.2 Results and Discussion

Fracture surfaces for samples at six different initial stresses can be seen in Figure 3.4. The fracture surfaces are predominantly intergranular. Figure 3.5 shows higher magnification images for the fracture surfaces of Figure 3.4 D and E. Notably the fracture surface in Figure 3.4 F is the only fracture surface exhibiting any ductile fracture but it also exhibits large areas of transgranular fracture. These fracture surfaces are consistent with what is expected from silver-gold in stress-corrosion cracking. Silver-gold tends to preferentially fracture intergranularly during stress corrosion cracking but can undergo transgranular fracture as well.
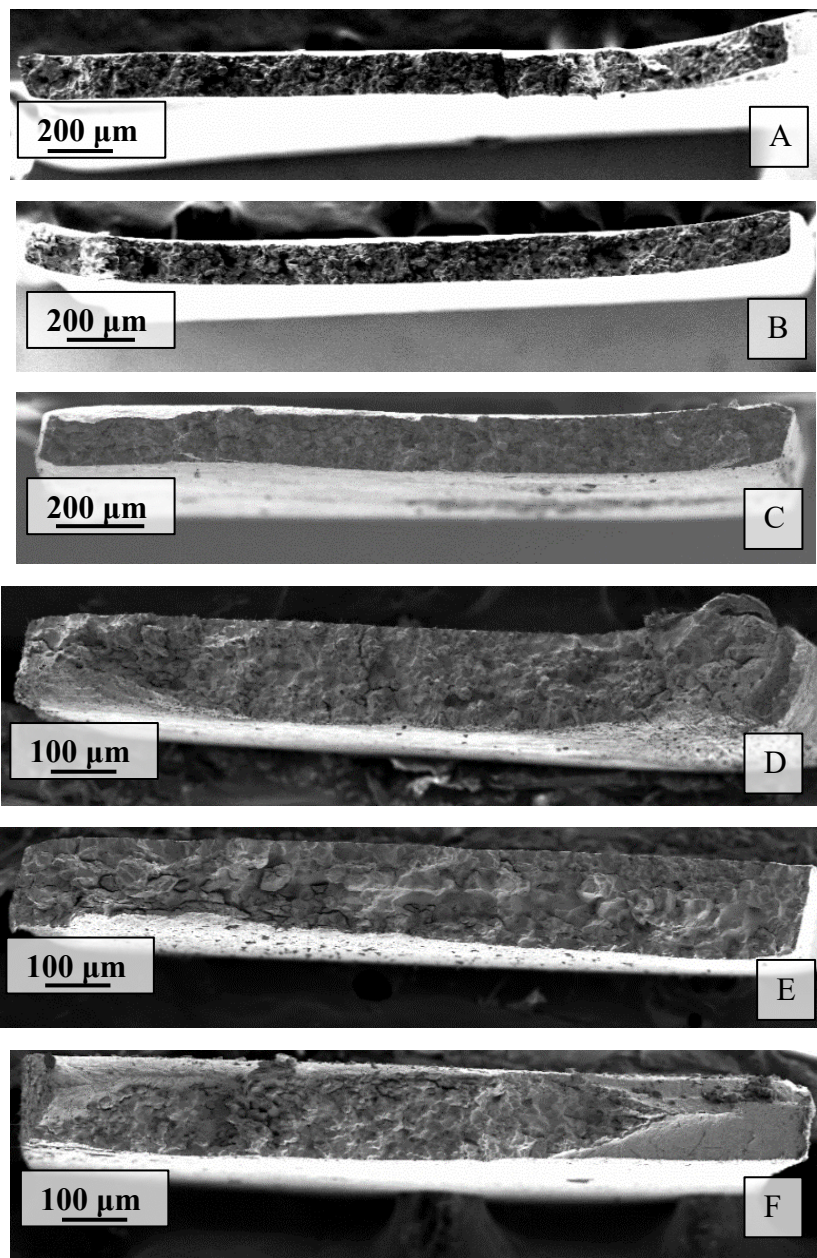
Figure 3.4: Fracture Surfaces of Ag$_{72}$ Au$_{28}$ Polycrystal Samples With Initial Stresses of (a) 84 MPa, (B) 100 MPa, (C) 101 MPa, (D) 117 MPa, (E) 121 MPa, and (F) 132 MPa. Samples Were Dealloyed at 1.23 V vs NHE While Under Tension
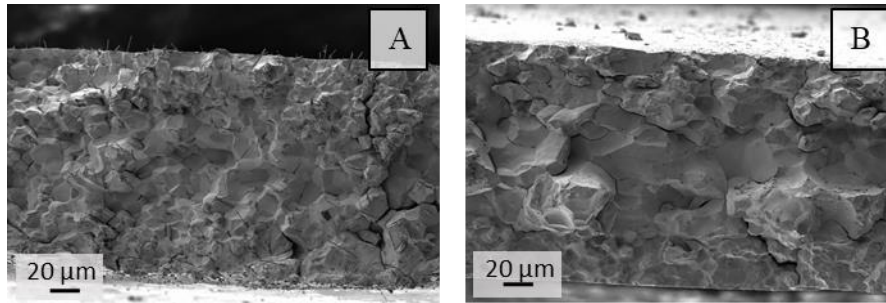
Figure 3.5: Fracture Surfaces for Polycrystal $Ag_{72}$ $Au_{28}$ Samples That Underwent Corrosion With an Initial Stress Level of (a) 117 MPa and (B) 121 MPa

The load cell proved not to be sensitive enough to capture the small changes from the crack injection events for the polycrystal samples. Current transients were visible however in the electrochemical data. In Figure 3.6, a sample of the current transients is seen in the electrochemical data for the sample with an initial stress of 37.9 MPa. For these current transients you can clearly see the peak and decay behavior that is expected. Not all current transients show this clearly due to various reasons. Cracks can be occurring in multiple places at once or close enough together in time to obscure the decay behavior.
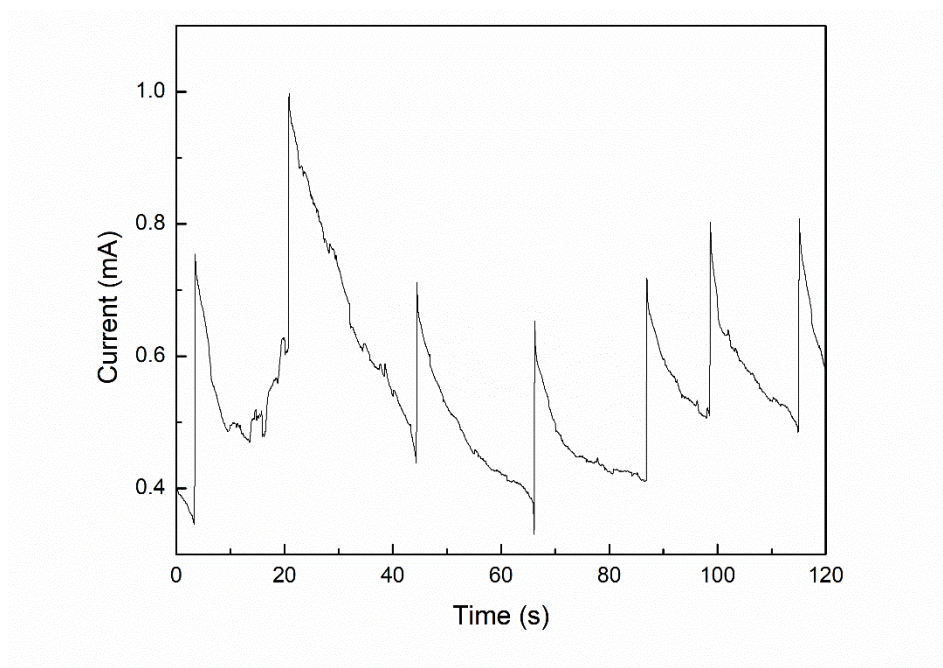
Figure 3.6: Electrochemical Current Data From a $Ag_{72}$ $Au_{28}$ Polycrystal Sample Dealloyed at 1.23 V vs NHE While Under an Initial 37.9 MPa Tension Showing Current Transients.

The electrochemical data files were loaded into the software program, Origin. The current data was put through Origin's peak analyzer. Filtering parameters were optimized for each sample in order to ignore noise and variations in current caused by cracks forming in the nanoporous gold layer.
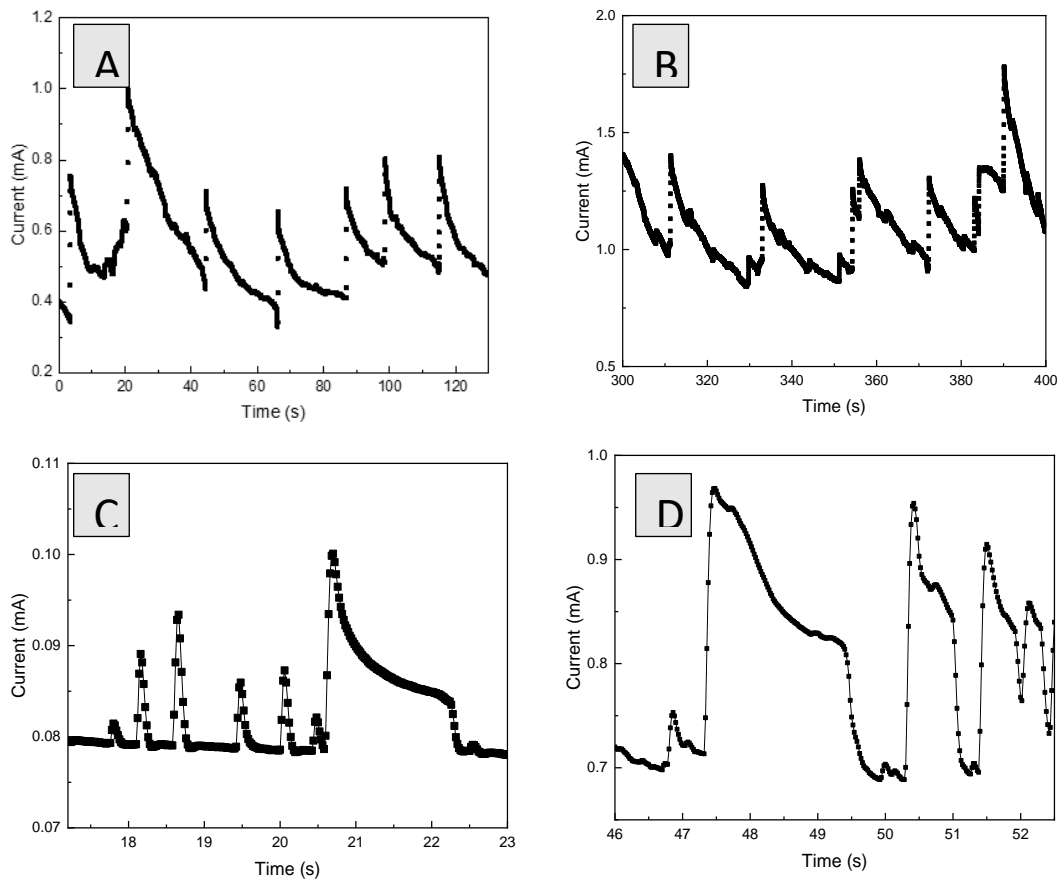
Figure 3.7: Current Transient Data for Samples with Initial Stresses
of (A) 38 MPa, (B) 48 MPa, (C) 117 MPa, and (D) 121 MPa

Representative current transients at four initial strain values are shown in Figure

3.7.  Histograms of the time between current transients is seen in Figure 3.8.

Experiments at lower initial stresses are difficult to conduct due to the length of time the

process takes and the size of the electrolyte well.  Due to the small amount of electrolyte

that can be held, the amount of silver that builds up in the electrolyte and on the counter

electrode over long periods, over 1000 seconds, begins to interfere with the experiment.

75
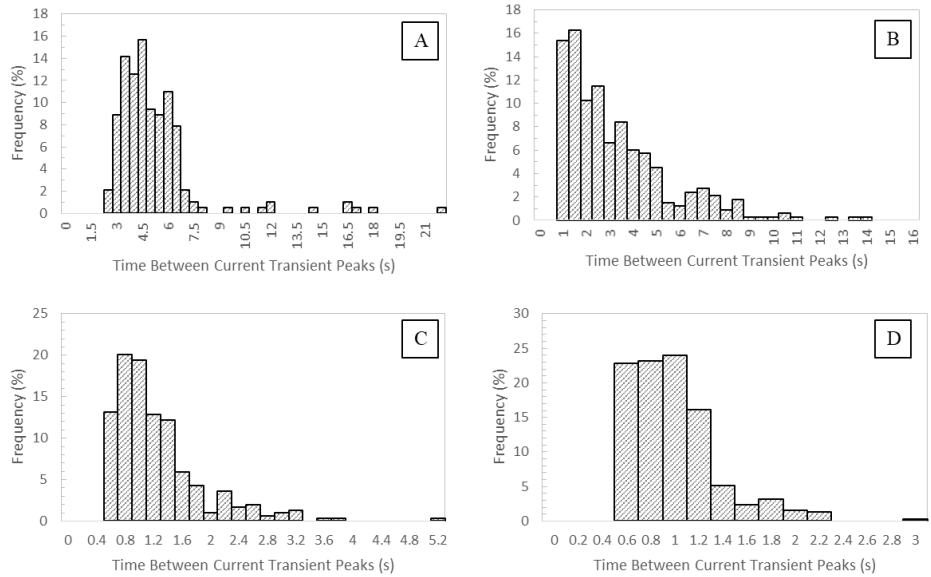
Figure 3.8: Histograms of the Average Time Between Current Transient Peaks for Initial Stress Levels of (A)38 MPa (B)48 MPa (C) 117 MPa (D) 121 MPa

| Initial Stress (MPa) | Mean | Median | Standard Deviation |
|---|---|---|---|
| 38 | 5.02 | 4.36 | 2.73 |
| 48 | 3.04 | 2.37 | 2.34 |
| 117 | 1.16 | 0.98 | 0.65 |
| 121 | 0.89 | 0.83 | 0.37 |

Table 3.2: Average Dealloyed Depths and Median Crack Depths in Microns for $Ag_{70}Au_{30}$ and $Ag_{72}Au_{28}$ Samples Where the Tension Was Applied to Open Corroded Grain Boundaries As Well As the Control, Crack-injection $Ag_{72}Au_{28}$ Sample Where the Corrosion and Tension Were Applied in Quick Succession. (N. Badwe et al.. 2018)

Evaporation of the electrolyte will occur and necessitates adding more electrolyte during the experiment which causes a jump in current. For this reason, the samples at the two lower stress values were run under the same corrosion conditions, but only allowed

to proceed for a thousand seconds.  These samples are represented by the green dots in

Figure 3.9.
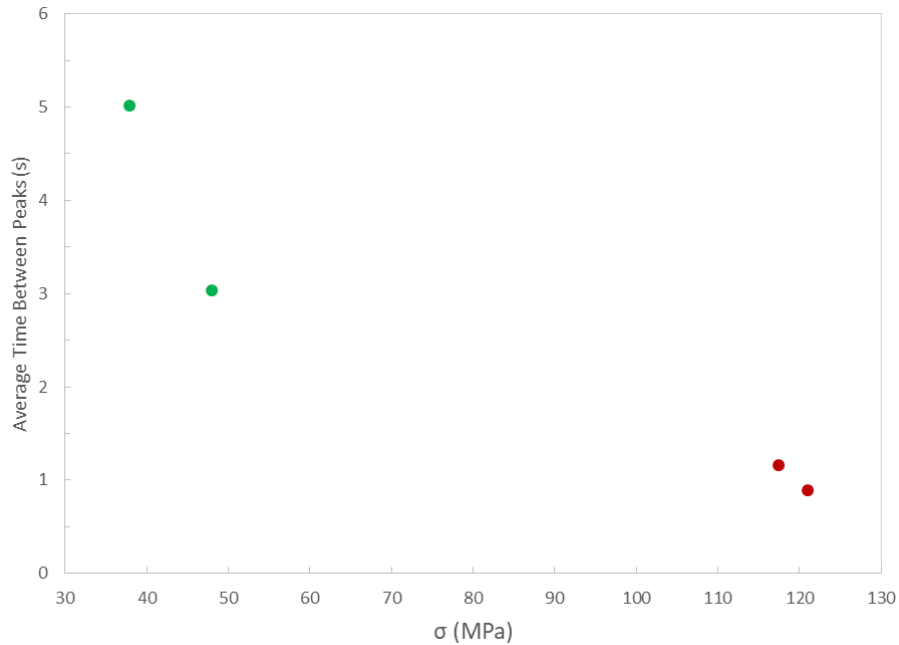


Figure 3.9: Average Time Between Current Transient Peaks Versus Initial
Applied Stress Including Lower Initial Stress Samples That Do Not Proceed to
Fracture (Green) and Samples That Did Experience Through Thickness
Fracture (Red)

    While many other experiments were conducted at a variety of initial stress values,

only the ones showing exponential-like decay in the current transients are included here.

At higher stress values, the current transients appear to be occurring too closely together

to be distinguishable at a sampling rate of 0.05 s and the peaks overlap such that the

characteristic exponential decay is obscured.  Furthermore, the magnitude of the current

transient peaks appears to decrease with increasing stress, an expected result.  However

for these smaller current transients, they become much more difficult to distinguish from

background noise.
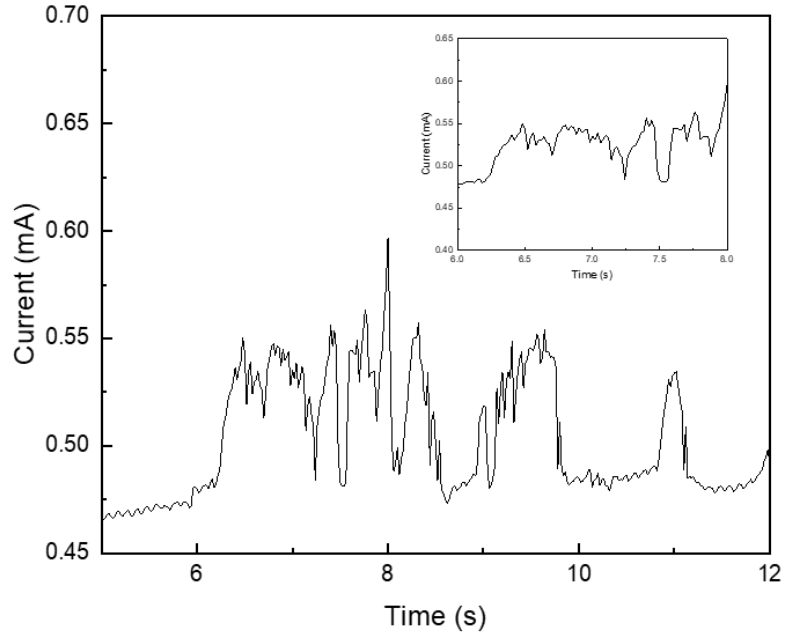
Figure 3.10: Single Crystal Current Data for an Initial Stress of 18 MPa. Example of Noise Obscuring Potential Crack Injections. Inset Graph Is Increased Magnification of a Set of Peaks As an Example of Peaks With No Steep Initial Rise and Exponential Current Decay Behavior.
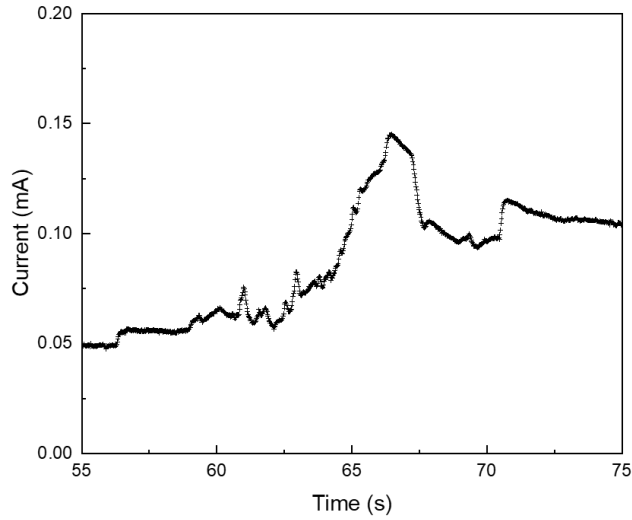


Figure 3.11: Single Crystal Current Data for an Initial Stress of 21 MPa Showing an Example of Possible Current Transient Overlapping

78

Occasionally, the data appeared to have intermittent sinusoidal events occurring on the order of the current transient magnitude. These events obscure current transient peaks, making it difficult to reliably find the distance between them, therefore that data is not considered here. Attempts were made to move to a different experimental set-up where more electrolyte could be employed and a Faraday cage could be used. These attempts were unsuccessful. Applying a steady-current rather than an applied voltage was attempted to see if the voltage peaks were more easily distinguishable, this approach was not fruitful. Corrosion applied during a constant strain also produced noisier data, presumably due to electrical noise from the tensile stage.

These experiments were attempted on single crystal samples with the hope that the crack injection events would be large enough to avoid the issues mentioned. At low stress values, the current transients either were not present or obscured. For higher stress values, the samples fractured in a single observable injection event or too quickly to distinguish separate crack injection events at a sampling rate of 0.05 s. Some examples of such issues with single crystal experiments can be seen in Figures 3.10 and 3.11.

A relationship between the initial stress and the time between crack injection events can be seen. As the initial stress increases, the time between crack injection events decreases. Due to the limited nature of the data set, no definitive comments can be made on the shape this relationship may take.

Not much is known about the initiation of a crack in nanoporous gold during stress corrosion cracking. Chen showed that higher initial stresses in nanoporous gold lead to a higher terminal velocity (X. Chen 2016; X. Chen et al. 2020). Therefore it stands to reason that a crack in a sample with a higher initial stress does not require as

79

thick of a nanoporous gold layer in order to achieve the speed required to inject into the parent phase material compared to a sample with lower initial stress. This is consistent with lower initial stress samples having more time between the crack injection events evidenced by the current transients.

3.3 Conclusions

Histograms of crack depths in crack penetration and crack injection polycrystal experiments showed clear qualitative differences in shape. Quantitatively, the cracks for the crack-injection experiment went much deeper, ~ 4 μm deeper, than the cracks in the corrosion penetration sample. Additionally, for the corrosion penetration samples, the median crack depth is slightly less than the average corrosion depth but for the crack injection sample the median crack depth goes beyond the average corrosion depth. These results support previous research from our group which claims to have injected a brittle crack into the parent-phase alloy (N. Badwe et al. 2018; Nilesh Badwe 2014). A similar composition and dealloying protocol were employed, but these crack penetration experiments produced substantially shallower cracks compared to the injected cracks. This indicates that in the work by Badwe the cracks were injected and not simply traveling down an already dealloyed grain boundary (Nilesh Badwe 2014). These confirmed injected cracks help to create a basis for the argument that stress-corrosion crack in silver-gold alloys is composed of a set of crack injection events.

To look for evidence of discontinuous crack injection events during stress-corrosion cracking, the current was monitored during stress corrosion cracking. Current transient events were observed, corresponding to the exposure of fresh surface to the

80

electrolyte.  The observance of these current transients supports the theory that stress

corrosion cracking can occur discontinuously.  When the imposed stress at the beginning

of corrosion is higher, the current transients occur closer together in time.  Conversely for

lower imposed stress the current transients occur more infrequently.  The more time that

has passed, the thicker the layer of nanoporous gold implying that higher stress samples

do not require as thick of a layer to inject into the parent phase.  This is consistent with

observations by Chen that cracks in higher initial stress nanoporous gold samples gain

speed more quickly in the early stages of crack propagation (X. Chen 2016; X. Chen et

al. 2020).  The current capabilities of the experimental setup are limiting.  A more

sophisticated setup should be employed to confirm these results and build a more

complete data set.

        These results support the film-induced cleavage model for stress-corrosion

cracking and opens more avenues for research. In particular, further research into the

relationship between the initial stress and the thickness of the nanoporous gold layer as it

relates to the frequency and depth of crack injections may provide insight into the

initiation of a crack in nanoporous gold.

CHAPTER 4

CRACK INJECTIONS COMPARED TO STRESS-CORROSION

The propensity of silver-gold to fracture intergranularly during stress-corrosion cracking can be limiting when looking to compare fracture surfaces. One can use single-crystal silver-gold samples to examine transgranular stress corrosion cracking. The work presented in this chapter uses single-crystal silver-gold samples to compare fracture surfaces from crack-injection, where the tension is applied immediately following the corrosion, and stress-corrosion, where the tension is applied simultaneously. Comparing the crystallographic directions of the fracture surfaces with electron backscatter diffraction, the transgranular fracture surfaces provide evidence that stress-corrosion cracking is a series of finite crack injection events.

4.1 Methods

A round single crystal with a 9 mm diameter and a composition of 77 at% Ag 23 at% Au was taken to Majer Precision Engineering Inc. to have samples cut by wire electrical discharge machining. Disks 100 µm thick were cut from the crystal. Strips 1 mm wide were then cut from the disk. Tensile directions were chosen randomly to avoid bias. The single crystal was then taken to CAMET Research Inc. to be oriented. The axis of the crystal was found to be 11.8° from (110) and the tensile directions of the samples were $(10\bar{4})$ and $(8\bar{5}\bar{6})$. These directions are within 14° of [001] and $[\bar{1}11]$ respectively. These strips were then lightly polished using silicon carbide paper before being annealed at 500° C for 24 hours in air and furnace cooled.

For crack-injection experiments, the samples were mounted over a rectangular Teflon cell attached to a solenoid tensile device. Approximately 2 mm of each end of the sample were clamped down to the stage of the tensile device with the sample spanning the Teflon cell. The Teflon cell has a 1 mm wide well for electrolyte which was filled with 0.1 M $HClO_4$ + 0.01 M $AgClO_4$ and silver wires were used as reference and counter electrodes in a three-electrode setup connected to a Gamry potentiostat. The sample was then dealloyed at 1.26 V vs SHE for 30 seconds exactly as determined by the chronoamperometry feature of the potentiostat. This dealloying prescription results in a nanoporous gold layer ~5 µm thick. As soon as the chronoamperometry was visually confirmed to be completed, a manual switch on a Magnetic Sensor Systems pull-type tubular s-22-150-30 solenoid device was triggered, rapidly applying the tension (less than 1 second between completion of corrosion and application of tension). This resulted in a through-thickness fracture. The solenoid applies ~28.9 N with a ~56 ms rise time, which was measured using an Interface SMA-25 mini s-type load cell and an uncorroded 2 mm wide 72 at% Ag 28 at% Au polycrystal sample. After fracture the samples were rinsed in nanopure water and air dried.

For stress-corrosion experiments, the samples were mounted over a rectangular Teflon cell attached to a motorized tensile stage (Thorlabs, Inc. MTS25-Z8 and Thorlabs, Inc. KDC101) and load cell (SMA-25, Interface Inc.). Approximately 2 mm of each end of the sample were clamped down to the stage of the tensile device with the sample spanning the Teflon cell. The Teflon cell has a 1 mm wide well for electrolyte which was filled with 0.1 M $HClO_4$ + 0.01 M $AgClO_4$ and silver wires were used as reference and counter electrodes in a three-electrode setup connected to a Gamry potentiostat. For

fixed displacement, the sample was then rapidly loaded (2.4 mm/s) to a fixed

displacement corresponding to ~1.78 N after relaxation.  The sample was then dealloyed

at 1.15 V vs SHE until the sample experienced complete through-thickness fracture.

Conversely for slow strain rate the samples were dealloyed at 1.15 V vs NHE while being

extended at 1 µm/s, continuing until through-thickness fracture was achieved.  The

samples were then rinsed in nanopure water and air dried.

The fracture surfaces of the crack-injection and stress-corrosion samples were

examined using the scanning electron microscope and electron backscatter diffraction on

a Zeiss-Auriga FIB SEM.

4.2 Results and Discussion

The crack-injection experiments, seen in Figure 4.1, produced very smooth,

brittle fracture surfaces.  The $[10\overline{4}]$ sample did undergo some ductile fracture but

exhibited large section of flat, brittle cleavage-like fracture seen in the SEM micrograph

in Figure 4.1 A.  The $[8\overline{5}\overline{6}]$  sample in Figure 4.1 B showed brittle cleavage-like fracture.

The EBSD corresponding to these fracture surfaces is seen in Figure 4.1 C and 4.1 D.
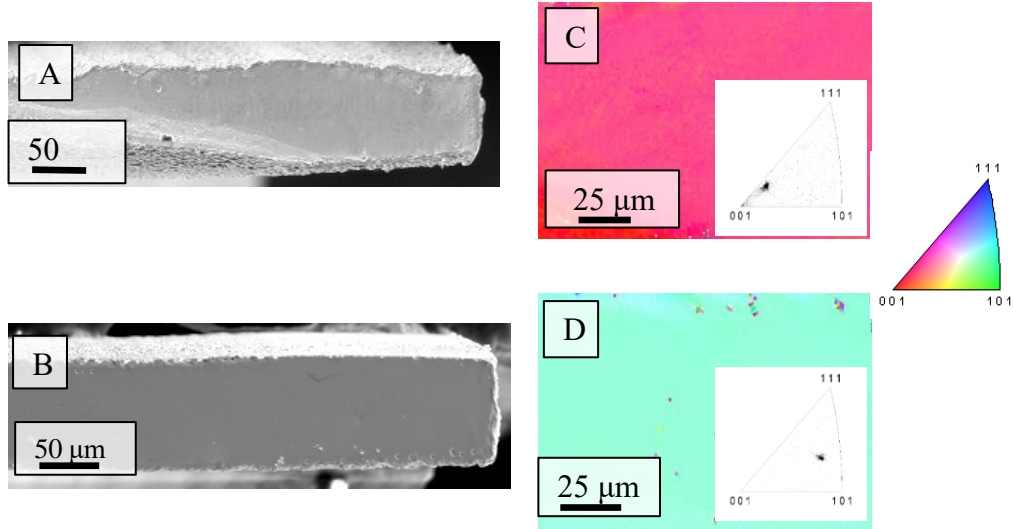
Figure 4.1: Fracture Surfaces for Crack Injection Experiments on 100 μm Thick, $Ag_{77}Au_{23}$ Single Crystal Samples. (A) [$10\bar{4}$] Orientation Underwent Both Brittle and Some Ductile Fracture and (B) [$8\bar{5}\bar{6}$] Orientation Underwent Brittle Fracture and (C) (D) Their Corresponding EBSD. (X. Chen et al.. 2020)

The stress-corrosion experiments are seen in Figure 4.2. Although the fracture surfaces produced flat fracture surfaces, these exhibit noticeable texture. The [$10\bar{4}$] tensile axis sample produced a fracture surface close to the ($1\bar{1}\bar{5}$) pole, 15.8° off of the ($00\bar{1}$) pole. The [$8\bar{5}\bar{6}$] tensile axis sample produced a fracture surface near the ($2\bar{2}\bar{1}$) pole which is 15.8° off of the ($1\bar{1}\bar{1}$) pole.
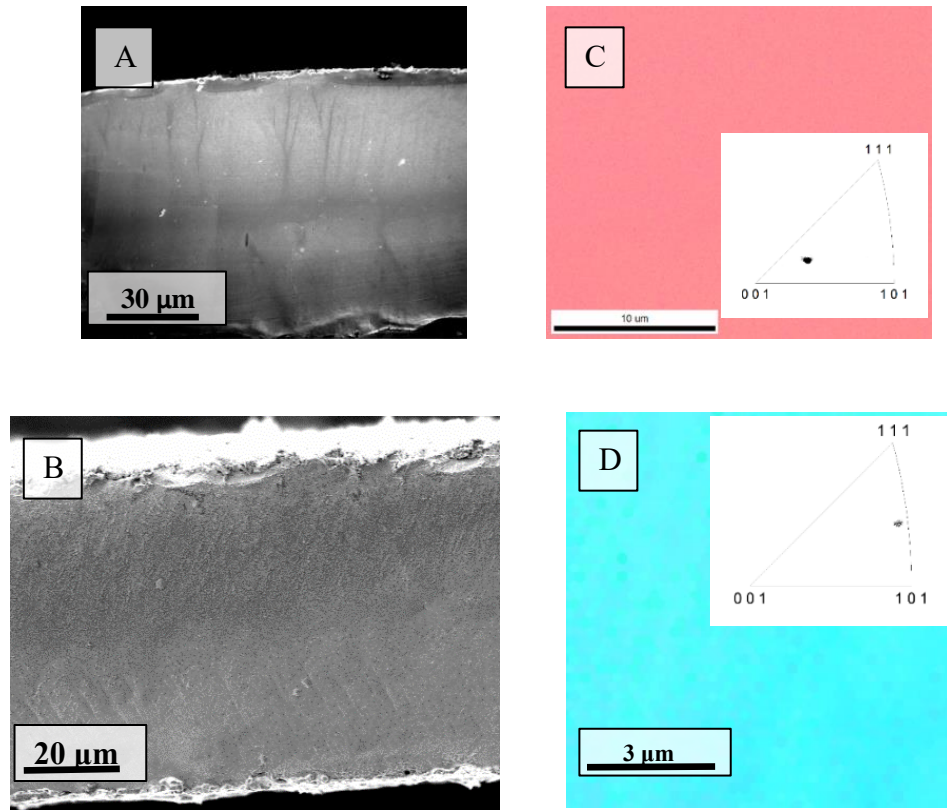
Figure 4.2: Fracture Surfaces for Stress-Corrosion Experiments on 100 μm Thick, $Ag_{77}Au_{23}$ Single Crystal Samples. SEM Micrographs of Fracture Surfaces for (A) $[10\bar{4}]$ Orientation and (B) $[8\bar{5}\bar{6}]$ Orientation and (C) (D) Their Corresponding EBSD. (X. Chen et al. 2020)

It is generally expected that a cleavage-like fracture surface will be a low-index crystallographic surface. The stress-corrosion experiments evidently returned high-index surfaces. An explanation for this is that these high-index surfaces are low-index "vicinal-like" surfaces. This also explains the "texture" in the SEM micrographs of the stress-corrosion experiments. The $[2\bar{2}\bar{1}]$ direction as a vicinal-like surface can be composed of steps with terraces of $(1\bar{1}\bar{1})$ and a width equivalent to the third nearest neighbor (nn) distance on a {111} surface, 0.863 nm. The riser will have an orientation of (111) and be of monatomic height, 0.235 nm. This is written in the notation $3(1\bar{1}\bar{1})$ x 1 (111). This decomposition holds for a terrace width of 3m and a height of m where m is an integer,

creating a more general surface description 3m $(1\bar{1}\bar{1})$ x m (111).  Similarly, the $[1\bar{1}\bar{5}]$

direction as a vicinal-like surface can be written as 3m $(00\bar{1})$ x m $(11\bar{1})$.
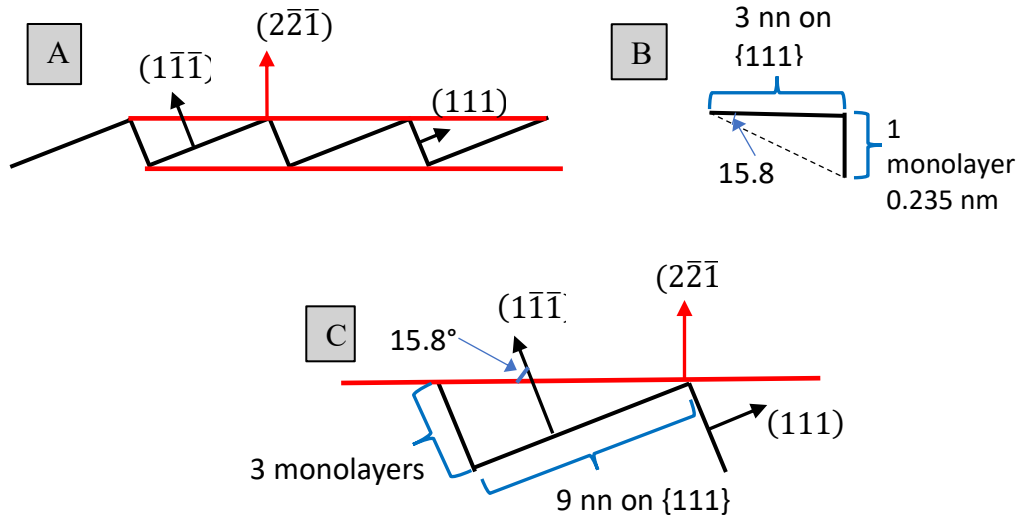


Figure 4.3: Diagrams for a Vicinal-like Surface, Measured by EBSD as $(22\bar{1})$. (A) Shows Steps on the Surface in Black and the Surface Returned by EBSD in Red. (B) Gives the Relevant Widths and Heights for the Smallest Step Size. (C) Shows the Step Dimensions Scaled Up by a Factor of Three.

The crystallographic similarities between the fracture surfaces of the crack-injection and stress-corrosion lead to the conclusion that the stress-corrosion cracking is occurring as a crack injection, taking the same preferred crystallographic planes. Notably, the fracture surfaces are not {111} which is the preferred slip plane in FCC materials.

4.3 Conclusions

To examine this further, single crystal silver-gold samples underwent stress corrosion cracking and a crack-injection event.  The fracture surfaces for both sets of experiments are flat.  The crack injection surfaces are particularly flat and cleavage-like,

87

while the stress corrosion surfaces show some small amount of texture. When the crystallographic planes of fracture are compared, a striking resemblance appears between the sets of experiments. Treating the stress corrosion surfaces as vicinal-like surfaces, their high-index orientations can be decomposed into steps with lower index terraces. Low-index orientations are expected in a cleavage-like fracture. The orientations of these fracture surfaces are particularly significant because for neither case is the fracture surface {111}, which is the close-packed plane in a FCC material.

The crystallographic similarities between the crack injection fracture surfaces and the stress corrosion fracture surfaces lend credence to the theory that stress corrosion cracking is a series of crack injection events rather than a single continuous event. This idea is an extension of the film-induced cleavage mechanism for stress-corrosion cracking. It may also be applicable to other forms of environmentally assisted fracture. Recently a process similar to the crack injection mechanism described here was proposed in relation to hydrogen embrittlement in high strength steels (Shishvan, Csányi, and Deshpande 1952). There it was suggested that under suitable conditions, dynamic effects will inhibit plastic flow such that a high-speed crack nucleated in a hydride can be injected several microns into the parent-phase.

CHAPTER 5

SAMPLE SIZE EFFECTS IN NANOPOROUS GOLD

Badwe et al. showed that for nanoporous gold samples with a thickness of 125 μm and a width of 3 mm, the behavior of nanoporous gold in tension was brittle for a ligament diameter less than ~ 220 nm and ductile for larger ligament diameters (Nilesh Badwe, Chen, and Sieradzki 2017).  This has only been examined for the 125 μm thickness samples, but based on these results an estimate can be made about what ligament diameter for various sample thicknesses will produce ductile versus brittle behavior.  The average ligament diameter is $< \mathscr{L} >$ and the length of a ligament is defined as $m < \mathscr{L} >$ where m is a constant ranging from 3 to 5.  A representative cell volume, $v_{cell}$, is then defined as $(m < \mathscr{L} >)^3$ and the number of ligaments in the cell volume, n, is then estimated.  Using these representative values, the total number of ligaments in the cell, N, can be estimated from the volume of the sample, V, by the equation $nV/v_{cell}$.  Using $< \mathscr{L} >$ and sample size from the previous work in Sieradzki's group, we estimate m=3 and n=5, $N \cong 5 \times 10^{10}$ ligaments and, as an estimate, at ~10x the ligaments we would expect brittle behavior and at ~1/10x we would expect ductile behavior for this sample size.  Using this calculated N value, we can estimate approximately what size tensile sample would be the transition point from brittle to ductile fracture behavior. The ligament size is limited by parent phase alloy composition and dealloying rate requirements to form monolithic crack-free NPG.
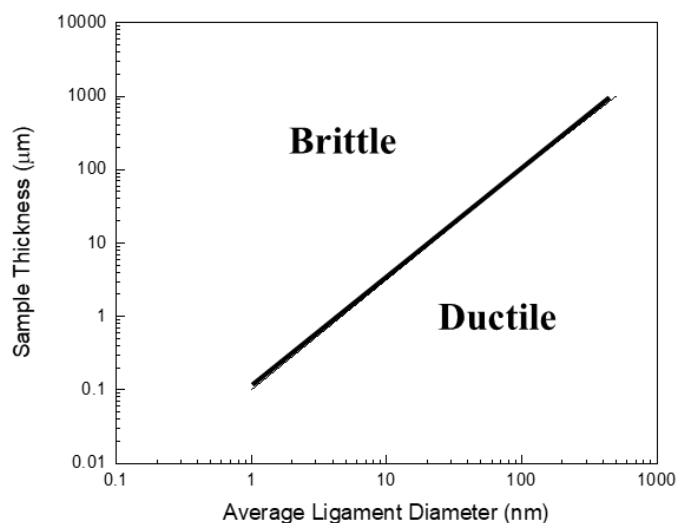
Figure 5.1: Critical Radius of a Tensile Wire Sample, 1 cm Long, vs Mean Ligament Size for Transition From Ductile to Brittle Behavior in Nanoporous Gold

## 5.1 Methods

A sheet of 12 μm thick 70 at% silver 30 at% gold from Goodfellow and a 50 μm thick 72 at% silver 28 at% gold sheet were cut into samples approximately 2.5 mm wide and 10 mm long. The samples were heat treated, in air between quartz plates at 600° C for 36 hours and furnace cooled. Samples were placed on a piece of mica with a layer of gold deposited on it and secured by wrapping with gold wire. This was placed in a glass dish of 1 M $HNO_3$. A platinum wire was put partially into the electrolyte and connected to the counter electrode lead of a Gamry 1010B potentiostat. The gold wire connected to the samples was connected to the working electrode lead and a mercury-mercurous sulfate reference electrode in a salt bridge was put into the electrolyte and connected to the reference electrode lead. These samples were dealloyed at 1.14 V vs NHE for multiple days until the current density dropped below 10 $\mu A/cm^2$. This voltage was chosen based on the linear sweep voltammetry, seen in Figure 5.2 and a series of tests on

90

12 μm thick samples. Voltages above 1.14 V vs NHE resulted in large amounts of grain boundary cracking in the nanoporous gold for the 12 μm thick samples.
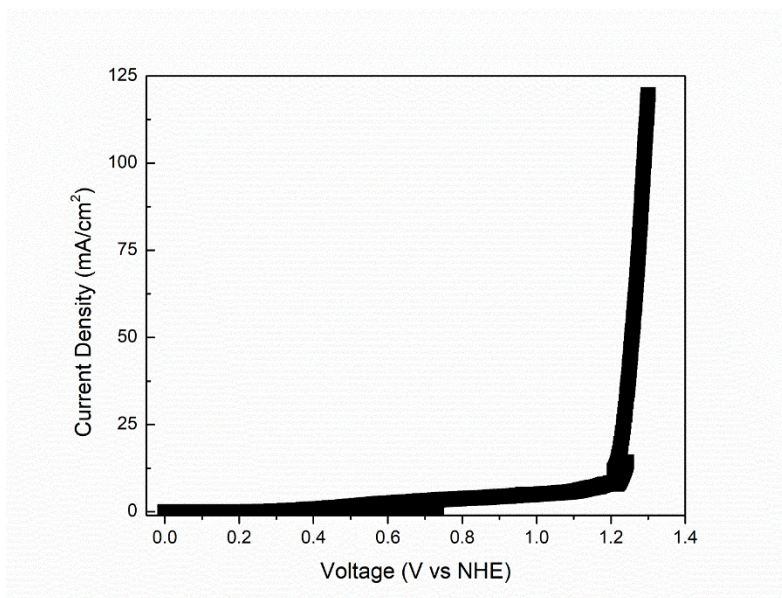


Figure 5.2: Linear Sweep Voltammetry for a 12 µm Piece of $Ag_{70}Au_{30}$

The samples were then removed from the electrolyte and submerged in nanopure water for at least 10 minutes. Once they were then removed from the water and placed on a quartz plate, the samples were heat-treated at different temperatures to obtain different ligament diameters. Ligament diameters were obtained by examining heat-treated nanoporous gold in a Zeiss Auriga SEM and using Aquami (Stuckner et al. 2017) to analyze the ligaments.

After the heat-treatment the samples were cooled before being epoxied onto a tensile stage and an Interface SMA-25 mini s-type load cell. An Epsilon Technology Corporation miniature extensometer was also epoxied onto the tensile stage and load cell as seen in Figure 5.3. The epoxy was allowed to dry overnight. The sample was then extended at 1 μm/s while extensometer and load cell data were recorded.
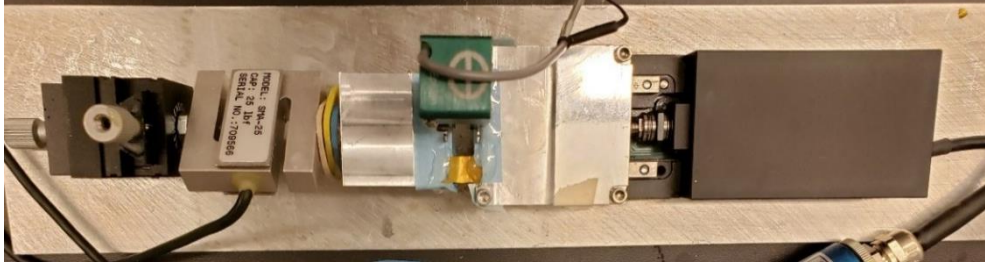
Figure 5.3: Experimental Setup Showing the Extensometer and Nanoporous
Gold Sample Epoxied to the Load Cell, Left, and Tensile Stage, Right.

5.2 Results and Discussion

Representative SEM images for each heat treatment and the corresponding

histogram of ligament diameters obtained through Aquami can be seen in Figure 5.4 for

the 12 μm thick samples and Figure 5.5 for the 50 μm thick samples.  The average

ligament sizes, rounded to the nearest 5 nm, for each heat treatment are presented in

Table 5.1.

| Sample Thickness (microns) | Heat Treatment Temperature (C) | Mean Ligament Diameter (nm) | Full Width Half Max (Gaussian Fit) | Weibull Shape Parameter | Standard Deviation |
|---|---|---|---|---|---|
| 12 | 450 | 150 ±62 | 87 ±10 | 2.56 | 62.0 |
| 12 | 475 | 215 ±101 | 194 ±21 | 2.25 | 101.5 |
| 12 | 525 | 250 ±107 | 179 ±19 | 2.45 | 107.3 |
| 12 | 550 | 295 ±93 | 189 ±17 | 3.46 | 92.8 |
| 50 | 400 | 100 ±41 | 61 ±5 | 2.48 | 41.3 |
| 50 | 450 | 150 ±48 | 97 ±4 | 3.7 | 44.8 |
| 50 | 500 | 200 ±80 | 124 ±7 | 2.6 | 81.8 |

Table 5.1: Heat Treatment Temperatures and the Mean Ligament Diameter,
Rounded to the Nearest Five Nanometers, Resulting From a Heat Treatment at
the Corresponding Temperature for Ten Minutes.  Also Given Are the Full Width
Half Max Values for a Gaussian Fit to the Histograms Presented in Figure4.3 and
4.4 As Well As the Weibull Shape Parameter for Those Histograms
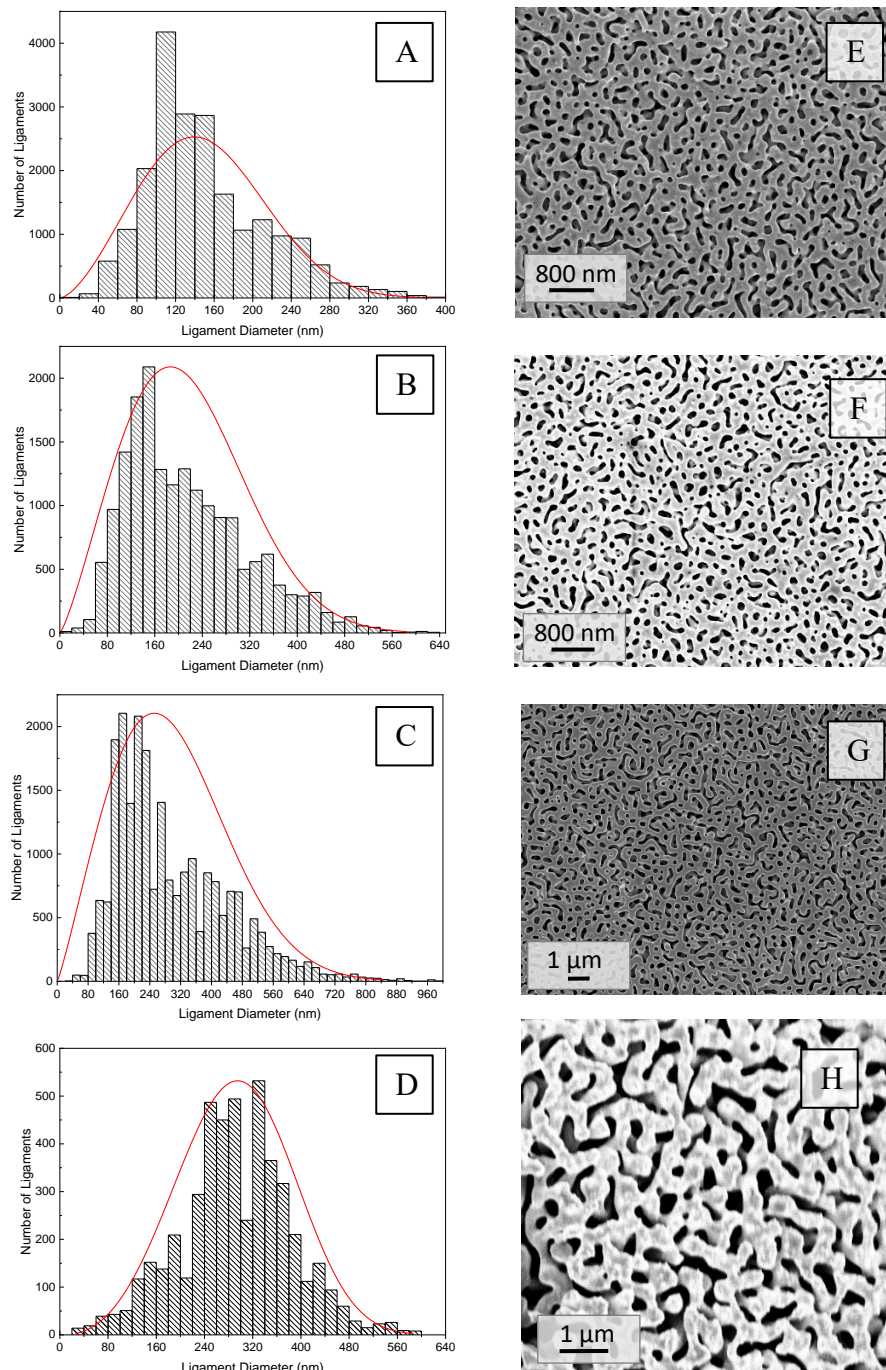
Figure 5.4: Histogram Distributions of Ligament Diameters Overlaid with a Weibull Distribution (red) of 12 µm Thick Samples of Nanoporous Gold Heat Treated at (A) 450° C, (B) 475° C, (C) 525° C, and (D) 550° C and the Corresponding SEM Images (E), (F), (G), and (H).
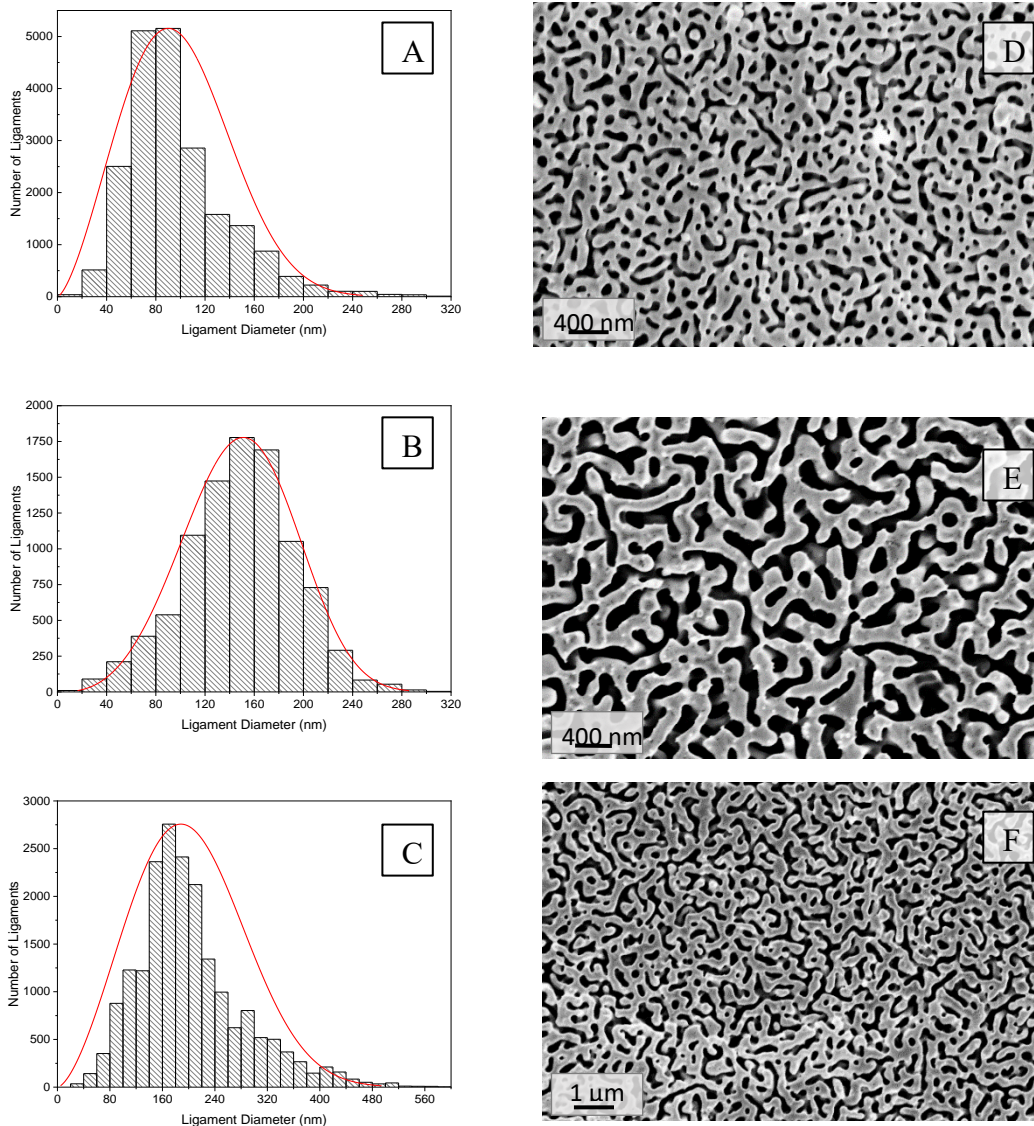
Figure 5.5: Histogram Distributions of Ligament Diameters Overlaid with a Weibull distribution (red) of 50 µm Thick Samples of Nanoporous Gold Heat Treated at (A) 400° C, (B) 450° C, and (C) 500° C, and the Corresponding SEM Images (D), (E), and (F).

The fit overlaid on the histograms is a Weibull distribution. The corresponding

Weibull shape parameters are listed in Table 5.1. These are similar to those found by

Badwe et al. (Nilesh Badwe, Chen, and Sieradzki 2017). Badwe et al. found Weibull

shape parameters between 2.35 and 3.18 for heat treated nanoporous gold samples 125 µm in thickness with average ligament diameters between 30 and 741 nm.



Figure 5.6: Representative Stress-Strain Curves for 50 µm Thick Nanoporous Gold with Average Ligament Diameters of 200 nm (Red), 150 nm (Grey), and 100 nm (Green)

Stress-strain curves representative of those obtained at each ligament size for the 50 µm thick samples are presented in Figure 5.6. The 100 nm ligament sample shows fairly linear behavior, but still has some curvature and a max stress of 7.1 MPa. The 150 nm ligament size shows some signs of curvature. The 150 nm ligament exhibits more curvature than the 100 nm ligament sample and has a max stress of 6.3 MPa. The 200 nm ligament sample shows ductile behavior and a max stress of 11.6 MPa. These max stress values are consistent with those obtained by Badwe et al. (Nilesh Badwe, Chen, and Sieradzki 2017). Badwe et al. observed max stress values between 10 and 20 MPa for

95

125 µm thick samples of nanoporous gold with ligament diameters ranging from 223 nm
to 742 nm.

Badwe et al. observed that the transition from brittle to ductile behavior occurred
at an average ligament diameter of ~220 nm (Nilesh Badwe, Chen, and Sieradzki 2017).
Based on the argument presented in the introduction of this section, it was expected that
for a sample thickness of 50 µm a ligament diameter of 200 nm would show curvature
which is consistent with the results.  Similarly, it was anticipated that a ligament diameter
of 100 nm would be borderline between linear and curved.
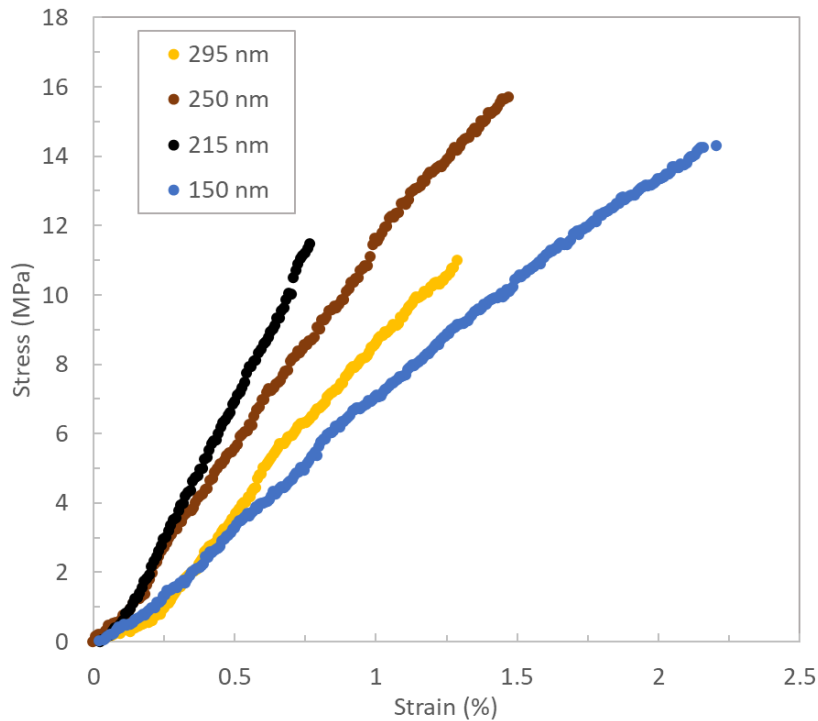


Figure 5.7: Representative Stress-Strain Curves for 12 µm Thick Nanoporous
Gold with Average Ligament Diameters of 295 nm (Yellow), 250 nm (Brown),
215 nm (Black), and 150 nm (Blue).
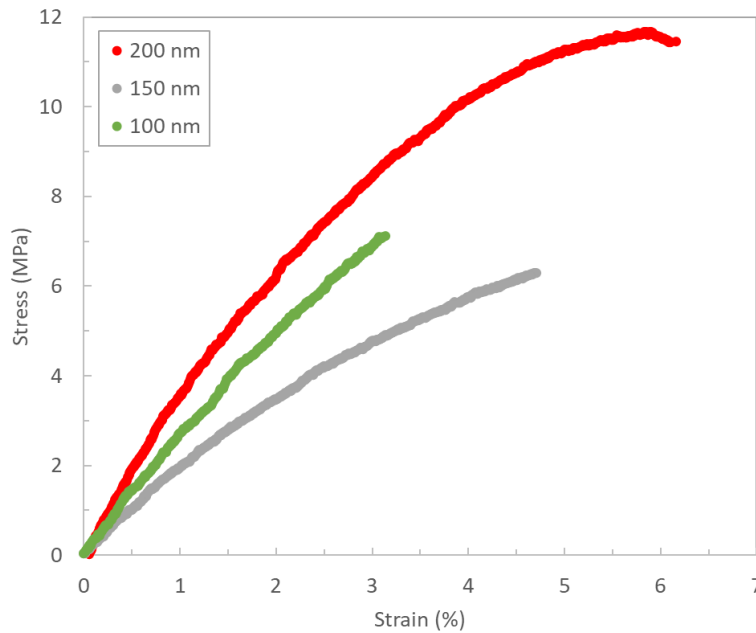
Examining the 12 µm thick samples proved more difficult.  Stress-strain curves
representative of those obtained at each ligament size for the 12 µm thick samples are

presented in Figure 5.7. For all four of the examined ligament sizes, 150, 215, 250, and 300 nm, the behavior is linear. The slopes from the curves are 700 MPa, 2GPa, 1 GPa, and 900 MPa respectively with corresponding max stress values of 14.3 MPa, 11.3 MPa, 15.7 MPa, and 10.7 MPa. This brittle behavior is unexpected based on the observations of Badwe et al. and the experiments on the 50 μm thick samples. It was anticipated that ligaments larger than 100 nm in a 12 μm thick sample would produce ductile behavior. Indeed, ligament sizes that are large enough to produce ductile behavior in both the 125 μm and 50 μm samples continue to produce brittle behavior in the 12 μm thick samples. The max stress values are, however, consistent with those found by Badwe et al. indicating that the brittle behavior is not caused by large amounts of pre-existing cracks within the sample (Nilesh Badwe, Chen, and Sieradzki 2017).

One potential explanation for this behavior is the connectivity of the nanoporous gold. Li et al. found that coarsening nanoporous gold by heat treatment results in a loss of connectivity when the solid fraction is less than 30% (Y. Li et al. 2019). More coarsening results in more loss of connectivity. Notably the nanoporous gold presented here underwent heat treatments that are not particularly long, only ten minutes. Due to being substantially thinner, the interior of the 12 μm samples will take less time than the 50 and 125 μm samples to come to temperature during heat treatment. In this manner the 12 μm samples can lose more connectivity on the interior compared to that of the 50 and 125 μm samples.

The argument presented in the introduction to this section assumes that the only thing that changes is the ligament diameter and the sample thickness. This change in connectivity is not accounted for. The full width half max values of a Gaussian fit to the

ligament size distribution can also be interrogated. The width of the distributions show similar behavior with the 12 μm samples showing wider distributions than the 50 μm samples. This indicates that the connectivity may have been impacted more by the heat treatment in the thinner samples and may be the source of the brittle behavior.

4.3 Conclusion

Samples 50 μm thick showed curvature in their stress-strain curves for an average ligament diameter of 200 nm and more linear, but still curved behavior for an average ligament diameter of 100 nm, in line with expectations. Samples 12 μm thick only showed linear behavior for ligaments ranging from 150 to 295 nm. Max stress values indicate that the linear behavior is not due to pre-existing cracks in the nanoporous gold. The width of the Gaussian fit of the distribution indicate that the 12 μm samples may be experiencing a greater loss of connectivity than the thicker samples.

Ultimately using the 50 μm samples, it can be concluded that sample thickness in relation to the ligament size affects the behavior of nanoporous gold. The results from the 12 μm samples suggest that the connectivity of the nanoporous gold also may play a role in the behavior.

CHAPTER 6

CONCLUSIONS AND FUTURE WORK

6.1 Conclusions

This thesis has been focused on nanoporous gold. Herein we examined effects of ordering on the morphology and grain structure of nanoporous gold. Then we provided evidence for a potential mechanism of stress-corrosion cracking using the nanoporous gold, silver-gold system.

In Chapter 2 we explored the effects of a phase change during dealloying on the grain structure and morphology of a copper-gold binary alloy and compared it to the grain structure of copper-gold at the same composition before and after dealloying without a phase change. This was accomplished by establishing a dealloying and handling protocol that enabled EBSD on as-dealloyed nanoporous gold. The phase change from ordered $L1_2$ to FCC did not substantially change the grain structure of the material. The disordered material, which did not undergo a phase change, also did not show significant change to the grain structure before and after dealloying. We were also able to apply the protocol to silver-gold samples. Silver-gold does not undergo a phase change during dealloying and predictably also retains its grain structure. In addition to the EBSD, digital image correlation with the software Aquami (Stuckner et al. 2017) was performed on nanoporous gold dealloyed from ordered and disordered copper-gold. The morphologies were shown to be very similar, with the only quantitative difference being the mean diameter. The difference was small enough not to be statistically significant. Based on the digital image correlation and EBSD results we conclude that the

nanoporous gold morphology is fairly robust and indifferent to some variations in surface diffusion and phase.

In Chapter 3 we provided statistical evidence that, in a polycrystal silver-gold alloy, a crack injection event travels beyond the depth of corrosion, even in a grain boundary. We concluded that a crack injection can be started in a porous grain boundary and continue into a parent grain boundary when corrosion and tensile stress are separated in time. Then further polycrystal silver-gold experiments were performed where current during stress-corrosion cracking was monitored. Current transients were seen and their frequency was found to increase with increasing applied initial stress. Based on these experiments, we concluded that stress-corrosion cracking can be composed of crack injection events rather than a continuous process. This supports the film-induced cleavage model for stress-corrosion cracking.

Chapter 4 focused on crack injection events in transgranular stress-corrosion fracture. To examine the relationship between stress-corrosion and crack-injection events further, crack-injection and stress-corrosion cracking fracture surfaces for single-crystal silver-gold samples were compared. For two different tensile orientations, the fracture surfaces of the injection and stress-corrosion are crystallographically similar. This provides evidence that crack-injection can be a mechanism for stress-corrosion.

Chapter 5 examined sample size effects in nanoporous gold. Samples 50 μm thick showed curvature for an average ligament diameter of 200 nm. For an average ligament diameter of 100 nm the behavior is more linear but still shows some curvature indicating it is close to the transition ligament size. Samples 12 μm thick only showed brittle behavior for ligaments ranging from 150 to 295 nm. We attributed this to a

potential loss in connectivity of the nanoporous gold in thinner samples during

coarsening.

6.2 Future Work

Stainless steels specifically are of interest. Porosity, morphologically similar to

that in NPG, may form in the sensitized stainless steel where Cr is depleted, specifically

in the sensitized grain boundaries and the region near these grain boundaries. The

theories and models describing the formation of electrochemical-dealloying induced

porosity were not well developed when room temperature, stainless steel, stress-corrosion

research was occurring (prior to the 1980's) (A.J.Forty 1979; Pickering 1983). Since the

1980's, research on SCC in sensitized stainless steel has focused on higher temperatures

($\sim 300°$ C) similar to those seen in nuclear power reactors (Kritzer 2004). As such, there is

still a lot to understand about SCC in stainless steels at room temperature. Understanding

the room temperature mechanisms can aid in understanding high temperature research.

In sensitized stainless steels the concentrations of Cr in the grain boundaries are

affected by both the C content and sensitization temperature and time(Jones 1996a); these

concentrations can dip below $\sim 10$ at%. The depletion of Cr is not limited to the grain

boundaries, however. Within 10 nm of the grain boundary, measured perpendicularly to

the boundary, the Cr concentration will be $\leq 13$ at% and the gradient will extend $\sim 30$ nm

out perpendicularly from the boundary (Wells et al. 1992; Y. H. Lu et al. 2005). It is well

known that 12 at% Cr is required for passivation in stainless steels (Jones 1996b) and

because the concentrations of Cr in the grain boundary and a region around the grain

101

boundary lie below this, the grain boundaries are susceptible to electrochemical dealloying and have the potential for porosity formation.

A correlation between homologous temperature and pore size has been established in recent research (McCue, Karma, and Erlebacher 2018; Q. Chen and Sieradzki 2013). This correlation indicates that a pore size of approximately 1-2 nm would be expected in a sensitized stainless steel system; this is further validated Deakin, Zong, Lynch and Newman (Deakin et al. 2004). Other work by Newman et al. shows that, in sodium thiosulfate, intergranular cracking rates in 304 sensitized stainless steel grain boundaries were two orders of magnitude larger than what Faraday's law predicted for a "bare surface" of the composition found in the grain boundaries (Fe9Cr10Ni) (R. C. Newman, Sieradzki, and Isaacs 1982). However, it is important to note that in these constant extension rate tests, martensite forms at room temperature due to strain. Furthermore, the sodium thiosulfate can convolute things because it has a disproportionation reaction; specifically, reduction which causes the chemisorption of sulfur catalyzing dissolution of iron and nickel and potentially causing hydrogen embrittlement of the martensite. Therefore, hydrogen embrittlement cannot be ruled out as the difference between the experimental bare surface and 304 cracking rate.

Aberration-corrected STEM should be used to examine both high and low angle grain boundaries from 304 stainless steel samples before and after they are sensitized as well as following electrochemical dissolution experiments to compare the Cr concentration and morphology before sensitization, after sensitization, and after electrochemical dissolution. The post-dissolution grain boundaries should be examined for evidence of porosity. If porosity is confirmed, experiments examining the extent of

porosity down the grain boundary, similar to those in Section 3.1, should be performed.

Then crack-injection experiments can be performed, like those done by Badwe on

polycrystal silver-gold, to examine the ability of a crack to be injected from a porous

grain-boundary into a parent grain-boundary (Nilesh Badwe, Chen, and Sieradzki 2017).

Binary copper-manganese alloys are known to produce nanoporous copper

through electrochemically induced dealloying.  Hayes et al. showed that the ligament size

can be varied by varying the dealloying conditions (free corrosion versus potentiostatic,

varying electrolytes) (Hayes et al. 2006).  Much the same as silver-gold, the copper-

manganese alloy is FCC and copper, like gold, is also FCC.  Thus during the dealloying

process there is no phase change from parent to porosity.  This coupled with the

knowledge that copper-zinc undergoes stress-corrosion cracking leads us to believe that

copper manganese can exhibit stress-corrosion cracking the same way silver-gold can.

The material cost for copper-manganese is much lower than silver-gold which allows for

larger samples as well as more samples compared to silver-gold.  Thicker samples would

be beneficial for both the current transient experiments, in Section 3.2, as well as the

sample size effect experiments, in Chapter 5.

In the case of current transient experiments, thicker samples increase the

likelihood of achieving large crack-injection events as well as multiple consecutive large

crack-injection events.  A well-defined number of crack-injection events leading to

through thickness fracture allows for a better estimation of crack-injection distance.  For

sample size effects, small samples are fragile and difficult to work with.  The thicker

samples of copper-manganese would allow for a larger size sample size range than was

feasible for silver-gold and therefore a more complete picture of the relationship between

sample thickness and ligament size as it relates to the fracture behavior.

REFERENCES

A.J.Forty. 1979. "Corrosion Micromorphology of Noble Metal Alloys and Depletion Gilding." *Nature* 282 (December): 597–98. https://www.nature.com/articles/282597a0.pdf.

Achenbach, J. D., and J. G. Harris. 1979. "Acoustic Emission from a Brief Crack Propagation Event." *Journal of Applied Mechanics, Transactions ASME* 46 (1): 107–12. https://doi.org/10.1115/1.3424480.

Ahn, Phillip, and Oluwaseyi Balogun. 2014. "Elastic Characterization of Nanoporous Gold Foams Using Laser Based Ultrasonics." *Ultrasonics* 54 (3): 795–800. https://doi.org/10.1016/j.ultras.2013.10.004.

Andresen, Peter L., and F. Peter Ford. 1988. "Life Prediction by Mechanistic Modeling and System Monitoring of Environmental Cracking of Iron and Nickel Alloys in Aqueous Systems." *MateriaLs Science and Engineering: A* 103 (1): 167–84. https://doi.org/10.1016/0025-5416(88)90564-2.

Andrews, E. H. 1959. "Stress Waves and Fracture Surfaces." *Journal of Applied Physics* 30 (5): 740–43. https://doi.org/10.1063/1.1735224.

Artymowicz, D. M., J. Erlebacher, and R. C. Newman. 2009. "Relationship between the Parting Limit for De-Alloying and a Particular Geometric High-Density Site Percolation Threshold." *Philosophical Magazine* 89 (21): 1663–93. https://doi.org/10.1080/14786430903025708.

Atkinson, C., and J. D. Eshelby. 1968. "The Flow of Energy into the Tip of a Moving Crack." *International Journal of Fracture Mechanics* 4 (1): 3–8. https://doi.org/10.1007/BF00189137.

Badwe, N., X. Chen, D. K. Schreiber, M. J. Olszta, N. R. Overman, E. K. Karasz, A. Y. Tse, S. M. Bruemmer, and K. Sieradzki. 2018. "Decoupling the Role of Stress and Corrosion in the Intergranular Cracking of Noble-Metal Alloys." *Nature Materials*. https://doi.org/10.1038/s41563-018-0162-x.

Badwe, Nilesh. 2014. "Fracture of Nanoporous Gold." Arizona State University.

Badwe, Nilesh, Xiying Chen, and Karl Sieradzki. 2017. "Mechanical Properties of Nanoporous Gold in Tension." *Acta Materialia* 129: 251–58. https://doi.org/10.1016/j.actamat.2017.02.040.

Balk, T. John, Chris Eberl, Ye Sun, Kevin J. Hemker, and Daniel S. Gianola. 2009. "Tensile and Compressive Microspecimen Testing of Bulk Nanoporous Gold." *TMS JOM* 61 (12): 26–31.

Baranowski, B., S. Majchrzak, and T. B. Flanagan. 1971. "The Volume Increase of Fcc

Metals and Alloys Due to Interstitial Hydrogen over a Wide Range of Hydrogen Contents." *Journal of Physics F: Metal Physics* 1 (3): 258–61. https://doi.org/10.1088/0305-4608/1/3/307.

Barnes, Andrew, Nicholas A. Senior, and Roger C. Newman. 2009. "Film-Induced Cleavage of Ag-Au Alloys." *Metallurgical and Materials Transactions A: Physical Metallurgy and Materials Science* 40 (1): 58–68. https://doi.org/10.1007/s11661-008-9714-z.

Beachem, C. D. 1972. "A New Model for Hydrogen-Assisted Cracking (Hydrogen 'Embrittlement')." *Metallurgical Transactions* 3: 437–51.

Biener, Juergen, Andrea M. Hodge, and Alex V. Hamza. 2005. "Microscopic Failure Behavior of Nanoporous Gold." *Applied Physics Letters* 87 (12): 1–3. https://doi.org/10.1063/1.2051791.

Biener, Juergen, Andrea M. Hodge, Joel R. Hayes, Cynthia A. Volkert, Luis A. Zepeda-Ruiz, Alex V. Hamza, and Farid F. Abraham. 2006. "Size Effects on the Mechanical Behavior of Nanoporous Au." *Nano Letters* 6 (10): 2379–82. https://doi.org/10.1021/nl061978i.

Binnig, G., and H. Rohrer. 1986. "Scanning Tunneling Microscopy." *IBM Journal of Research and Development* 30 (4): 355–69.

Birnbaum, H. K. 1984. "Mechanical Properties of Metal Hydrides." *Journal of The Less-Common Metals* 104 (1): 31–41. https://doi.org/10.1016/0022-5088(84)90433-8.

Birnbaum, H. K., and P. Sofronis. 1994. "Hydrogen-Enhanced Localized Plasticity-a Mechanism for Hydrogen-Related Fracture." *Materials Science and Engineering A* 176: 191–202. https://doi.org/10.1016/0921-5093(94)90975-X.

Briot, Nicolas J., Tobias Kennerknecht, Christoph Eberl, and T. John Balk. 2014. "Mechanical Properties of Bulk Single Crystalline Nanoporous Gold Investigated by Millimetre-Scale Tension and Compression Testing." *Philosophical Magazine* 94 (8): 847–66. https://doi.org/10.1080/14786435.2013.868944.

Cahn, John W. 1959. "Free Energy of a Nonuniform System. II. Thermodynamic Basis." *The Journal of Chemical Physics* 30 (5): 1121–24. https://doi.org/10.1063/1.1730145.

Cahn, Robert W. 1997. "Percolation Frustrated." *Nature* 389 (6647): 121–22. https://doi.org/10.1038/38113.

Chen-Wiegart, Yu Chen Karen, Steve Wang, Yong S. Chu, Wenjun Liu, Ian McNulty, Peter W. Voorhees, and David C. Dunand. 2012. "Structural Evolution of Nanoporous Gold during Thermal Coarsening." *Acta Materialia* 60 (12): 4972–81. https://doi.org/10.1016/j.actamat.2012.05.012.

Chen, J. S. 1992. "Brittle Fracture of Cu-30 Au Induced by a Surface Layer." *Journal of The Electrochemical Society* 139 (6): L55. https://doi.org/10.1149/1.2069496.

Chen, J. S., M. Salmeron, and T. M. Devine. 1992. "Intergranular vs Transgranular Stress Corrosion Cracking of Cu 30-Au." *Scripta Metallurgica et Materiala* 26: 739–42.

———. 1993. "Intergranular and Transgranular Stress Corrosion Cracking of Cu30Au." *Corrosion Science* 34 (12): 2071–97. https://doi.org/10.1016/0010-938X(93)90061-K.

Chen, Qing, and Karl Sieradzki. 2013. "Spontaneous Evolution of Bicontinuous Nanostructures in Dealloyed Li-Based Systems." *Nature Materials* 12 (12): 1102–6. https://doi.org/10.1038/nmat3741.

Chen, Xiying. 2016. "Crack Injection in Silver Gold Alloys." Arizona State University.

Chen, Xiying, Erin K. Karasz, Nilesh Badwe, and Karl Sieradzki. 2020. "Dynamic Fracture and Dealloying Induced Stress-Corrosion Cracking." *Under Review*.

Deakin, Jane, Zehua Dong, Benjamin Lynch, and Roger C. Newman. 2004. "De-Alloying of Type 316 Stainless Steel in Hot, Concentrated Sodium Hydroxide Solution." *Corrosion Science* 46 (9): 2117–33. https://doi.org/10.1016/j.corsci.2004.01.011.

Detsi, E., M. Van De Schootbrugge, S. Punzhin, P. R. Onck, and J. T.M. De Hosson. 2011. "On Tuning the Morphology of Nanoporous Gold." *Scripta Materialia* 64 (4): 319–22. https://doi.org/10.1016/j.scriptamat.2010.10.023.

Ding, Yi, Young Ju Kim, and Jonah Erlebacher. 2004. "Nanoporous Gold Leaf: "Ancient Technology "/Advanced Material." *Advanced Materials* 16 (21): 1897–1900. https://doi.org/10.1002/adma.200400792.

Dulaney, E. N., and W. F. Brace. 1960. "Velocity Behavior of a Growing Crack." *Journal of Applied Physics* 31 (12): 2233–36. https://doi.org/10.1063/1.1735529.

Dursun, Aziz, Dylan V. Pugh, and Scan G. Corcoran. 2003. "A Steady-State Method for Determining the Dealloying Critical Potential." *Electrochemical and Solid-State Letters* 6 (8): 32–35. https://doi.org/10.1149/1.1588111.

Dursun, Aziz, Dylan V. Pugh, and Sean G. Corcoran. 2005. "Probing the Dealloying Critical Potential." *Journal of The Electrochemical Society* 152 (2): B65. https://doi.org/10.1149/1.1848351.

Edeleanu, C., and A. J. Forty. 1960. "Some Observations on the Stress-Corrosion Cracking of α-Brass and Similar Alloys." *Philosophical Magazine*. https://doi.org/10.1080/14786436008235881.

Erlebacher, Jonah. 2004. "An Atomistic Description of Dealloying." *Journal of The*

*Electrochemical Society* 151 (10): C614. https://doi.org/10.1149/1.1784820.

Erlebacher, Jonah, Michael J. Aziz, Alain Karma, Nikolay Dimitrov, and Karl Sieradzki. 2001. "Evolution of Nanoporosity in Dealloying." *Nature* 410 (6827): 450–53. https://doi.org/10.1038/35068529.

Fineberg, Jay, Steven P Gross, M Marder, and Harry L Swinney. 1992. "Instability in the Propagation of Fast Cracks." *Physical Review B* 45 (10): 5146–54. https://doi.org/10.1126/science.284.5418.1233d.

Flanagan, Ted B., and H. Noh. 1995. "A Possible Role for Hydrogen-Induced Lattice Migration in Alloy Materials Processing." *Journal of Alloys and Compounds* 231 (1–2): 1–9. https://doi.org/10.1016/0925-8388(96)80003-X.

Ford, F P. 1984. "Current Understanding of the Mechanisms of Stress Corrosion and Corrosion Fatigue." In *Environment-Sensitive Fracture: Evaluation and Comparison of Test Methods, ASTM STP 821*, edited by S W Dean, E N Pugh, and G M Ugiansky, 32–51. Philadelphia: American Society for Testing and Materials.

Freund, L. B. 1972. "Energy Flux into the Tip of an Extending Crack in an Elastic Solid." *Journal of Elasticity* 2 (4): 341–49. https://doi.org/10.1007/BF00045718.

Freund, L B. 1986. "The Mechanics of Dynamic Fracture." *Tenth U. S. National Congress of Applied Mechanics*, 49.

Friedersdork, F., and K. Sieradzki. 1996. "Film-Induced Brittle Intergranular Cracking of Silver-Gold Alloys." *Corrosion Science* 52 (5): 331–36.

Fujita, Takeshi, Pengfei Guan, Keith McKenna, Xingyou Lang, Akihiko Hirata, Ling Zhang, Tomoharu Tokunaga, et al. 2012. "Atomic Origins of the High Catalytic Activity of Nanoporous Gold." *Nature Materials* 11 (9): 775–80. https://doi.org/10.1038/nmat3391.

Fujita, Takeshi, Tomoharu Tokunaga, Ling Zhang, Dongwei Li, Luyang Chen, Shigeo Arai, Yuta Yamamoto, et al. 2014. "Atomic Observation of Catalysis-Induced Nanopore Coarsening of Nanoporous Gold." *Nano Letters* 14 (3): 1172–77. https://doi.org/10.1021/nl403895s.

Fukai, Y., M. Mizutani, S. Yokota, M. Kanazawa, Y. Miura, and T. Watanabe. 2003. "Superabundant Vacancy-Hydrogen Clusters in Electrodeposited Ni and Cu." *Journal of Alloys and Compounds* 356–357: 270–73. https://doi.org/10.1016/S0925-8388(02)01270-7.

Fukai, Y., K. Mori, and H. Shinomiya. 2003. "The Phase Diagram and Superabundant Vacancy Formation in Fe-H Alloys under High Hydrogen Pressures." *Journal of Alloys and Compounds* 348 (1–2): 105–9. https://doi.org/10.1016/S0925-8388(02)00806-X.

Fukai, Y, and M. Mizutani. 2002. "Phase Diagram, and Superabundant Vacancy Formation in Cr-H Alloys." *Materials Transactions* 43 (5): 1079–84.

Fukai, Yuh. 2003. "Formation of Superabundant Vacancies in M-H Alloys and Some of Its Consequences: A Review." *Journal of Alloys and Compounds* 356–357: 263–69. https://doi.org/10.1016/S0925-8388(02)01269-0.

Fukai, Yuh, and Nobuyuki Okuma. 1993. "Evidence of Copious Vacancy Formation in Ni and Pd under a High Hydrogen Pressure." *Japanese Journal of Applied Physics* 32 (9): L1256–59. https://doi.org/10.1143/JJAP.32.L1256.

Fukai, Yuh, and Hidehiko Sugimoto. 2007. "Formation Mechanism of Defect Metal Hydrides Containing Superabundant Vacancies." *Journal of Physics Condensed Matter* 19: 1–24. https://doi.org/10.1088/0953-8984/19/43/436201.

Fukai, Yuh, Saori Yokota, and Jun'ichi Yanagawa. 2006. "The Phase Diagram and Superabundant Vacancy Formation in Co-H Alloys." *Journal of Alloys and Compounds* 407 (1–2): 16–24. https://doi.org/10.1016/j.jallcom.2005.06.016.

Galvele, J. R. 1993. "Surface Mobility Mechanism of Stress-Corrosion Cracking." *Corrosion Science* 35: 419–34. https://doi.org/10.1016/0010-938X(94)90072-8.

Galvele, Jose R. 1987. "A Stress Corrosion Cracking Mechanism Based on Surface Mobility." *Corrosion Science* 27 (1): 1–33. https://doi.org/10.1016/0010-938X(87)90117-X.

Garg, Sabodh K., and Julius Siekmann. 1966. "Cranz-Schardin Multisource Spark Camera Systems." *Review of Scientific Instruments* 37 (8): 1032–33. https://doi.org/10.1063/1.1720399.

Gavriljuk, V. G., V. N. Bugaev, Yu N. Petrov, A. V. Tarasenko, and B. Z. Yanchitski. 1996. "Hydrogen-Induced Equilibrium Vacancies in FCC Iron-Base Alloys." *Scripta Materialia* 34 (6): 903–7. https://doi.org/10.1016/1359-6462(95)00580-3.

Geng, Ke, Minglu Liu, Yusi Xie, Ashlee Aiello, Erin Karasz, and Karl Sieradzki. 2019. "Morphology Evolution during Delithiation of Li-Pb Alloys: Oscillatory Electrochemical Behavior." *Journal of The Electrochemical Society* 166 (6): C108–14. https://doi.org/10.1149/2.0161906jes.

Giaever, Ivar. 1960. "Energy Gap in Superconductors Measured by Electron Tunneling." *Physical Review Letters* 5 (4): 147–48. https://doi.org/10.1103/PhysRevLett.5.147.

Gilman, John J. 1956. "Propagation of Cleavage Cracks in Crystals." *Journal of Applied Physics* 27 (11): 1262–69. https://doi.org/10.1063/1.1722249.

Gittard, Shaun D., Bonnie E. Pierson, Cindy M. Ha, Chung An Max Wu, Roger J. Narayan, and David B. Robinson. 2010. "Supercapacitive Transport of

Pharmacologic Agents Using Nanoporous Gold Electrodes." *Biotechnology Journal* 5 (2): 192–200. https://doi.org/10.1002/biot.200900250.

Goldman, Tamar, Ariel Livne, and Jay Fineberg. 2010. "Acquisition of Inertia by a Moving Crack." *Physical Review Letters* 104 (11): 5–8. https://doi.org/10.1103/PhysRevLett.104.114301.

Greer, Julia R., and William D. Nix. 2006. "Nanoscale Gold Pillars Strengthened through Dislocation Starvation." *Physical Review B - Condensed Matter and Materials Physics* 73 (24): 1–6. https://doi.org/10.1103/PhysRevB.73.245410.

Griffith, A . A . 1921. "The Phenomena of Rupture and Flow in Solids." *Philosophical Transactions of the Royal Society of London. Series A, Containing Papers of a Mathematical or Physical Character* 221 (1921): 163–98.

Hahn, G. T., and A. R. Rosenfield. 1965. "Local Yielding and Extension of a Crack under Plane Stress." *Acta Metallurgica* 13 (3): 293–306. https://doi.org/10.1016/0001-6160(65)90206-3.

Hahn, M. T., and E. N. Pugh. 1980. "The Use of Load Pulsing in the Interpretation of Transgranular Stress-Corrosion Fracture Surfaces in a Type 310S Stainless Steel." *Corrosion* 36 (7): 380–82.

Hakamada, Masataka, and Mamoru Mabuchi. 2006. "Nanoporous Gold Prism Microassembly through a Self-Organizing Route." *Nano Letters* 6 (4): 882–85. https://doi.org/10.1021/nl0602443.

———. 2008. "Microstructural Evolution in Nanoporous Gold by Thermal and Acid Treatments." *Materials Letters* 62 (3): 483–86. https://doi.org/10.1016/j.matlet.2007.05.086.

Hall, M. M. 2008. "Crack Tip Strain Rate Equation with Applications to Crack Tip Embrittlement and Active Path Dissolution Models of Stress Corrosion Cracking." In *Environment-Induced Cracking of Materials, Volume 1 - Chemistry, Mechanics and Mechanisms*, edited by Sergei Shipilov, Russell Jones, Jean-Marc Olive, and Raul Rebak, 59–68. Elsevier. https://doi.org/10.1016/B978-008044635-6.50008-X.

Hayes, J. R., A. M. Hodge, J. Biener, A. V. Hamza, and K. Sieradzki. 2006. "Monolithic Nanoporous Copper by Dealloying Mn-Cu." *Journal of Materials Research* 21 (10): 2611–16. https://doi.org/10.1557/jmr.2006.0322.

Herring, Conyers. 1950. "Effect of Change of Scale on Sintering Phenomena." *Journal of Applied Physics* 21 (4): 301–3. https://doi.org/10.1063/1.1699658.

Hodge, A. M., J. Biener, J. R. Hayes, P. M. Bythrow, C. A. Volkert, and A. V. Hamza. 2007. "Scaling Equation for Yield Strength of Nanoporous Open-Cell Foams." *Acta Materialia* 55 (4): 1343–49. https://doi.org/10.1016/j.actamat.2006.09.038.

110

Hutchinson, J.W. 1968. "Singular Behaviour at the End of a Tensile Crack in a Hardening Material." *Journal of the Mechanics and Physics of Solids* 16: 13–31.

Iwamoto, Maswanao, and Y Fukai. 1999. "Superabundant Vacancy Formation in Iron under High Hydrogen Pressures: Thermal Desorption Spectroscopy." *Materials Transactions, JIM* 40 (7): 606–11.

Jeer, Leo T.H. De, Diego Ribas Gomes, Jorrit E. Nijholt, Rik Van Bremen, Václav Ocelík, and Jeff Th M. De Hosson. 2015. "Formation of Nanoporous Gold Studied by Transmission Electron Backscatter Diffraction." *Microscopy and Microanalysis* 21 (6): 1387–97. https://doi.org/10.1017/S1431927615015329.

Jin, Hai Jun, Lilia Kurmanaeva, Jörg Schmauch, Harald Rösner, Yulia Ivanisenko, and Jörg Weissmüller. 2009. "Deforming Nanoporous Metal: Role of Lattice Coherency." *Acta Materialia* 57 (9): 2665–72. https://doi.org/10.1016/j.actamat.2009.02.017.

Jin, Hai Jun, and Jörg Weissmüller. 2011. "A Material with Electrically Tunable Strength and Flow Stress." *Science* 332 (6034): 1179–82. https://doi.org/10.1126/science.1202190.

Jones, Denny A. 1996a. "Intergranular Corrosion of Austenitic Stainless Steels." In *Principles and Prevention of Corrosion*, edited by Bill Stenquist, Rose Kernan, and Patricia Daly, Second Edi, 292–304. Upper Saddle River: Prentice-Hall, Inc.

———. 1996b. "Passive Films." In *Principles and Prevention of Corrosion*, 2nd ed., 116–18. Upper Saddle River.

Jurgens, Birte, Christian Kubel, Christian Schulz, Tobias Nowitzki, Volkmar Zielasek, Jurgen Biener, Monika M. Biener, Alex V. Hamza, and Marcus Baumer. 2007. "New Gold and Silver-Gold Catalysts in the Shape of Sponges and Sieves." *Gold Bulletin*.

Kelly, R.G., A.J. Frost, T. Shahrabi, and R. C. Newman. 1991. "Brittle-Fracture of an Au/Ag Alloy Induced by a Surface-Film." *Metallurgical Transactions A-Physical Metallurgy and Materials Science* 22 (2): 531–41.

Kerkhof, F. 1973. "Wave Fractographic Investigations of Brittle Fracture Dynamics." In *Proceedings of an International Conference on Dynamic Crack Propagation*, 3–35. Dodrecht: Springer.

Kertis, F., J. Snyder, Lata Govada, Sahir Khurshid, N. Chayen, and J. Erlebacher. 2010. "Structure/Processing Relationships in the Fabrication of Nanoporous Gold." *TMS JOM* 62 (6): 50–56.

Kritzer, Peter. 2004. "Corrosion in High-Temperature and Supercritical Water and Aqueous Solutions: A Review." *Journal of Supercritical Fluids* 29 (1–2): 1–29.

https://doi.org/10.1016/S0896-8446(03)00031-7.

Kuwano-Nakatani, Satoko, Takeshi Fujita, Kazuki Uchisawa, Daichi Umetsu, Yu Kase, Yusuke Kowata, Katsuhiko Chiba, et al. 2015. "Environment-Sensitive Thermal Coarsening of Nanoporous Gold." *Materials Transactions*, 1–5.

Larche, F C, and J W Cahn. 1985. "The Interactions of Composition Crystalline Solids." *Acta Metallurgica* 33 (3): 331–57. https://ac.els-cdn.com/000161608590077X/1-s2.0-000161608590077X-main.pdf?_tid=4a3bfde8-b93c-11e7-bea7-00000aacb35d&acdnat=1508905605_724ccd06d087891c8cdd42b4809628df.

Li, Dongwei, Ye Zhu, Hui Wang, and Yi Ding. 2013. "Nanoporous Gold as an Active Low Temperature Catalyst toward CO Oxidation in Hydrogen-Rich Stream." *Scientific Reports* 3: 1–7. https://doi.org/10.1038/srep03015.

Li, Rong, and K. Sieradzki. 1992. "Ductile-Brittle Transition in Random Porous Au." *Physical Review Letters* 68 (8): 1168–71. https://doi.org/10.1103/PhysRevLett.68.1168.

Li, Yong, Bao Nam Dinh Ngô, Jürgen Markmann, and Jörg Weissmüller. 2019. "Topology Evolution during Coarsening of Nanoscale Metal Network Structures." *Physical Review Materials* 3. https://doi.org/10.1103/PhysRevMaterials.3.076001.

Lichter, B. D., W. F. Flanagan, J. S. Kim, J. C. Elkenbracht, and M. Van Hunen. 1996. "Mechanistic Studies of Stress Corrosion Cracking: Application of the Corrosion-Assisted Cleavage Model to Results Using Oriented Single Crystals." *Corrosion (Houston)* 52 (6): 453–63. https://doi.org/10.5006/1.3292134.

Lochbaum, Dave. 2018. "Pipe Rupture at Surry Nuclear Plant Kills Four Workers." All Things Nuclear. 2018.

Logan, Hugh L. 1952. "Film-Rupture Mechanism of Stress Corrosion." *Journal of Research of the National Bureau of Standards* 48 (2): 99–105.

Lu, Gang, and Efthimios Kaxiras. 2005. "Hydrogen Embrittlement of Aluminum: The Crucial Role of Vacancies." *Physical Review Letters* 94 (15): 1–5. https://doi.org/10.1103/PhysRevLett.94.155501.

Lu, Y. H., Q. J. Peng, T. Sato, and T. Shoji. 2005. "An ATEM Study of Oxidation Behavior of SCC Crack Tips in 304L Stainless Steel in High Temperature Oxygenated Water." *Journal of Nuclear Materials* 347 (1–2): 52–68. https://doi.org/10.1016/j.jnucmat.2005.07.006.

Lu, Zhanpeng, and Tetsuo Shoji. 2006. "Unified Interpretation of Crack Growth Rates of Ni-Base Alloys in LWR Environments." *Journal of Pressure Vessel Technology* 128 (3): 318–27. https://doi.org/10.1115/1.2217964.

Lührs, Lukas, Birthe Zandersons, Norbert Huber, and Jörg Weissmüller. 2017. "Plastic Poisson's Ratio of Nanoporous Metals: A Macroscopic Signature of Tension-Compression Asymmetry at the Nanoscale." *Nano Letters* 17 (10): 6258–66. https://doi.org/10.1021/acs.nanolett.7b02950.

Lynch, S. P. 2011. "Hydrogen Embrittlement Phenomena and Mechanisms." In *Stress Corrosion Cracking: Theory and Practice*, edited by V. S. Raja and Tetsuo Shoji, 90–130. Philadelphia: Woodhead Publishing.

Maiti, S. K., M. F. Ashby, and L. J. Gibson. 1984. "Fracture Toughness of Brittle Cellular Solids." *Scripta Metallurgica* 18 (3): 213–17. https://doi.org/10.1016/0036-9748(84)90510-6.

Mameka, Nadiia, Jürgen Markmann, Hai Jun Jin, and Jörg Weissmüller. 2014. "Electrical Stiffness Modulation - Confirming the Impact of Surface Excess Elasticity on the Mechanics of Nanomaterials." *Acta Materialia* 76: 272–80. https://doi.org/10.1016/j.actamat.2014.04.067.

Marder, M. 1991. "New Dynamical Equation for Cracks." *Physical Review Letters* 207 (19): 2484–87. https://doi.org/10.1038/2071238d0.

Marder, Michael. 1998. "Adiabatic Equation for Cracks." *Philosophical Magazine B: Physics of Condensed Matter; Statistical Mechanics, Electronic, Optical and Magnetic Properties* 78 (2): 203–14. https://doi.org/10.1080/13642819808202942.

McCue, Ian, Alain Karma, and Jonah Erlebacher. 2018. "Pattern Formation during Electrochemical and Liquid Metal Dealloying." *MRS Bulletin* 43 (1): 27–34. https://doi.org/10.1557/mrs.2017.301.

McCue, Ian, Joshua Stuckner, Mitsu Murayama, and Michael J. Demkowicz. 2018. "Gaining New Insights into Nanoporous Gold by Mining and Analysis of Published Images." *Scientific Reports* 8 (1): 1–11. https://doi.org/10.1038/s41598-018-25122-3.

Moffat, Thomas P, Fu-ren F Fan, and Allen J Bard. 1991. "Electrochemical and Scanning Tunneling Microscopic Study of Dealloying of Cu3Au." *Journal of Electrochemical Society* 138 (11): 3224–35. https://doi.org/10.1149/1.2085396.

Movrin, Damijan. 2000. "Dealloying of Silver-Gold Alloys." Arizona State University.

Nazarov, R., T. Hickel, and J. Neugebauer. 2014. "Ab Initio Study of H-Vacancy Interactions in Fcc Metals: Implications for the Formation of Superabundant Vacancies." *Physical Review B - Condensed Matter and Materials Physics* 89 (14): 1–18. https://doi.org/10.1103/PhysRevB.89.144108.

Newman, R. C., T. Shahrabi, and K. Sieradzki. 1989. "Film-Induced Cleavage of Alpha-Brass." *Scripta Metallurgica* 23 (1): 71–74. https://doi.org/10.1016/0036-

9748(89)90095-1.

Newman, R. C., and K. Sieradzki. 1983. "Correlation of Acoustic and Electrochemical Noise in the Stress-Corrosion Cracking of Alpha-Brass." *Scripta Metallurgica* 17: 621–24.

Newman, R. C., K. Sieradzki, and H. S. Isaacs. 1982. "Stress-Corrosion Cracking of Sensitized Type 304 Stainless Steel in Thiosulfate Solutions." *Metallurgical Transactions A* 13A: 2015–26.

Newman, Roger C. 2002. "Stress-Corrosion Cracking Mechanisms." In *Corrosion Mechanisms in Theory and Practice*, edited by Philippe Marcus and J. Oudar, 2nd ed., 399–450. New York: Marcel Dekker, Inc. https://doi.org/doi:10.1201/9780203909188.ch12\r10.1201/9780203909188.ch12.

Newman, Roger C., and Christopher Healey. 2007. "Stability, Validity, and Sensitivity to Input Parameters of the Slip-Dissolution Model for Stress-Corrosion Cracking." *Corrosion Science* 49: 4040–50. https://doi.org/10.1016/j.corsci.2007.05.001.

Nickel, Rod. 2020. "Stress, Corrosion Caused 2018 Enbridge Gas Pipeline Blast: Canadian Agency." *Reuters*, March 4, 2020.

Nkemzi, Daniel. 1997. "A New Formula for the Velocity of Rayleigh Waves." *Wave Motion* 26 (2): 199–205. https://doi.org/10.1016/s0165-2125(97)00004-8.

Okamoto, By H, and T B Massalski. 1983. "The Ag-Au ( Silver-Gold ) System." *Bulletin of Alloy Phase Diagrams* 4 (1): 30–38.

Okamoto, H., D.J. Chakrabarti, and D.E. Laughin. 1987. "The Au-Cu System, Phase Diagram of Binary Gold Alloys." *Bulletin of Alloy Phase Diagrams* 8: 454.

Oppenheim, Ivette C, Dennis J Trevor, Christopher E D Chidsey, Paula L Trevor, and Karl Sieradzki. 1991. "In Situ Scanning Tunneling Microscopy of Corrosion of Silver-Gold Alloys." *Science* 254 (5032): 687–89.

Oriani, R. A. 1972. "A Mechanistic Theory of Hydrogen Embrittlement of Steels." *Berichte Der Bunsen-Gesellschaft Fur Physikalische Chemie* 76 (8): 848–57.

———. 1978. "Hydrogen Embrittlement of Steels." *Annual Review of Materials Science* 8: 327–57. https://doi.org/10.3323/jcorr.60.236.

Oriani, R.A., and P. H. Josephic. 1974. "Equilibrium Aspects of Hydrogen-Induced Cracking of Steels." *Acta Materialia* 22: 1065–74. https://doi.org/10.1016/0001-6160(74)90061-3.

Orr, R. L. 1960. "Heats of Formation of Solid Au Cu Alloys." *Acta Metallurgica* 8: 489–93.

Osono, H., T. Kino, Y. Kurokawa, and Y. Fukai. 1995. "Agglomeration of Hydrogen-Induced Vacancies in Nickel." *Journal of Alloys and Compounds* 231: 41–45. https://doi.org/10.1016/0925-8388(95)01835-2.

Pan, Bing, Kemao Qian, Huimin Xie, and Anand Asundi. 2009. "Two-Dimensional Digital Image Correlation for in-Plane Displacement and Strain Measurement: A Review." *Measurement Science and Technology* 20 (6). https://doi.org/10.1088/0957-0233/20/6/062001.

Parks, B. W., J. D. Fritz, and H. W. Pickering. 1989. "The Difference in the Electrochemical Behavior of the Ordered and Disordered Phases of Cu3Au." *Scripta Metallurgica* 23 (6): 951–56. https://doi.org/10.1016/0036-9748(89)90276-7.

Perng, T. P., and C. J. Altstetter. 1987. "Comparison of Hydrogen Gaas Embrittlement of Austenitic and Ferritic Stainless Steels." *Metallurgical Transactions A* 18A: 123–34.

Petch, N. J., and P. Stables. 1952. "Delayed Fracture of Metals under Static Load." *Nature* 169: 842–43.

Petegem, Steven Van, Stefan Brandstetter, Robert Maass, Andrea M. Hodge, Bassem S. El-Dasher, Jürgen Biener, Bernd Schmitt, Camelia Borca, and Helena Van Swygenhoven. 2009. "On the Microstructure of Nanoporous Gold: An X-Ray Diffraction Study." *Nano Letters* 9 (3): 1158–63. https://doi.org/10.1021/nl803799q.

Pia, Giorgio, Alberto Cincotti, and Francesco Delogu. 2016. "Thermally and Catalytically Induced Coarsening of Nanoporous Au." *Materials Letters* 183: 114–16. https://doi.org/10.1016/j.matlet.2016.07.051.

Pickering, H. W. 1983. "Characteristic Features of Alloy Polarization Curves." *Corrosion Science* 23 (10). https://doi.org/10.1016/0010-938X(83)90092-6.

Pickering, H. W., and C. Wagner. 1967. "Electrolytic Dissolution of Binary Alloys Containing a Noble Metal." *Journal of The Electrochemical Society* 114 (7): 698. https://doi.org/10.1149/1.2426709.

Pugh, E. N. 1985. "Progress toward Understanding the Stress-Corrosion Problem." *Corrosion* 41 (9): 517–26.

Rabinovitch, A., V. Frid, and D. Bahat. 2006. "Wallner Lines Revisited." *Journal of Applied Physics* 99 (7). https://doi.org/10.1063/1.2181692.

Ravi-Chandar, K. 1998. "Dynamic Fracture of Nominally Brittle Materials." *International Journal of Fracture* 90 (1901): 83–102. https://doi.org/10.1023/A:1007432017290.

Rhodin, T.N. 1959. *Physical Metallurgy of Stress Corrosion Fracture*. New York: Interscience Publishers, Inc.

Ricker, R. E., J. L. Fink, J. S. Harris, and A. J. Shapiro. 1992. "Evidence for Film-Induced Cleavage in Rhodium Plated Nickel." *Scripta Metallurgica et Materiala* 26: 1019–23.

Robertson, Ian M., P. Sofronis, A. Nagao, M. L. Martin, S. Wang, D. W. Gross, and K. E. Nygren. 2015. "Hydrogen Embrittlement Understood." *Metallurgical and Materials Transactions A: Physical Metallurgy and Materials Science* 46 (6): 2323–41. https://doi.org/10.1007/s11661-015-2836-1.

Rugolo, J, J Erlebacher, and K Sieradzki. 2006. "Length Scales in Alloy Dissolution and Measurement of Absolute Interfacial Free Energy." *Nature Materials* 5 (12): 946–49. https://doi.org/10.1038/nmat1780.

Saito, M., G. S. Smith, and R. C. Newman. 1993. "Testing the Film-Induced Cleavage Model of Stress-Corrosion Cracking." *Corrosion Science* 35 (1–4): 411–13. https://doi.org/10.1016/0010-938X(93)90174-F.

Scamans, G. M., and P. R. Swann. 1978. "High Voltage Electron Metallography of Stress Corrosion Cracking of Austenitic Stainless Steels." *Corrosion Science* 18 (11): 983–95. https://doi.org/10.1016/0010-938X(78)90033-1.

Scott, T. E., and A. R. Troiano. 1960. "Interstitials and Fracture of Metals." *Nature* 185 (4710): 372–73. https://doi.org/10.1038/185372a0.

Scully, J.C. 1977. "Stress Corrosion Crack Propagation." In *Advances in Research on the Strength and Fracture of Materials*, edited by D. M. R. Taplin, 1:407–28. Pergamon Press Inc. https://doi.org/10.1016/B978-0-08-022136-6.50035-4.

Seebauer, E. G., and C. E. Allen. 1995. "Estimating Surface Diffusion Coefficients." *Progress in Surface Science* 49 (3): 265–330. https://doi.org/10.1016/0079-6816(95)00039-2.

Seker, Erkin, Wei-Chuan Shih, and Keith J. Stine. 2018. "Nanoporous Metals by Alloy Corrosion: Bioanalytical and Biomedical Applications." *MRS Bulletin* 43 (1): 49–56. https://doi.org/10.1557/mrs.2017.298.

Senior, N. A., and R. C. Newman. 2006. "Synthesis of Tough Nanoporous Metals by Controlled Electrolytic Dealloying." *Nanotechnology* 17 (9): 2311–16. https://doi.org/10.1088/0957-4484/17/9/040.

Sharon, Eran, and Jay Fineberg. 1999. "Confirming the Continuum Theory of Dynamic Brittle Fracture for Fast Cracks." *Letters to Nature* 397 (6717): 333–35. https://doi.org/10.1038/16891.

Shishvan, Siamak S, Gábor Csányi, and Vikram S Deshpande. 1952. "Journal of the Mechanics and Physics of Solids." *Nature* 170 (4336): 955. https://doi.org/10.1038/170955a0.

Sieradzki, K., R. R. Corderman, K. Shukla, R. C. Newman, and K. Sieradzki. 1989. "Computer Simulations of Corrosion: Selective Dissolution of Binary Alloys." *Philosophical Magazine A: Physics of Condensed Matter, Structure, Defects and Mechanical Properties* 59 (4): 713–46. https://doi.org/10.1080/01418618908209817.

Sieradzki, K., G. J. Dienes, A. Paskin, and B. Massoumzadeh. 1988. "Atomistics of Crack Propagation." *Acta Metallurgica* 36 (3): 651–63. https://doi.org/10.1016/0001-6160(88)90099-5.

Sieradzki, K., N. Dimitrov, D. Movrin, C. McCall, N. Vasiljevic, and J. Erlebacher. 2002. "The Dealloying Critical Potential." *Journal of The Electrochemical Society* 149 (8): B370. https://doi.org/10.1149/1.1492288.

Sieradzki, K., J. S. Kim, A. T. Cole, and R. C. Newman. 1987. "The Relationship Between Dealloying and Transgranular Stress-Corrosion Cracking of Cu-Zn and Cu-Al Alloys." *Journal of The Electrochemical Society* 134 (7): 1635–39. https://doi.org/10.1149/1.2100726.

Sieradzki, K., and R. C. Newman. 1985. "Brittle Behavior of Ductile Metals during Stress-Corrosion Cracking." *Philosophical Magazine A* 51 (1): 95–132. https://doi.org/10.1080/01418618508245272.

Sieradzki, K., and R.C. Newman. 1986. "A Percolation Model for Passivation in Stainless Steels." *Journal of The Electrochemical Society* 133 (9): 1979–80. https://doi.org/10.1149/1.2109065.

———. 1987. "Stress-Corrosion Cracking." *Journal of Physics and Chemistry of Solids* 48 (11): 1101–13. https://doi.org/10.1016/0022-3697(87)90120-X.

Sieradzki, K. 1990. "Atomistic and Micromechanical Modeling Aspects of Environment-Induced Cracking of Metals." In *Environment-Induced Cracking of Metals*, 125–37. Houston: NACE.

Sieradzki, K, and F J Friedersdorf. 1994. "Notes on the Surface Mobility Mechanism of Stress-Corrosion Cracking." *Corrosion Science* 36 (4): 669–75.

Snyder, J., T. Fujita, M. W. Chen, and J. Erlebacher. 2010. "Oxygen Reduction in Nanoporous Metal-Ionic Liquid Composite Electrocatalysts." *Nature Materials* 9 (11): 904–7. https://doi.org/10.1038/nmat2878.

Song, J., and W. A. Curtin. 2014. "Mechanisms of Hydrogen-Enhanced Localized Plasticity: An Atomistic Study Using α-Fe as a Model System." *Acta Materialia* 68: 61–69. https://doi.org/10.1016/j.actamat.2014.01.008.

Staehle, R. W. 2016. *Historical Views on Stress Corrosion Cracking of Nickel-Based Alloys: The Coriou Effect. Stress Corrosion Cracking of Nickel Based Alloys in*

*Water-Cooled Nuclear Reactors: The Coriou Effect*. European Federation of Corrosion. https://doi.org/10.1016/B978-0-08-100049-6.00001-X.

Stalder, B., P. Beguelin, and H.H. Kausch. 1983. "A Simple Velocity Gauge for Measuring Crack Growth." *International Journal of Fracture* 22: R47–54.

Stillwell, Charles W., and Edward S. Turnipseed. 1934. "Mechanism of Dezincification: Corrosion of ∈-Brass." *Industrial and Engineering Chemistry* 26 (7): 740–43. https://doi.org/10.1021/ie50295a011.

Stuckner, Joshua, Katherine Frei, Ian McCue, Michael J. Demkowicz, and Mitsuhiro Murayama. 2017. "AQUAMI: An Open Source Python Package and GUI for the Automatic Quantitative Analysis of Morphologically Complex Multiphase Materials." *Computational Materials Science* 139: 320–29. https://doi.org/10.1016/j.commatsci.2017.08.012.

Sun, Shaofeng, Xiying Chen, Nilesh Badwe, and Karl Sieradzki. 2015. "Potential-Dependent Dynamic Fracture of Nanoporous Gold." *Nature Materials* 14 (9): 894–98. https://doi.org/10.1038/nmat4335.

Sun, Ye, Sofie A. Burger, and T. John Balk. 2014. "Controlled Ligament Coarsening in Nanoporous Gold by Annealing in Vacuum versus Nitrogen." *Philosophical Magazine* 94 (10): 1001–11. https://doi.org/10.1080/14786435.2013.876113.

Sun, Ye, Kalan P. Kucera, Sofie A. Burger, and T. John Balk. 2008. "Microstructure, Stability and Thermomechanical Behavior of Crack-Free Thin Films of Nanoporous Gold." *Scripta Materialia* 58 (11): 1018–21. https://doi.org/10.1016/j.scriptamat.2008.01.036.

Tse, Ariana Y., Erin K. Karasz, and Karl Sieradzki. 2020. "Dealloying and Morphology Evolution of Ordered and Disordered Cu3Au." *Scripta Materialia* 176: 112–16. https://doi.org/10.1016/j.scriptamat.2019.09.008.

Turnbull, A. 1993. "Modelling of Environment Assisted Cracking." *Corrosion Science* 34 (6): 921–60. https://doi.org/10.1016/0010-938X(93)90072-O.

Vartabedian, Ralph. 2020. "'Horrible Sequence of Mistakes': How Bullet Train Contractors Botched a Bridge Project." *Los Angeles Times*, August 25, 2020.

Vermilyea, David A. 1972. "A Theory for the Propagation of Stress Corrosion Cracks in Metals." *Journal of The Electrochemical Society* 119 (4): 405–7. https://doi.org/10.1149/1.2404217.

———. 1977a. "A Film Rupture Model for Stress Corrosion Cracking." In *Stress Corrosion Cracking and Hydrogen Embrittlement of Iron Base Alloys*, 217.

———. 1977b. "A Film Rupture Model for Stress Corrosion Cracking." In *Stress*

*Corrosion Cracking and Hydrogen Embrittlement of Iron Base Alloys*, edited by R. W. Staehle, J. Hochmann, R. D. McCright, and J. E. Slater, 208–17. Houston: NACE.

Volkert, C. A., and E. T. Lilleodden. 2006. "Size Effects in the Deformation of Sub-Micron Au Columns." *Philosophical Magazine* 86 (33-35 SPEC. ISSUE): 5567–79. https://doi.org/10.1080/14786430600567739.

Volkert, C. A., E. T. Lilleodden, D. Kramer, and J. Weissmüller. 2006. "Approaching the Theoretical Strength in Nanoporous Au." *Applied Physics Letters* 89 (6): 3–5. https://doi.org/10.1063/1.2240109.

Vook, Richard W., and Baybars Oral. 1987. "The Epitaxy of Gold." *Gold Bulletin* 20 (1–2): 13–20. https://doi.org/10.1007/BF03214654.

Wang, Ke, and Jörg Weissmüller. 2013. "Composites of Nanoporous Gold and Polymer." *Advanced Materials* 25 (9): 1280–84. https://doi.org/10.1002/adma.201203740.

Weissmüller, J., R. N. Viswanath, D. Kramer, P. Zimmer, R. Würschum, and H. Gleiter. 2003. "Charge-Induced Reversible Strain in a Metal." *Science* 300 (5617): 312–15. https://doi.org/10.1126/science.1081024.

Weissmüller, Jörg, Roger C. Newman, Hai Jun Jin, Andrea M. Hodge, and Jeffrey W. Kysar. 2009. "Nanoporous Metals by Alloy Corrosion: Formation and Mechanical Properties." *MRS Bulletin* 34 (8): 577–86. https://doi.org/10.1557/mrs2009.157.

Wells, D B, J Stewart, R Davidson, P M Scott, and E H Williams. 1992. "The Mechanism of Intergranular Stress Corrosion Cracking of Sensitised Austenitic Stainless Steel in Dilute Thiosulphate Solution." *Corrosion Science* 33 (1): 39–71.

Wittstock, A., V. Zielasek, J. Biener, C.M. Friend, and M. Baumer. 2010. "Nanoporous Gold Catalysts for Selective Gas-Phase Oxidative Coupling of Methanol at Low Temperature." *Science* 327 (January): 319–22. https://doi.org/10.1126/science.1183591.

Wittstock, Arne, Jürgen Biener, and Marcus Bäumer. 2010. "Nanoporous Gold: A New Material for Catalytic and Sensor Applications." *Physical Chemistry Chemical Physics* 12 (40): 12919–30. https://doi.org/10.1039/c0cp00757a.

Wittstock, Arne, Jürgen Biener, Jonah Erlebacher, and Marcus Baumer, eds. 2012. *Nanoporous Gold: From an Ancient Technology to a High-Tech Material*. Royal Society of Chemistry.

Wolverton, C, Alex Zunger, and V Ozolin. 1998. "<1998-Alex Zunger-First-Principles Study of Temperature-Composition Phase Diagrams and Structures.Pdf>" 57 (11): 6427–43.

Xiao, Xinxin, Meng'En Wang, Hui Li, Yichuan Pan, and Pengchao Si. 2014. "Non-Enzymatic Glucose Sensors Based on Controllable Nanoporous Gold/Copper Oxide Nanohybrids." *Talanta* 125: 366–71. https://doi.org/10.1016/j.talanta.2014.03.030.

Yin, Guang, Ling Xing, Xiu Ju Ma, and Jun Wan. 2014. "Non-Enzymatic Hydrogen Peroxide Sensor Based on a Nanoporous Gold Electrode Modified with Platinum Nanoparticles." *Chemical Papers* 68 (4): 435–41. https://doi.org/10.2478/s11696-013-0473-y.

Zeis, Roswitha, Tang Lei, Karl Sieradzki, Joshua Snyder, and Jonah Erlebacher. 2008. "Catalytic Reduction of Oxygen and Hydrogen Peroxide by Nanoporous Gold." *Journal of Catalysis* 253 (1): 132–38. https://doi.org/10.1016/j.jcat.2007.10.017.

Zhang, Yongsheng, Georg Kresse, and C. Wolverton. 2014. "Nonlocal First-Principles Calculations in Cu-Au and Other Intermetallic Alloys." *Physical Review Letters* 112 (7): 1–5. https://doi.org/10.1103/PhysRevLett.112.075502.

Zheng, Yanjie, Yichun Xu, Lingling Lin, You Li, Wei Chen, Jinyuan Chen, Yun Lei, et al. 2019. "Nanoporous Gold Electrode Prepared from Two-Step Square Wave Voltammetry (SWV) and Its Application for Electrochemical DNA Biosensing of Lung Resistance Related Protein (LRP) Gene." *Journal of Electroanalytical Chemistry* 840 (February): 165–73. https://doi.org/10.1016/j.jelechem.2019.03.035.